EVIDENCE OF THREE-DIMENSIONAL CLOUD EFFECTS IN SATELLITE MEASUREMENTS OF REFLECTED SOLAR RADIATION

BY

NORMAN GARY LOEB

A thesis submitted to the Faculty of Graduate Studies and Research
in partial fulfillment of the requirements for the degree of

DOCTOR OF PHILOSOPHY

January, 1996

Department of Atmospheric and Oceanic Sciences
McGill University, Montréal, Québec, Canada

ISBN 0-612-12420-7

Abstract

The purpose of this study is to assess the performance of the plane parallel model in analyzing satellite measurements of clouds, and to examine what role 3D cloud effects may play in explaining any discrepancies. Direct comparisons between one year of Earth Radiation Budget Satellite (ERBS) scanner radiances and plane parallel model calculations are carried out under different Sun-Earth-satellite viewing configurations over ocean between 30°N and 30°S. When the plane parallel model calculations are matched to observations at nadir on a pixel-by-pixel basis by adjusting cloud fraction and cloud optical depth, the resulting frequency distributions of cloud optical depth show a systematic shift towards larger values with increasing solar zenith angle, regardless of what assumptions are made in the calculations. On average, this increase in cloud optical depth is extremely large for solar zenith angles ≥ 63°. For the thinnest 50% of the clouds, the increase only occurs at very oblique sun angles, whereas it is observed at all solar zenith angles for the thickest 10% of clouds. The cause is traced to a fundamental flaw in plane parallel theory when applied to real clouds: at nadir the solar zenith angle dependence of model reflectance is opposite to that of the observations.

On average, differences between observed and plane parallel model reflectances are found to be less sensitive to view and relative azimuth angle than to solar zenith angle. For solar zenith angles less than ≈63°, plane parallel model reflectances are within ≈10% of the observations. As solar zenith angle increases, differences between the observations and calculations increase at all view angles. At lower sun elevations, observed reflectances exceed plane parallel values by a constant amount at all view angles in the backscattering direction, while plane parallel model reflectances show a different view angle dependence from that observed in the forward direction. When comparisons are performed as a function of relative azimuth angle, no appreciable dependence in the reflectance difference

is observed. Violation of the principle of reciprocity applied to real observations is shown to be mainly caused by the systematic difference in the solar zenith angle dependence between observations and plane parallel calculations.

Monte Carlo simulations involving stochastic, isotropic, scale-invariant broken cloud fields are carried out in order to show that, qualitatively, differences between observed and plane parallel reflectances are generally consistent with 3D theory. While much of the discrepancy between 3D and 1D reflectances can be attributed to the presence of cloud sides, affecting the illuminated cloud area, it is shown that the slope of the illuminated cloud top surfaces may also play an important role.

Résumé

L'objectif de cette recherche est d'évaluer la performance des modèles plan-parallèle comme outil d'analyse des observations satellitaires des nuages, ainsi que d'étudier si des effets tri-dimensionels peuvent expliquer certaines lacunes de ces modèles. De plus, nous avons comparé une année d'observations de la radiance telles qu'obtenues par le "Earth Radiation Budget Satellite (ERBS)" à des résultats calculés à l'aide d'un modèle plan-parallèle. Nous avons éffectué cette comparaison pour différentes configurations du système soleil-terre-satellite pour des régions au-dessus de l'océan entre les latitudes 30°N et 30°S. Dans le cas d'observations prises au nadir, la comparaison pixel par pixel, faite en ajustant les coefficients de fraction nuageuse et d'épaisseur nuageuse donne un spectre d'épaisseur nuageuse qui glisse vers de plus grandes valeurs pour un angle solaire croissant. Nous obtenons ce résultat quelles que soient les hypothèses que nous faisons dans les calculs. En moyenne, cet accroissement est très important lorsque l'angle solaire dépasse 63°. D'autre part, pour la moitié de nuages la plus mince, cet accroissement ne se produit que pour des angles solaires très obliques, tandis que pour les 10% des nuages les plus épais il se produit pour tous les angles solaires. Nous identifions la cause de ce comportement comme étant une lacune fondamentale des modèles plan-parallèle lorsqu'ils sont appliqués à de vrais nuages. Au nadir, la dépendance de la réflectivité sur l'angle solaire, telle que calculée par le modèle, est contraire à celle révélée par les observations.

Nous constatons que les différences entre les réflectivités observées et calculées sont plus sensibles à l'angle solaire qu'à l'angle de mesure ou à l'angle azimutal relatif. Pour les angles solaires de moins de 63°, l'écart est de moins de 10%. Pour tous les angles de mesures, cet écart augmente en fonction de l'angle solaire croissant. Dans la direction de la dispersion vers l'arrière, les réflectivités observées sont systématiquement supérieures à celles calculées. Dans la direction de la dispersion vers l'avant, la dépendance sur l'angle de mesure des valeurs de réflectivités calculée est différente. Nous n'avons trouvé aucune

variation systématique de la différence entre les réflectivités calculées et observées en fonction de l'angle azimutal relatif. Nous montrons que la violation du principe de réciprocité appliqué aux observations est due aux différences systématiques de la dépendance sur l'angle solaire des différences entre les observations et les calculs.

Utilisant des champs de nuages stochastiques, isotropes et avec invariance d'échelle nous avons éffectué des simulations de Monte Carlo pour démontrer que, qualitativement, les différences entre les réflectivités observées et celles calculées avec un modèle plan-parallèle sont généralement en accord avec ce qui est prédit par la théorie 3D. Nous montrons que même si ces différences sont surtout dues à la présence des côtés de nuages, la pente de la surface illuminée du sommet des nuages a possiblement aussi un rôle important.

Statement of Originality

The original results presented in this thesis are as follows:

(1) When the plane parallel model approach is used to infer cloud optical depth directly from observations at nadir, the resulting frequency distributions of cloud optical depth show a systematic shift towards larger values with increasing solar zenith angle.

(2) When observations and plane parallel calculations are compared as a function of view angle, differences tend to be small for solar zenith angles $\lesssim 63^\circ$, but increase at all view angles at lower sun elevations. While the differences do not show much of a dependence on view angle in the backscattering direction, there are marked differences in the view angle dependence between the observations and calculations in the forward direction. Overall, no significant dependence on relative azimuth angle in the differences is observed.

(3) The breakdown in the principle of reciprocity applied to real observations is found to be mainly caused by the systematic difference in the solar zenith angle dependence between observations and plane parallel calculations.

(4) The effect of cloud top structure, such as the slope of illuminated cloud top surfaces, is found have an important effect on the radiation field based on Monte Carlo simulations of 3D clouds.

While Professor Roger Davies is responsible for suggesting this research project, and has monitored its progress closely, the data analysis, writing and editing of the thesis was carried out exclusively by the author. The results presented in (1) (Chapter 2 of the thesis) are closely related to a paper, co-authored by myself (first author) and Professor Davies, which has been accepted for publication in a refereed scientific journal (*Journal of Geophysical Research (Atmospheres)*). Professor Davies participated in the writing and editing of that paper. Plans are also under way to submit papers based on items (2) through (4) (Chapters 3 and 4 of the thesis) for publication in the near future.

Acknowledgments

I wish to express my sincere gratitude to Professor Roger Davies for his excellent supervision and encouragement during the course of this study. I have benefited immensely from his keen scientific insight and vast knowledge on cloud radiative processes and global climate.

I would also like to thank Tamás Várnai for allowing me to use his Monte Carlo model and for his helpful advice and comments. Thanks goes to my other fellow students, Lazaros Oreopoulos and Larry Di Girolamo, for the many interesting scientific discussions we've had over the past three years, and to Paul Vaillancourt for helping me with the French translation of the abstract.

I would like to acknowledge the following agencies for the financial support of this research: Fonds pour la Formation de Chercheurs et l'Aide à la Recherche (FCAR), the Natural Sciences and Engineering Research Council (NSERC), the Atmospheric Environment Service (AES), and the Jet Propulsion Laboratory (JPL).

Finally, I would like to dedicate this thesis to my parents, Max and Martha Loeb, for their love and support. Throughout the years they have always been there for me, and I am deeply grateful for it.

Table of Contents

Figure	List of Figures	Page

Figure	List of Figures	Page

Figure	List of Figures	Page

Figure	List of Figures	Page

Figure	List of Figures	Page

List of Tables

Chapter 1

Introduction

1.1 Background

Clouds are involved in the two key energy exchange processes that determine the Earth's climate, namely, radiative exchanges and water exchanges. They reflect approximately 20% of the incoming solar radiation globally, and modulate longwave radiation emitted to space. Understanding their effect on the Earth's radiation budget is complicated by the fact that clouds occur over a wide range of spatial and temporal scales, and because their radiative properties can vary depending on such characteristics as their thickness, amount, shape, microphysics, temperature, water phase, etc. One of the main uncertainties in understanding climate's sensitivity to perturbations is the nature of cloud-radiation feedbacks. In fact, in an intercomparison of nineteen state-of-the-art General Circulation Models (GCM's), Cess et al. (1990) found a threefold variation in climate sensitivity attributable primarily to the different treatment of clouds by the different models. For these reasons, the study of cloud properties and their effect on radiation has become one of the most important areas in climate research according to the World Climate Research Program (WCRP, 1990).

Since the first satellite images were returned in the early 1960's, it was immediately recognized that satellites can provide valuable information on cloud properties (Arking, 1964; Young, 1967). Only with satellite measurements can a comprehensive overview of cloud systems over large portions of the globe be obtained on a frequent basis. While the early work tended to be mainly qualitative in nature, much of the research during the past fifteen years has been devoted towards attaining a more quantitative measure of clouds and their radiative effects. These include studies which have addressed the effects of clouds on the radiative energy exchange at the top of the atmosphere (Hartmann et al., 1986; Ramanathan, 1987), and those which have provided global climatologies of the physical properties of clouds (Schiffer and Rossow, 1983; Stowe, et al., 1989). Future missions such as the Earth Observing System (EOS) (to be launched in 1998) will continue to provide vital information on cloud and other variables necessary to improve our understanding of climate processes (Dozier, 1994).

To obtain quantitative information on the physical properties of clouds from satellite measurements, models/algorithms are needed which can interpret radiance measurements and relate these to the clouds in the satellite's field-of-view. The conventional approach in cloud remote sensing applications adopts the plane parallel assumption which considers clouds to be (locally) one-dimensional and therefore horizontally invariant (e.g. Rossow, 1989). We know from practical experience, however, that real clouds occur in a wide variety of shapes and sizes that have obvious three-dimensional characteristics, and one might reasonably expect there to be many discrepancies between one- and three-dimensional approaches. While ample theoretical evidence exists to support this (e.g. Busygin, 1973; McKee and Cox 1974; Aida, 1977; Davies, 1978; Davies, 1984; Bréon, 1992; Kobayashi, 1993), by comparison, relatively few observational studies have addressed this issue. Those that have were limited either to small sample sizes (e.g. Coakley and Davies, 1986; Rossow, 1989; Coakley, 1991), or involved the use of empirical bidirectional cloud reflectance models (normalized by upwelling irradiance) rather than the actual satellite radiance measurements themselves (Stuhlmann et al., 1985). Nevertheless, these and other studies (e.g. Minnis, 1989; Davies, 1994) suggest that the simple 1D approach is inadequate for certain types of clouds, and may lead to substantial biases when used to infer cloud properties from satellite measurements. Additional observational studies are now needed to quantify this bias for mixtures of cloud types that are representative of general conditions.

1.2 3D Cloud Effects

In general, 3D cloud effects may be attributed to various combinations of (a) non-linear averaging of sub-pixel inhomogeneity, (b) cloud sides, affecting illuminated and viewed cloud cross-sections as well as allowing loss of radiation, (c) cloud top structure, and (d) internal cloud inhomogeneity. Because radiance is a convex function of cloud optical depth, the assumption that the sensor field-of-view is covered by a single uniform cloud layer when in fact there may be a variety of cloud thicknesses will tend to cause optical depth retrievals to be underestimated due to (a) (Stephens, 1986). This will depend on how the cloud mass is distributed within the field-of-view and will tend to be more pronounced at small solar zenith angles when (b) is factored in due to the loss of radiation through the cloud sides (i.e. diffusive leakage). The presence of cloud sides also enhances the illuminated area of the scene, which can affect the angular distribution of reflected radiation (Davies, 1984). Internal inhomogeneities due to small-scale liquid water content variations within clouds can also cause a "channeling" effect (Cannon, 1970; Cahalan, 1989; Davis et al., 1990), whereby radiation from denser portions of the cloud may get preferentially "channeled" into less dense regions, thus reducing cloud albedo relative to internally homogeneous clouds. However, since the path length of photons at visible wavelengths is generally greater than the size of smaller scale cloud structures, multiple scattering will tend to filter out their effects, leaving the radiance largely dependent only on the grossest scales (Stephens, 1988; Rossow, 1989).

Because of the large number of degrees of freedom characterizing cloud inhomogeneities, direct observation of these effects from satellite measurements is rather difficult. In order to isolate the cloud contribution and identify the specific cloud properties, it is necessary to remove atmospheric effects (e.g. molecular and aerosol scattering and attenuation) as well as surface effects (particularly over land in broken cloud scenes). Since cloud inhomogeneities can occur over a wide range of spatial scales, the sensor resolution may also influence the results. If the sensor resolution corresponds to the scale over which the radiation interacts most strongly with the optical property variations, then 3D effects would likely be more pronounced in this case than at other resolutions. Another consideration is the sampling of the measurements—for example, certain inhomogeneities may be more pronounced in specific Sun-Earth-satellite configurations. Spectral considerations may also be important. The fact that radiation is dominated by scattering at one wavelength and absorption at another may also influence the interaction between cloud inhomogeneities and the radiation field (Stephens and Tsay, 1990). Because of these complications, few observational studies of 3D cloud effects have been undertaken.

1.3 This Study

Rather than attempt to identify 3D cloud effects directly from observations, the present study first focuses on determining whether conventional use of the plane parallel model approach is sufficient, on average, to represent the radiative properties in general cloud conditions when analyzing satellite data. The approach is to compare one year of satellite observations directly with plane parallel calculations stratified by Sun-Earth-satellite viewing geometry. Then, 3D cloud simulations are carried out in order to examine what role 3D cloud effects may play in accounting for any discrepancies between the observations and plane parallel results.

The data set is restricted to oceanic scenes equatorward of 30°. These restrictions avoid complications due to changes in underlying surface albedo and strong diurnal effects. The analyzed data are sufficiently non-restrictive, however, that they encompass a wide range of general cloud types. Cumuliform clouds, for which three-dimensional effects are likely to be strong, are well represented in this latitude range. A range of stratiform clouds are also represented, but not as frequently as at higher latitudes (Warren et al., 1988). Cloud types unique to continental and high latitude conditions are missing from this study.

Chapter 2 describes the observations and the development of a reasonably sophisticated one-dimensional analysis procedure. Then, considering only observations with view angle cosines between 0.9-1.0, the validity of the plane parallel approach in estimating cloud optical depth from observations at different solar zenith angles is assessed. In Chapter 3, comparisons between the observed and plane parallel representations of the view and relative azimuth angle dependence of the reflectance field are performed, and the applicability of the principle of reciprocity to satellite observations is discussed. In Chapter 4, Monte Carlo simulations involving 3D cloud fields are carried out in order to examine whether the results in Chapters 2 and 3 can be qualitatively explained by 3D theory.

Chapter 2

Plane Parallel Model Cloud Optical Depth Bias

2.1 Introduction

The remote sensing of cloud properties from satellite-measured radiances, in addition to many other applications, conventionally adopts the plane parallel assumption. In this chapter, the validity of this approach as a means of inferring cloud optical depth from observations at different solar elevations is examined. The analysis relies on the statistical information content of a very large number of observations, stratified by solar zenith angle. For this comparison, the data is restricted to viewing angle cosines between 0.9 and 1.0. This restriction avoids complications due to expansion effects of the viewed area at larger off-nadir angles.

In the following, the development of a reasonably sophisticated one dimensional analysis procedure is described. The absence of measured data to constrain the input variables to the analysis, especially the lack of information on the sub-pixel cloud fraction which completely handicaps the analysis of a single scene, is shown to be much less of a problem when the data are analyzed statistically. Consistent results are in fact obtainable for a wide a range of input assumptions.

2.2 Observations

Observed reflectances are determined from ERBS scanner shortwave radiance measurements as follows:

$$R(\mu,\mu_o,\phi) = \frac{\pi I(\mu,\mu_o,\phi)}{\mu_o F} \mathrm{x}100\% \tag{2.1}$$

where,

I is the shortwave pixel radiance,

F is the solar constant (=1365 W m^{-2}) corrected for the Earth-Sun distance,

μ is the cosine of the observer zenith angle,

μ_o is the cosine of the solar zenith angle,

ϕ is the azimuth angle relative to the solar plane (ϕ=0 corresponds to forward scattering),

The scanner instrument aboard the ERBS satellite measures radiance in three broadband intervals: shortwave (0.2 to 5 μm), longwave (5 to 50 μm) and total (0.2 to 50 μm) (Kopia, 1986; Barkstrom et al., 1989). The scan is perpendicular to the orbital track with a field-of-view (FOV) of about 31x47 km^2 at nadir, increasing to about 550x150 km^2 at the limb. The ERBS orbit is in a 57° inclination which precesses 4.95° west per day, allowing measurements from many different Sun-Earth-satellite viewing configurations to be sampled during the course of one month.

One year (from November, 1984, to October, 1985) of pixel-level (S-8) measurements are considered here. Only scenes over ocean between 30°S and 30°N are included in order to avoid complications arising from strong diurnal effects and surface inhomogeneities, and because albedos over ocean are generally quite small compared to those from clouds (outside of the sunglint region). Tropical latitudes were selected because there tends to be a higher frequency of occurrence of cumuliform clouds than at higher latitudes (Warren et al., 1988). As a result, the tropics provide a good testbed for examining how the plane parallel model compares with observations.

Fig. 2.1 illustrates the coordinate system used in this study. The data is stratified into ten bins of the cosine of the solar zenith angle (μ_o) between 0 and 1, seven bins of the cosine of the view angle (μ) between 0.3 and 1, and six relative azimuth (ϕ) bins of width 30° between 0° and 180°. Note that the comparisons are restricted to μ>0.3 since beyond this point, the Earth does not entirely fill the ERBS scanner field-of-view.

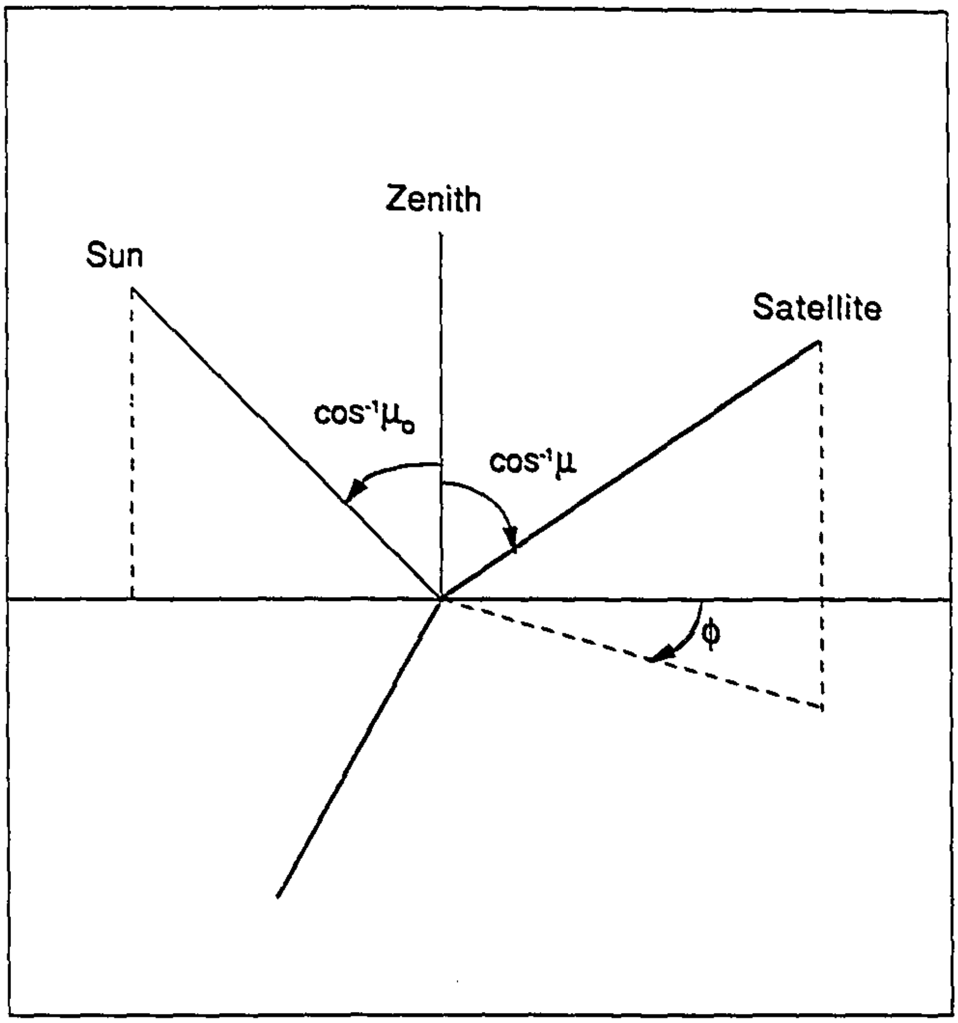

Figure 2.1 Schematic illustrating the coordinate system used in this study.

While other instruments capable of providing measurements at a higher resolution than ERBS are available (e.g. AVHRR, Landsat), they were not selected for the purposes of this study since they are generally in sun-synchronous orbits. Measurements from sun-synchronous orbits cannot be easily applied to examine the μ_o dependence of cloud properties since a given region will only be sampled over a finite range of solar zenith angles. In contrast, instruments which are in a precessing orbit can sample the same region over the full range of solar zenith angles. In the case of ERBS, nearly complete solar zenith angle sampling is achieved every thirty-six days (Baldwin and Coakley, 1991).

2.3 Plane Parallel Calculations

Since the ERBS scanner footprint can exceed the size of individual cloud elements, many of the measurements from ERBS are taken from mixed scenes—that is, scenes composed of both clear and sub-pixel cloud regions. The sensitivity to such inhomogeneities in the plane parallel calculations can be evaluated by neglecting 3D effects and assuming the radiance is a linear function of cloud fraction (f). Thus, reflectances from pixels which are partly filled by a single layer cloud can be approximated as:

$$R = (1-f)R^{CLR} + fR^{CLD} \qquad (2.2)$$

where

R^{CLD} is the shortwave reflectance contribution from the cloudy portion of the pixel (depends on cloud optical depth τ_p) and

R^{CLR} is the shortwave reflectance contribution from the clear-sky portion of the pixel.

Alternately, another commonly used approach in satellite remote sensing is to assume the pixels to be homogeneous—either overcast or clear. This removes one degree of freedom in the calculations since cloud fraction is always unity for cloudy pixels. This approach has merit provided the spatial resolution of the measurements is sufficiently high. While this is not the case in this study (due to the low resolution of ERBS measurements), this approach is nonetheless considered here along with the inhomogeneous approximation for comparison purposes. The following sections describe how the R^{CLD} and R^{CLR} values are obtained.

2.3.1 Cloud Reflectances (R^{CLD})

Modeling the transfer of radiation from cloudy atmospheres across broad spectral intervals requires that the spectral variation of both cloud and clear sky scattering and transmission be taken into account. Here, look-up tables of R^{CLD} were generated using the DISORT program of Stamnes et al. (1988) which is based on the Discrete Ordinates Method. The look-up tables consist of R^{CLD} determined at 31 cloud optical depths between 0.5 and 200 (defined at 0.55 μm), 19 view and solar zenith angles between 0° and 89°, and 19 azimuth angles between 0° and 180°. Reflectances at arbitrary angles and cloud optical depths are obtained by interpolation of the look-up table reflectances. Forty-eight streams were used in all DISORT calculations and Earth curvature effects were also accounted for. The atmosphere was divided into four homogeneous vertical layers corresponding to a lower boundary layer, a cloud layer, a tropospheric layer and a stratospheric layer. Reflection from the ocean surface below the cloud layer was obtained using the Lambertian model with an albedo of 7%. Unfortunately, since cloud-top heights were not available on a scene-by-scene basis, a fixed cloud-top height had to be assumed. Based on International Satellite Cloud Climatology Project (ISCCP) results of one-year of cloud-top height retrievals over ocean (Rossow and Schiffer, 1991), a cloud-top height of 3 km was used. For comparison purposes, look-up tables were also derived for a cloud-top height of 6 km, and for the case where no atmosphere is present above or below the cloud.

When included, scattering in the layers above and below the cloud layer consists of both molecular and aerosol scattering. All clear sky optical depths, aerosol phase functions and single scattering albedos for the boundary layer, troposphere and stratosphere were obtained directly from the LOWTRAN-7 model (Kneizys et al., 1988). Fig. 2.2 shows the

0.5 µm clear sky optical depth profiles of ozone absorption, aerosol scattering, molecular scattering, and the total, used in the calculations. Since aerosol concentrations can show rather large temporal and spatial variations over ocean (Prospero et al., 1983; Hoppel et al., 1990), the largest uncertainty in these profiles is associated with the aerosol component. In this study, an aerosol optical depth of 0.1 at the surface is assumed based on the studies of Toon and Pollack (1976) and Durkee et al. (1991) who found aerosol optical depths to typically range between 0.05 and 0.2 over ocean.

Within the cloud layer, drop-size distributions are represented using Deirmendjian's C.1 cloud model (Deirmendjian, 1969). Single scattering properties were calculated using the Mie scattering code of Bohren and Huffman (1983) with refractive indices from Hale and Querry (1973). Only one cloud microphysical model is considered because broadband shortwave reflectances for a given optical depth tend to be quite insensitive to the cloud microphysics. As an example, when reflectances generated using the C.1 model (effective radius 6 µm) for a cloud optical depth of 10 were compared with those generated using a modified gamma size distribution having an effective droplet radius of 10 µm, relative reflectance differences tended to be quite small (< 5%), and no systematic dependence on μ_0 was observed in the differences. This arises because, spectrally, the most significant contribution to the broadband reflectance emanates from visible wavelengths, where sensitivity to cloud microphysics is small (Arking and Childs, 1985; Coakley and Davies, 1986; Loeb, 1992). At longer wavelengths (>0.9 µm) the sensitivity to cloud microphysics is more pronounced, but these wavelengths contribute much less energy to the overall broadband reflectance compared to visible wavelengths. Finally, no account of absorption by water vapor within the cloud was included since absorption is largely dominated by water droplets when water vapor absorption above the cloud is taken into account (Davies et al., 1984).

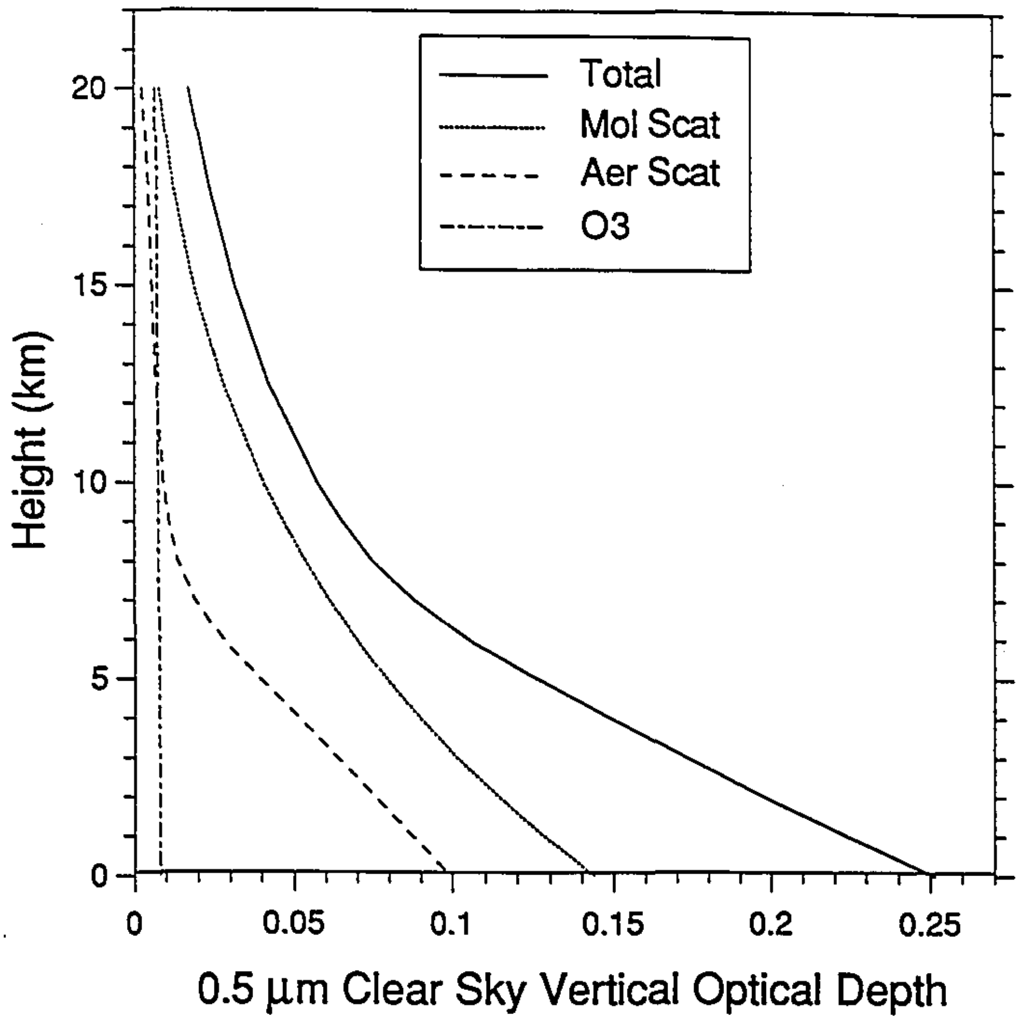

Figure 2.2 0.5 µm clear sky vertical optical depth profiles of ozone, aerosol scattering, molecular scattering and the total.

In order to avoid excessive computational times in generating the look-up tables, the spectral resolution was set no higher than necessary. Based on comparisons of shortwave radiance for different spectral intervals and resolutions from LOWTRAN-7 simulations, a resolution of Δv=1000 cm^{-1} over the 4000 cm^{-1} to 34000 cm^{-1} range was found to yield sufficient accuracy. The simulations consisted of radiance calculations involving the cumulus cloud model in LOWTRAN-7. When radiances obtained using a resolution of Δv=50 cm^{-1} over the complete ERBS shortwave interval of 2000 cm^{-1} to 50000 cm^{-1} were compared to those obtained using Δv=1000 cm^{-1} for wavenumbers between 4000 cm^{-1} and 34000 cm^{-1}, relative differences were generally less than three percent.

2.3.2 Clear Sky Reflectances (R^{CLR})

Rather than rely on model calculations of clear sky reflectance, the approach used here was to generate look-up tables of clear sky reflectances directly from one year of observations. The first step was to define an initial nadir clear sky longwave threshold in order to identify pixels having the greatest probability of actually being cloud-free. This threshold was inferred from the peak in the longwave radiance frequency distribution of pixels identified as clear by the ERBE Maximum Likelihood Estimation (MLE) technique (Wielicki and Green, 1989). Next, by analyzing shortwave reflectance frequency distributions of only those pixels warmer than this clear-sky longwave cut-off, clear-sky reflectances in each μ_0 bin were derived in a similar manner. As an example, Fig. 2.3 shows one such shortwave reflectance frequency distribution (labeled "Clear") for μ_0 = 0.5–0.6. Also shown for comparison are frequency distributions of all pixels in this μ_0 range ("All Data"), and of pixels having a longwave radiance lower than the longwave cut-off ("Cloud Contam"). From the "Clear" frequency distribution, a clear sky reflectance was defined for each μ_0 bin by the reflectance corresponding to the peak of the distribution (for μ_0 = 0.5–0.6, this corresponds to a shortwave reflectance of 6.5%).

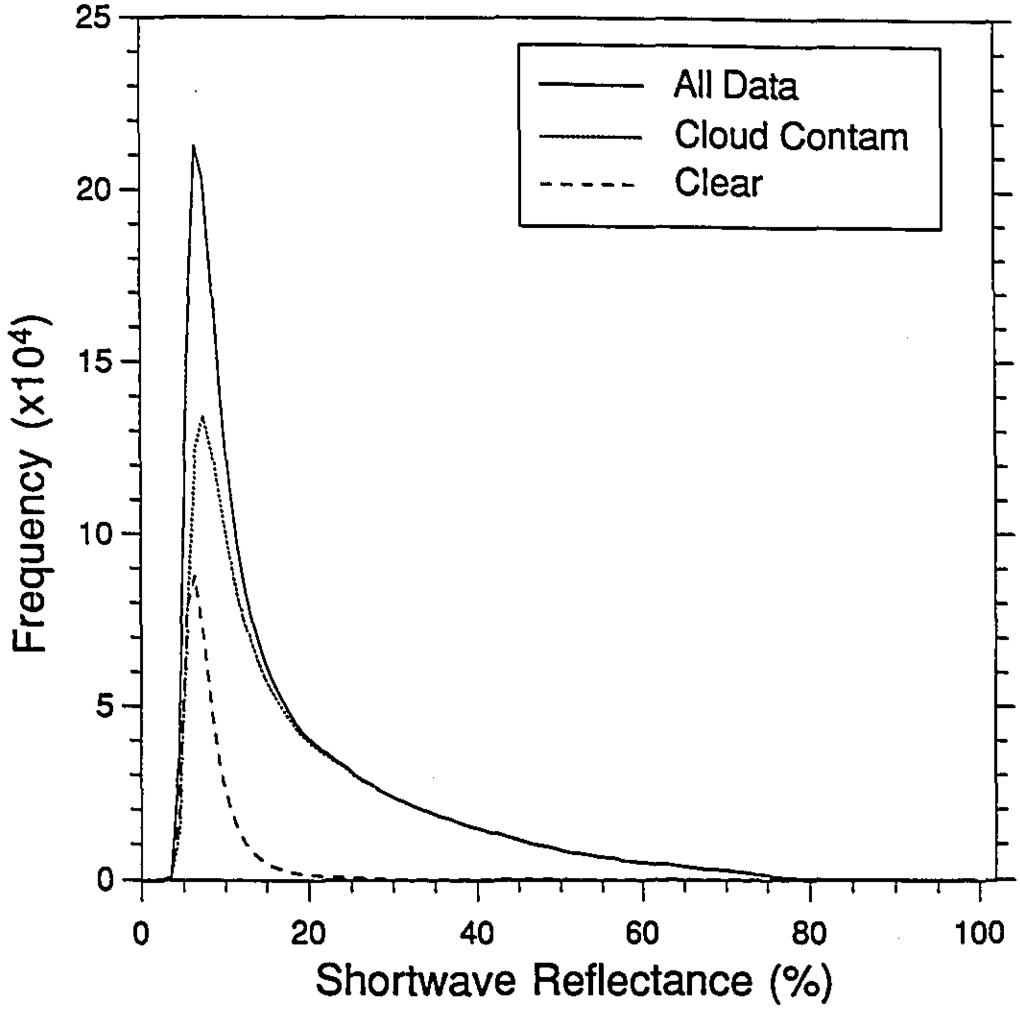

Figure 2.3 Observed shortwave reflectance frequency distribution for μ=0.9-1.0 and μ_o=0.5-0.6 for all data ("All Data"), only data remaining after the longwave cut-off is applied ("Cloud Contam."), and for pixels identified as clear ("Clear").

2.4 Analysis Approach

2.4.1 Sampling Considerations

To avoid introducing uncertainties due to factors not accounted for in the plane parallel calculations, clear scenes and scenes consisting of thick overcast ice clouds are excluded from the analysis. The latter scene types were not included since no provision for scattering by ice crystals was made in this study. To exclude clear scenes, the ERBE clear scene identifier was used. This is likely to be a conservative choice since the ERBE "clear" category may contain ≈5% cloud cover. Scenes consisting of thick overcast ice clouds were more difficult to identify, however. Based on LOWTRAN-7 model calculations (Kneizys et al., 1988) and results from previously published observational studies, longwave thresholds were defined for this purpose. LOWTRAN-7 calculations involving thick cirrus clouds under tropical atmospheric conditions were performed for cloud top heights ranging from 8 km to 11 km. Table 2.1 shows the broadband and 11 μm brightness temperatures obtained for these cases. Broadband brightness temperatures ranged from 230 K (for cloud tops at 11 km) to 245 K (for tops at 8 km), while the corresponding 11 μm brightness temperatures ranged from 233 K to 256 K. Machado et al. (1992) explored a range of 11 μm brightness temperatures based on Meteosat satellite measurements and found 11 μm brightness temperatures to range from 207 K to 253 K (for cloud top heights between 14.5 km and 8 km). Based on these results, a conservative broadband longwave threshold of 245 K (corresponding to an 11 μm brightness temperature of 256 K) was selected to exclude thick ice clouds from the analysis. Since the objective here is to consider water clouds only, this choice of threshold appears to be reasonable. Based on an analysis of ERBS nadir observations, this threshold was observed to remove the coldest 10% of all pixels and to cause average shortwave reflectances to decrease by approximately 3% (absolute change). It should be noted that while this technique will filter out very cold, thick, overcast ice clouds, it will not necessarily exclude all thin or sub-pixel ice clouds since longwave radiances in such cases can be quite similar to those from scenes containing only water clouds. The effect of inadvertently retaining some thin or partly cloudy ice cloud scenes in the analysis is expected to have a minor effect on the average shortwave reflectance dependence on μ_0 since, as will be shown in Section 2.5, the same dependence on μ_0 is observed even when thick ice clouds are included.

Cirrus Cloud Top Height (km)	Broadband Brightness Temperature (K)	11 µm brightness Temperature (K)
8	245.1	256.5
9	240.4	250.1
10	235.4	243.8
11	230.0	233.4

Table 2.1 Broadband and 11 µm brightness temperatures from LOWTRAN-7 runs involving thick cirrus clouds as a function of cloud top height.

2.4.2 Model Fits to Observations

In order to examine the consistency between the plane parallel model and observations, cloud optical depths (τ_p) and cloud fractions (f) are first inferred on a pixel-by-pixel basis to ensure a match between the calculations and observations. Once this is done for one year of observations, the resulting distributions of cloud optical depth are then examined. Separate analyses are carried out using both inhomogeneous ($f \leq 1$) and homogeneous ($f=1$) pixel approximations in Eq. (2.2). Provided diurnal and latitudinal biases in the observations are small, and provided cloud optical depths and cloud fractions are derived in a consistent manner at all μ_0, one would expect both of these parameters to remain constant with μ_0 since there are no other physical grounds for them to vary. Therefore, any systematic departure from this behavior would most likely be due to limitations in the plane parallel model approach.

Given the rather large field-of-view associated with ERBS scanner data, cloud fractions and cloud optical depths can only be inferred in a very approximate manner. Thus, the aim here is not to produce "climatologies" of cloud fraction and cloud optical depth, but rather to show that the conclusions drawn about the dependence of τ_p on μ_o are not sensitive to how cloud fraction is determined.

Initial estimates of cloud fraction (f) for the inhomogeneous approximation are obtained on a pixel-by-pixel basis from observed longwave and shortwave radiances from the following:

$$f_{LW} = \frac{(I_{LW}^{PIX} - I_{LW}^{CLR})}{(I_{LW}^{CLD} - I_{LW}^{CLR})} \tag{2.3}$$

$$f_{SW} = \frac{(I_{SW}^{PIX} - I_{SW}^{CLR})}{(I_{SW}^{CLD} - I_{SW}^{CLR})} \tag{2.4}$$

where I_{SW}^{PIX} and I_{LW}^{PIX} are observed shortwave and longwave pixel radiances, respectively, and I_{SW}^{CLR}, I_{LW}^{CLR}, I_{SW}^{CLD} and I_{LW}^{CLD} are representative shortwave and longwave clear and overcast radiances. In general, f_{SW} and f_{LW} will not be identical. Since shortwave radiances from cloudy scenes are affected by more degrees of freedom than are longwave radiances, more uncertainty in the shortwave estimate of cloud fraction is expected. However, if cloud top temperatures are very similar to the sea surface temperature, f_{LW} will tend to underestimate the cloud fraction, so that f_{SW} would likely be more representative. Therefore, an effective cloud fraction which uses both f_{LW} and f_{SW} is desirable since both of these values provide valuable information on cloud cover. Accordingly, estimates of cloud fraction (f) are obtained by simply averaging f_{LW} and f_{SW}. I_{SW}^{CLD} and I_{LW}^{CLD} were subjectively determined beforehand so as to ensure that the yearly mean value of f is 0.4 at all μ_o. This value was chosen based on one year of cloud fractions inferred using the ERBE MLE technique. I_{SW}^{CLR}

and I_{LW}^{CLR} were defined by the clear sky threshold values described earlier. For the homogeneous pixel approximation, an f of 1.0 is assumed for all pixels.

Once a value of cloud fraction has been obtained for a given pixel, the next step is to determine a cloud optical depth which ensures a match between the plane parallel reflectance and the pixel observation. Letting the observed shortwave reflectance equal R in Eq. (2.2), and using R^{CLR} to represent the clear sky reflectance, the corresponding reflectance from the cloudy portion of the pixel (R^{CLD}) is obtained. Next, this value is compared with the plane parallel model look-up tables of cloud reflectance and a 0.55 µm τ_p is inferred.

Figs. 2.4 (a) and (b) show contour plots of shortwave reflectance as a function of cloud optical depth and cloud fraction. As shown, many different cloud optical depth/cloud fraction combinations can yield the same reflectance, and the reflectance sensitivity to these parameters also appears to depend on μ_0—it is more pronounced at $\mu_0 = 0.55$ than at $\mu_0 = 0.15$. Thus, by using two very different approximations such as the inhomogeneous and homogeneous pixel approximations, a wide range of possible cloud fraction/τ_p combinations are accounted for. In the inhomogeneous pixel approximation, f varies from pixel to pixel along with cloud optical depth (τ_{nh}), while in the homogeneous pixel approximation, cloud fractions are fixed at unity and the cloud optical depth (τ_h) consequently tends to be much lower than τ_{nh}.

In order to account for uncertainties due to clear sky effects above/below the cloud layer, comparisons between observations and calculations are performed using cloud top heights of 3 km and 6 km, and for the case where clear sky effects are ignored.

2.4.3 Error Analysis

Uncertainties in mean reflectance due to sampling errors are calculated from the standard error in the mean, taking into account the high degree of spatial correlation

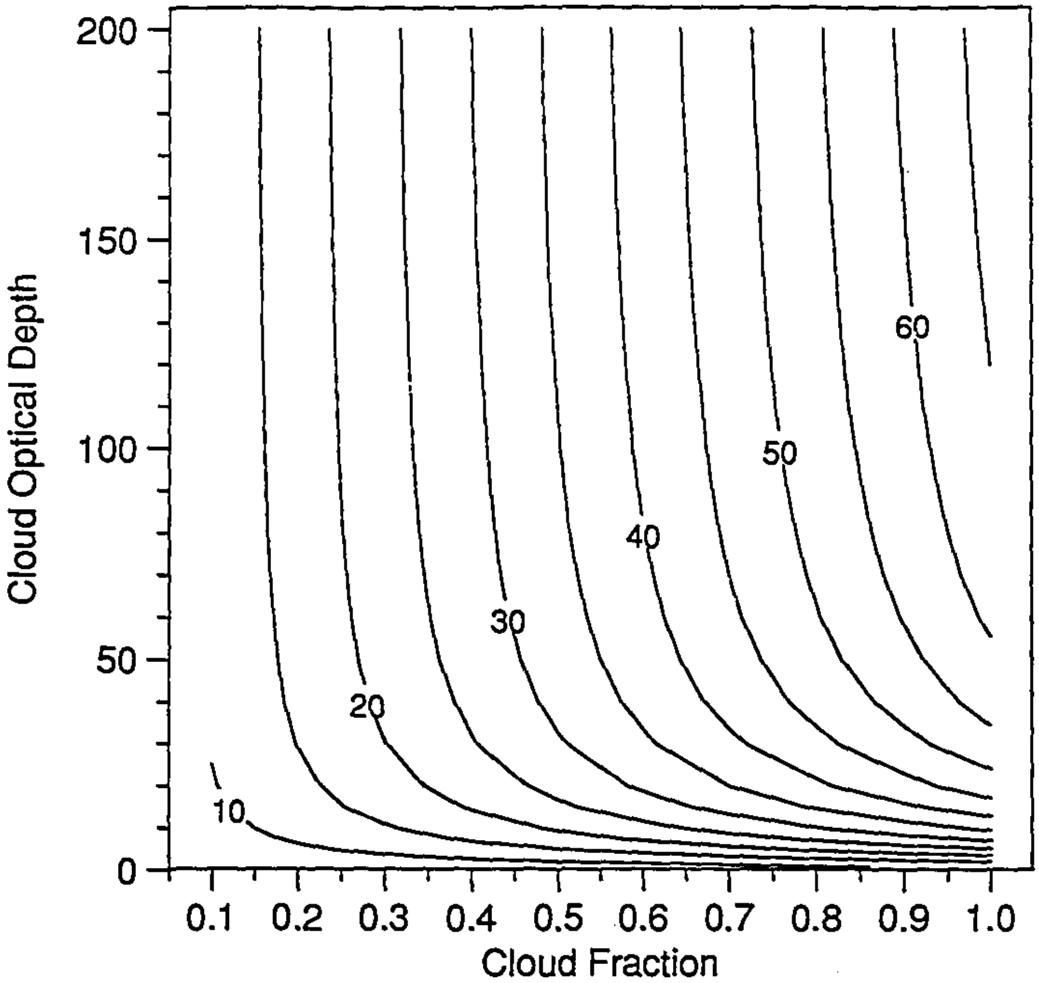

200
150
100
50
0
Cloud Optical Depth
0.1 0.2 0.3 0.4 0.5 0.6 0.7 0.8 0.9 1.0
Cloud Fraction
10
20
30
40
50
60

(a)

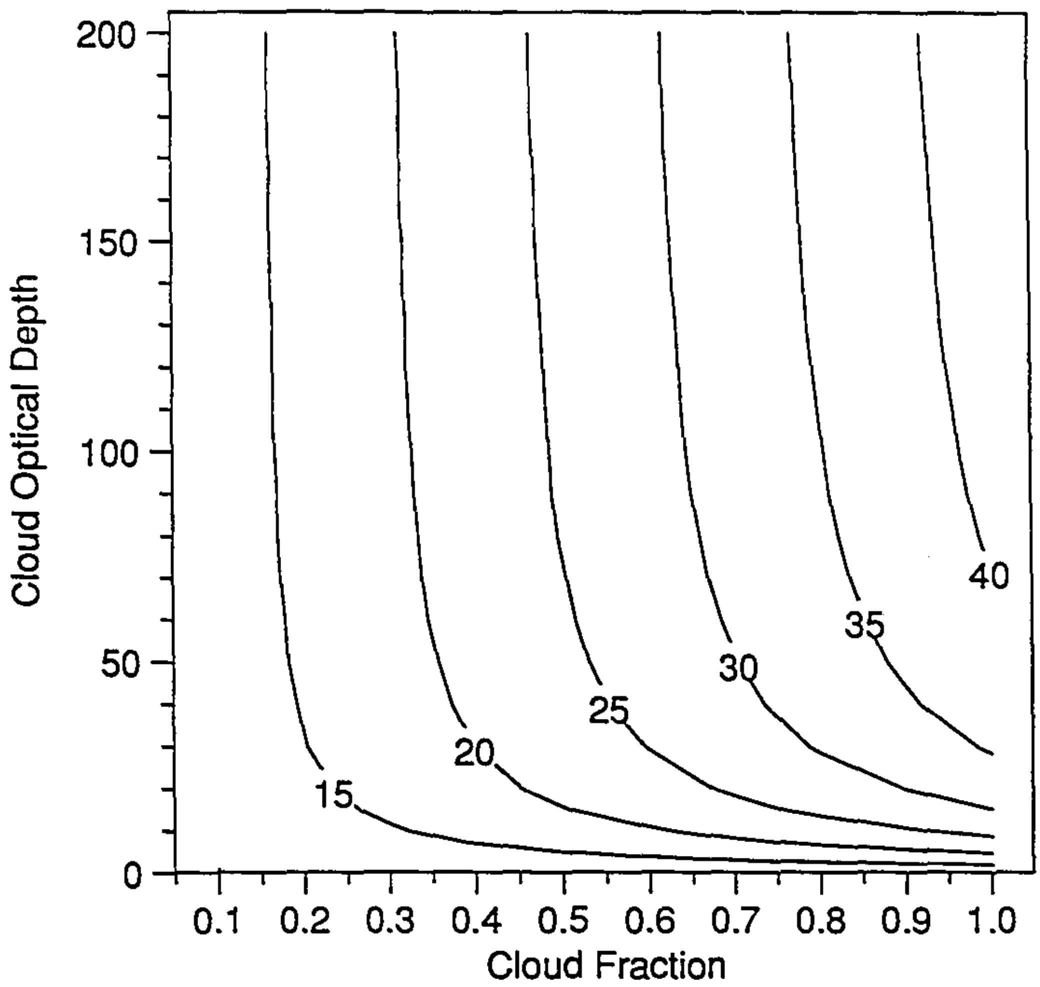

(b)

Figure 2.4 Contours of calculated shortwave reflectance at nadir as a function of cloud optical depth and cloud fraction for (a) μ_0=0.55 and (b) μ_0=0.15 for a cloud top height of 3 km.

between pixels, which gives rise to a correlation radius of ≈500 km. Based on Davies (1994) the error in the mean reflectance can be obtained from:

$$E = \pm\frac{\sigma}{\sqrt{N}}\left\{1+2\sum_{r=1}^{N-1}\left(1-\frac{r}{N}\right)\rho(r)\right\}^{1/2} \tag{2.5}$$

where σ is the standard deviation for N observations, and ρ(r) is the autocorrelation at lag r given by:

$$\rho(r) = \frac{\mathrm{cov}(I_i, I_{i+r})}{\sigma(I_i)\sigma(I_{i+r})} \tag{2.6}$$

$\mathrm{cov}(I_i, I_{i+r})$ is the covariance in radiance for fields-of-view along the satellite track r pixels apart.

Because of the very large number of observations used in this study (N>500,000), errors in mean reflectance tend to be quite small—generally less that 0.15% in absolute reflectance. Consequently, in most of the graphs of mean reflectance that follow, error bars have not been included. Uncertainties in reflectance frequency distributions were also small, at less than 1%.

Estimates of cloud optical depth for any given scene will tend to suffer from rather large uncertainties given the complexity of cloud scenes at scales as large as the ERBS pixel. The largest uncertainty will lie in the estimate of cloud fraction—simple threshold techniques become less reliable in general as pixel resolution decreases (Wielicki and Parker, 1992). Other sources of uncertainty include the effect of attenuation above the cloud top by the atmosphere, uncertainties in cloud microphysics, uncertainties due to the use of a lower spectral resolution, and uncertainties due to the Lambertian model used to calculate reflection contributions from the ocean surface below the cloud layer. For the purpose of this study, however, the most important errors are those which show a systematic dependence on μ_0. Such model bias errors would tend to obscure any systematic differences between the observations and calculations with μ_0 which may be attributable to inherent limitations of the plane parallel model assumption. In the following section, it is demonstrated that regardless of how the plane parallel calculations are carried out, bias errors due to the plane parallel model assumption tend to dominate.

2.5 Results

Before making direct comparisons between the observations and plane parallel calculations, it is useful to first examine the observations alone. Fig. 2.5 shows average observed reflectances versus μ_0 for all pixels throughout the year ("All Obs"), for pixels which were not rejected as being clear or containing thick ice clouds ("Obs Analyzed"), and when clear pixels were not included ("No Clr"). In all cases, the reflectance appears to increase with decreasing μ_0. Reflectances for the "Obs Analyzed" case are lower than the other two cases because excluding thick ice clouds tends to lower the average reflectance. Since the relative dependence of the observed shortwave reflectance on μ_0 shows very little change regardless of whether or not thick ice clouds are included, it is unlikely that the presence of undetected thin or partly cloudy ice clouds will influence this dependence either. The tendency for reflectances to increase as μ_0 decreases is also very apparent in the reflectance frequency distributions. This is illustrated in Fig. 2.6 which shows reflectance frequency distributions for various μ_0 values (for the "Obs Analyzed" case). The frequency distributions are rather similar for $\mu_0 > 0.5$, but as μ_0 decreases, the peak in the distributions tends to occur at progressively higher reflectance values, and the distributions tend to broaden rather dramatically.

In order to test whether or not this behavior in the observed reflectance is attributable to diurnal effects, the observations were stratified according to whether they occurred in the morning or afternoon, local time. This comparison, shown in Fig. 2.7, reveals that while the morning and afternoon reflectances are statistically different for moderate-high solar elevations, they are in close agreement at low elevations, and both morning and

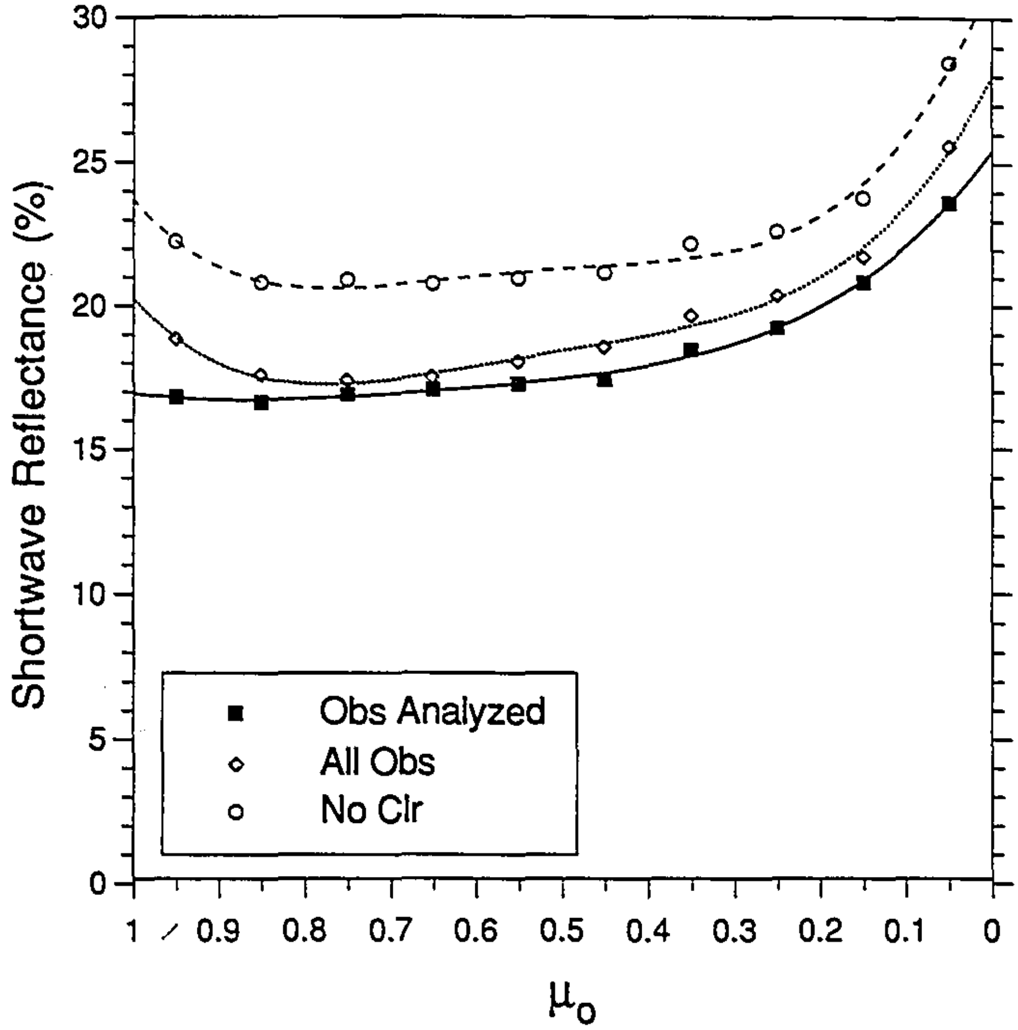

Figure 2.5 One year average observed shortwave reflectances versus μ_o for pixels which were not rejected as being either clear or containing thick ice clouds ("Obs Analyzed"), for all observations throughout the year ("All Obs"), and for pixels not rejected as clear ("No Clr").

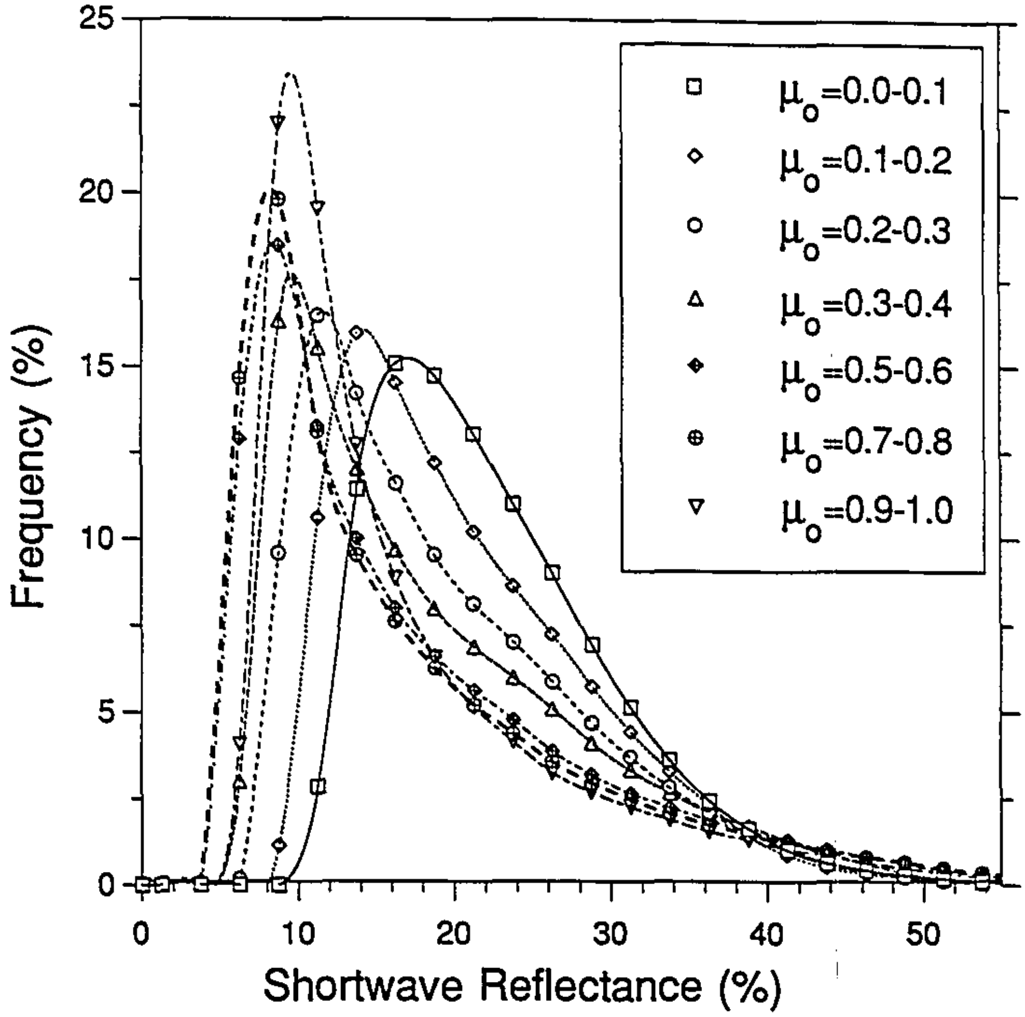

Figure 2.6 Observed shortwave reflectance frequency distributions at μ=0.9-1.0 for various μ_o bins for observations not rejected as being either clear or containing thick ice clouds.

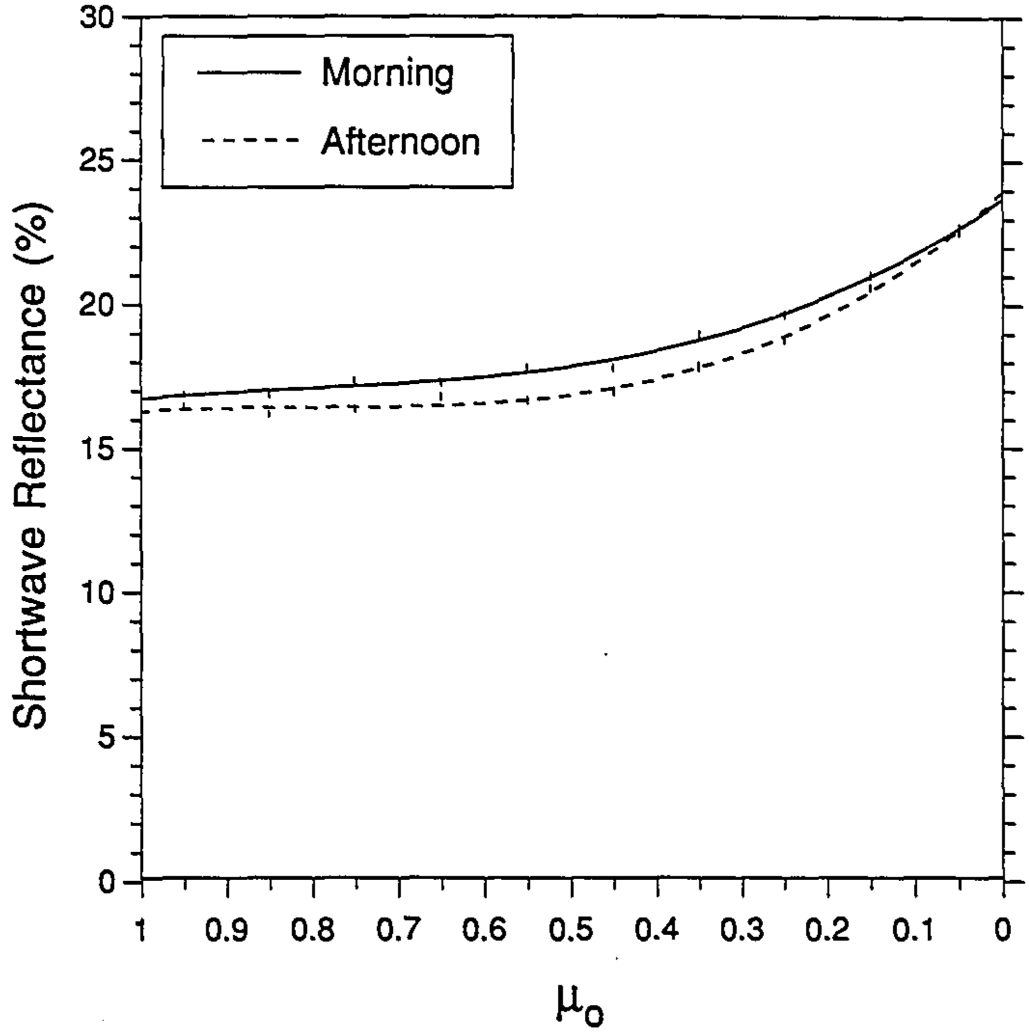

Figure 2.7 One year average observed shortwave reflectances versus μ_o for pixels which were not rejected as being either clear or containing thick ice clouds stratified by morning and afternoon local time.

afternoon reflectances show a similar systematic increase with decreasing μ_0. The fact that the morning observations appear to be slightly larger than afternoon values is consistent with results from other satellite-based studies on the diurnal behavior of cloud properties over ocean (Minnis and Harrison, 1984; Hartmann and Recker, 1986). Overall, these studies have found a maximum in low level cloudiness and a minimum in cloud-top temperature during the morning, and a minimum in cloudiness and a maximum in cloud-top temperature during the late afternoon. They note, however, that diurnal effects over ocean are much less pronounced than those over land. Thus, while weak diurnal effects are indeed present in oceanic observations, they are not the main reason for the increase in reflectance with decreasing μ_0 shown here.

In order to examine whether latitudinal biases are present in the observations, observations were also stratified according to whether they fall in the 0°–15° or 15°–30° latitude ranges. This is illustrated in Fig. 2.8 which shows the fraction (in percent) of pixels lying in both these latitude bins. For $\mu_0 < 0.6$, the proportion of pixels from both these latitude ranges is reasonably constant. Approximately 55% of the pixels fall in the 15°–30° latitude range, while about 45% lie between 0° and 15°. Not surprisingly, when the sun is closer to zenith, a much larger fraction of pixels occurs in the 0°–15° latitude range. Despite this oversampling, there does not appear to be any significant effect on the observed reflectance frequency distributions in Fig. 2.6—at $\mu_0 = 0.9$–1.0, the reflectance frequency distribution appears to be quite similar to those at intermediate μ_0 (where the fraction of samples in the 0°–15° latitude range is much lower). The marked differences in the reflectance frequency distributions for $\mu_0 < 0.6$ cannot therefore be attributed to latitudinal effects since the latitudinal sampling appears nearly constant there.

Since neither diurnal nor latitudinal effects have a significant influence on the observed frequency distributions, the intrinsic cloud properties of this data set should not depend on μ_0. Further, for the plane parallel assumption to be applicable, we would expect

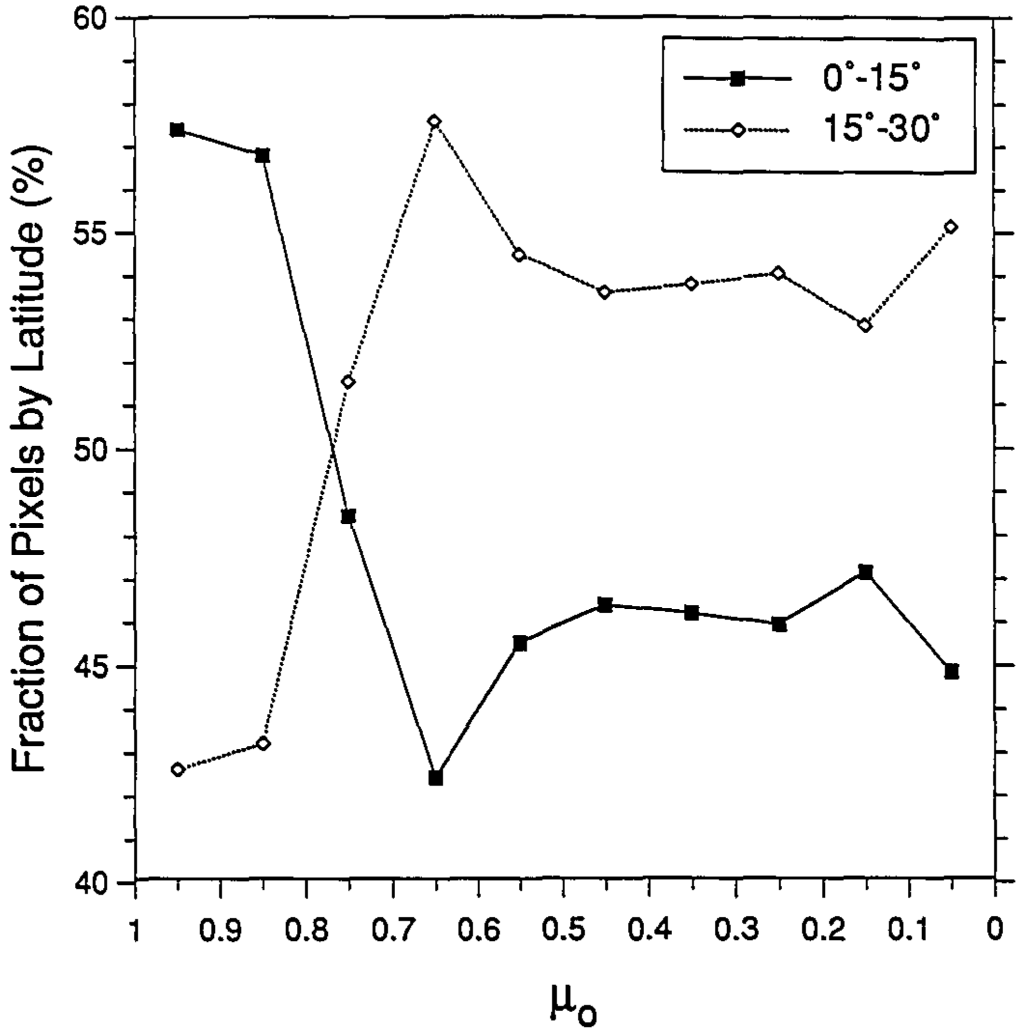

Figure 2.8 Fraction of nadir observations falling between the 0°-15° and 15°-30° latitude zones.

the model reflectance dependence on μ_0 for constant τ_p to agree with the observations. When constant cloud fraction and cloud optical depth values are used in plane parallel model calculations for different μ_0, an interesting result occurs. Fig. 2.9 shows plane parallel model reflectance calculations at nadir for a cloud optical depth of 10 and a cloud fraction of 1.0 for three different conditions: (i) a cloud top of 3 km; (ii) a cloud top height of 6 km; and (iii) when clear sky effects above and below the cloud are not included in the calculation. The lower altitude clouds have smaller reflectances because of increased attenuation by the atmosphere above the cloud top. In each case, calculated reflectances decrease with decreasing μ_0. This result is in stark contrast to the observations.

The tendency for the plane parallel model reflectances to decrease with decreasing μ_0 also appears to become more pronounced for thicker clouds. Fig. 2.10 shows plane parallel reflectance calculations as a function of τ_p for $\mu_0 = 0.15$ and $\mu_0 = 0.5$ for the same cloud models as in Fig. 2.9. For small τ_p very little dependence on μ_0 is observed, but as the cloud gets thicker, reflectance differences tend to increase substantially. At small τ_p, slight errors in the calculations are expected due to uncertainties associated with the use of the Lambertian model in calculating reflection contributions from the ocean surface below the cloud layer. The largest uncertainties would likely occur at Sun-Earth-satellite geometries where sun glint from the ocean surface is a maximum. At nadir, this effect would tend to be most pronounced for overhead sun, and would be negligible at small μ_0 (Koepke and Quenzel, 1979). Thus, while inclusion of sun glint in the calculations might cause a slight increase in reflectance at overhead sun, it would not alter the tendency for the reflectance to decrease with decreasing μ_0.

Because of these rather marked differences in the relative dependence of reflectance on μ_0 between the observations and calculations, cloud optical depths inferred using the plane parallel assumption are fundamentally flawed at low sun elevations, regardless of what assumptions are made regarding sub-pixel cloud fraction. Fig. 2.11 shows one-year

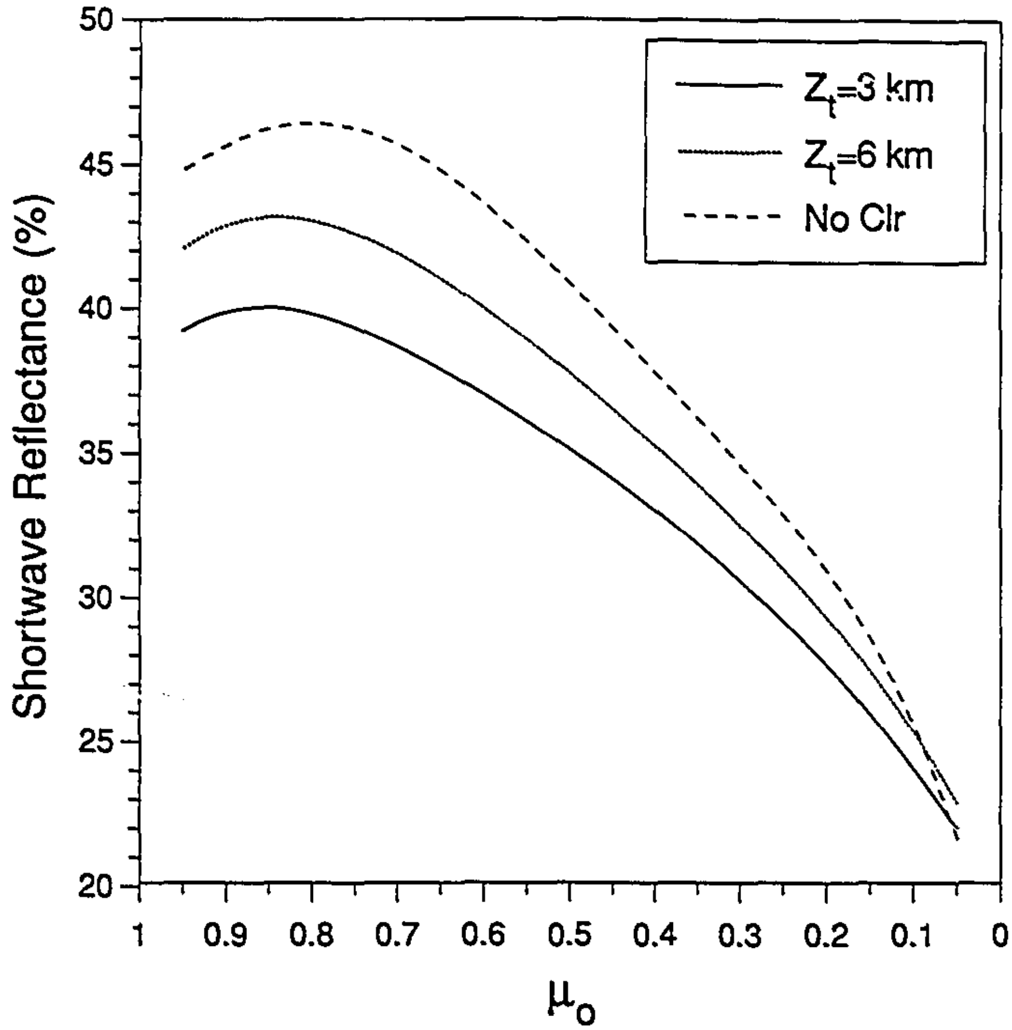

Figure 2.9 Broadband shortwave reflectance calculations vs μ_o for a cloud with optical depth 10, cloud fraction 1, and cloud top heights of 3 km and 6 km, as well as for the case where clear sky effects above and below the cloud are not included in the calculation.

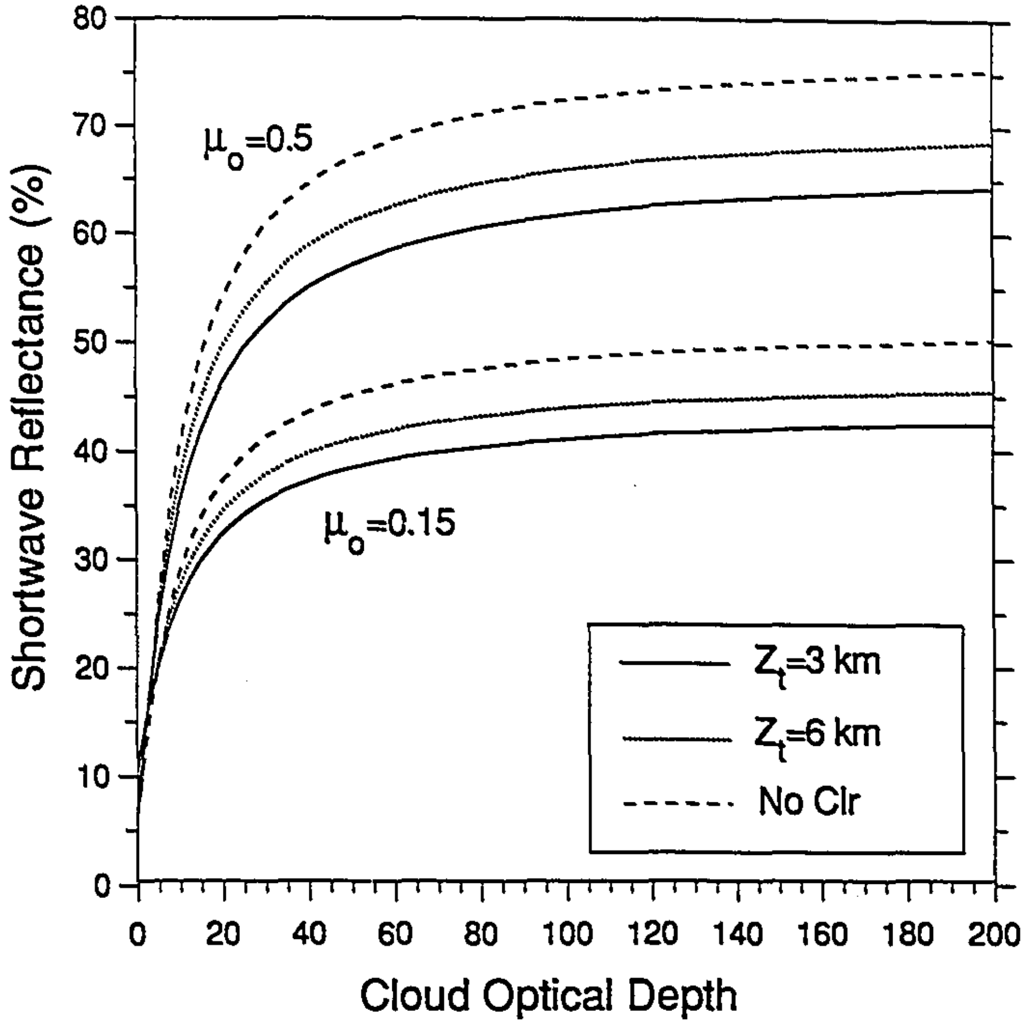

Figure 2.10 Broadband shortwave reflectance calculations vs cloud optical depth for μ_o=0.5 (top three curves) and μ_o=0.15 (bottom three curves) for cloud top heights of 3 km and 6 km, as well as for the case where clear sky effects above and below the cloud are not included in the calculation.

average values of τ_p as a function of μ_o for both the inhomogeneous ("Inhom") and homogeneous ("Hom") pixel approximations (for a representative cloud-top altitude of 3 km). In the inhomogeneous pixel approximation, cloud fractions were derived from thresholds which were pre-selected so as to ensure a constant yearly mean cloud fraction of 0.4, while for the homogeneous approximation, a constant cloud fraction of 1.0 was assumed for all cloudy pixels. For the inhomogeneous case, τ_{nh} depends most strongly on μ_o for μ_o<0.45. Between μ_o≈0.95 and μ_o≈0.55, τ_{nh} increases gradually from ≈6 to ≈9, and then increases rapidly to ≈100 at μ_o≈0.05. By comparison, the μ_o dependence in cloud optical depth is less pronounced for the homogeneous pixel approximation. Between μ_o≈0.95 and μ_o≈0.25, τ_h increases from ≈3 to ≈5, and reaches ≈18 for μ_o≈0.05. Note that cloud optical depths are likely underestimated by at least a factor of 2 for this case since sub-pixel cloud fractions are not accounted for.

The larger increase in τ_{nh} for the inhomogeneous case is expected since, as shown in Fig. 2.10, calculated reflectances tend to show a much greater sensitivity to μ_o when τ_p is larger. To demonstrate the dependence of average τ_p on μ_o more systematically, the τ_p values were divided into different classes of occurrence of cloud optical depth. Fig. 2.12 shows analogous results to Fig. 2.11, but for each class of occurrence. Here the 0-50% line represents the average τ_p for cloud optical depths lying below the 50th percentile (i.e. over the smallest half of each cloud optical depth distribution), the 50-75% line represents the average τ_p for optical depths lying between the 50th and 75th percentiles, etc. The increases in both τ_h and τ_{nh} with decreasing μ_o tend to be small for the lower classes of τ_p (optical depths ≤ 6), while they are much more pronounced for the largest classes. In fact, the rise in τ_p with decreasing μ_o is extremely large at all solar zenith angles for classes with $\tau_p \geq 12$ at μ_o≈ 0.95. For these cases, cloud optical depths more than double between $\mu_o = 0.95$ and $\mu_o = 0.45$. This occurs for the inhomogeneous pixel approximation

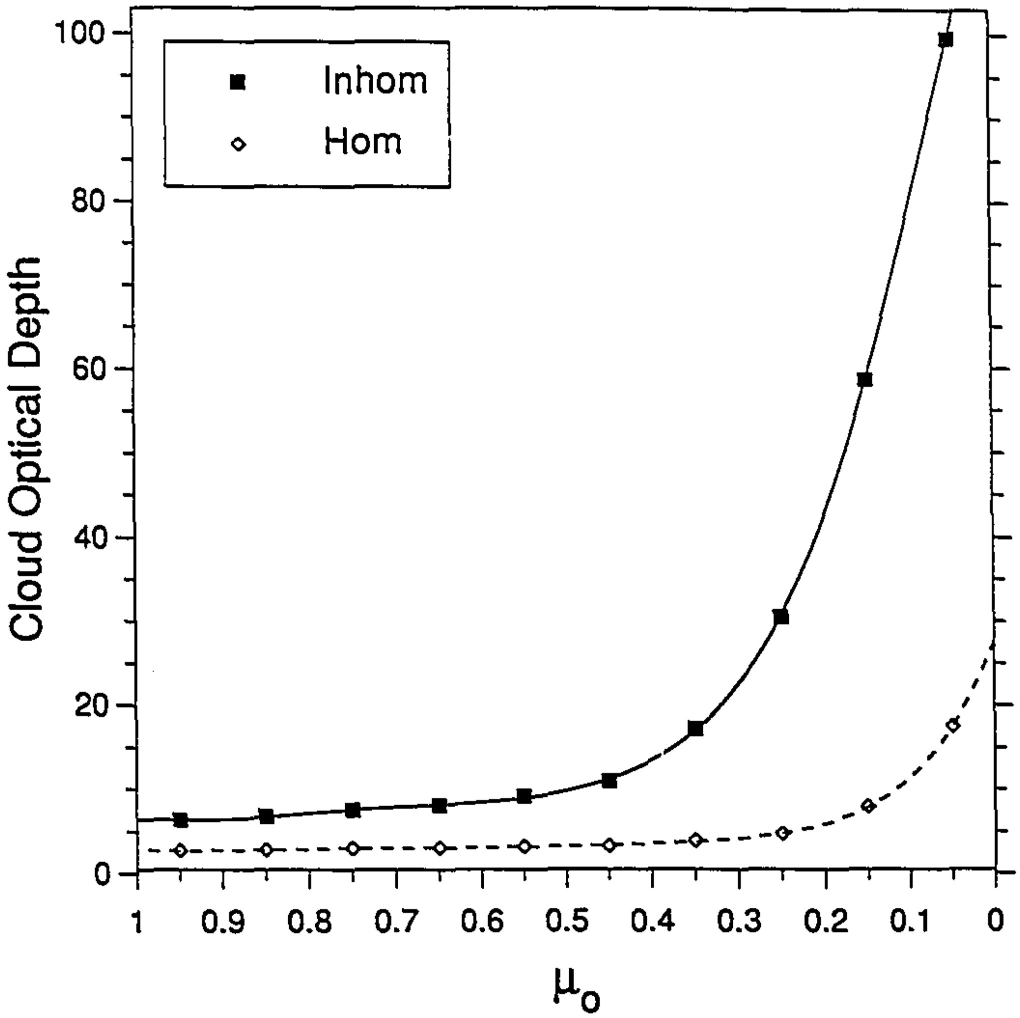

Figure 2.11 One year average cloud optical depth vs μ_o obtained using the inhomogeneous and homogenous pixel approximations.

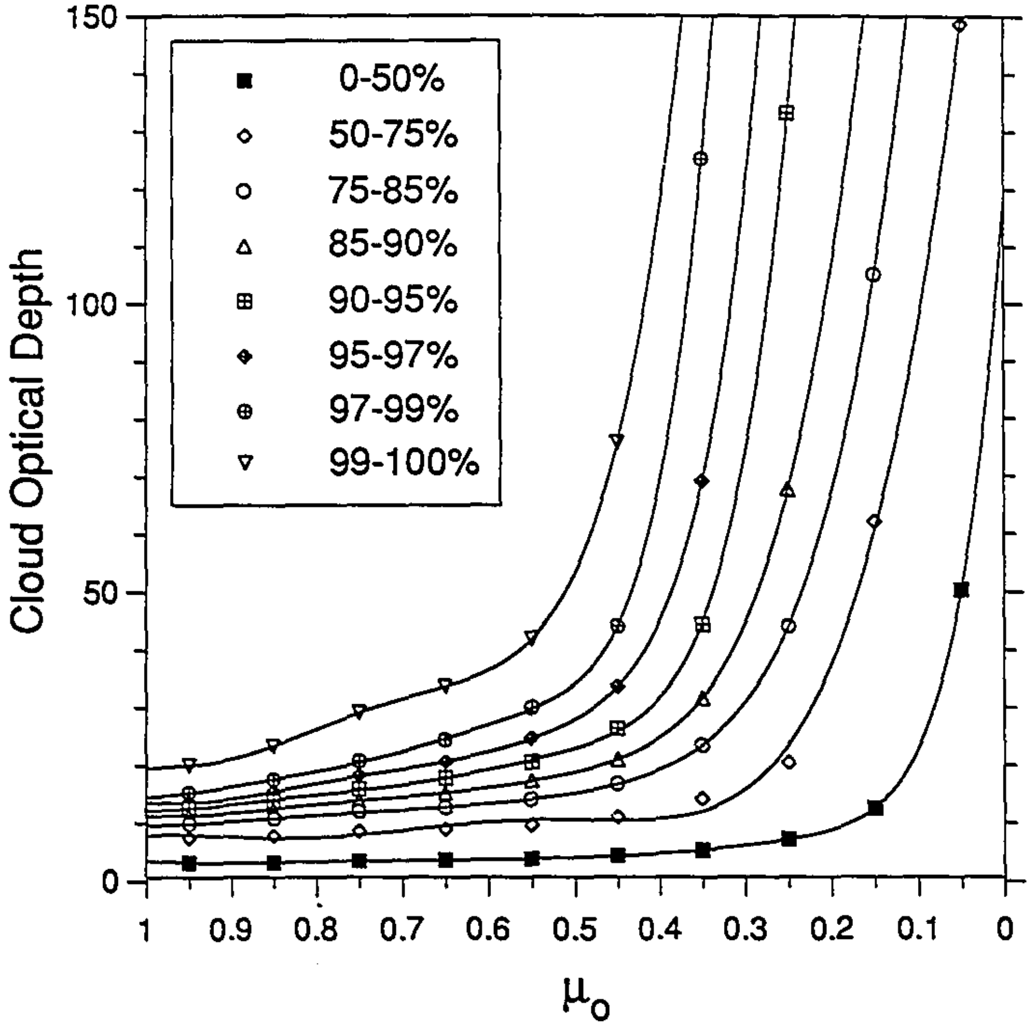

150
100
50
0
Cloud Optical Depth
0-50%
50-75%
75-85%
85-90%
90-95%
95-97%
97-99%
99-100%
1
0.9
0.8
0.7
0.6
0.5
0.4
0.3
0.2
0.1
0
μ_o

(a)

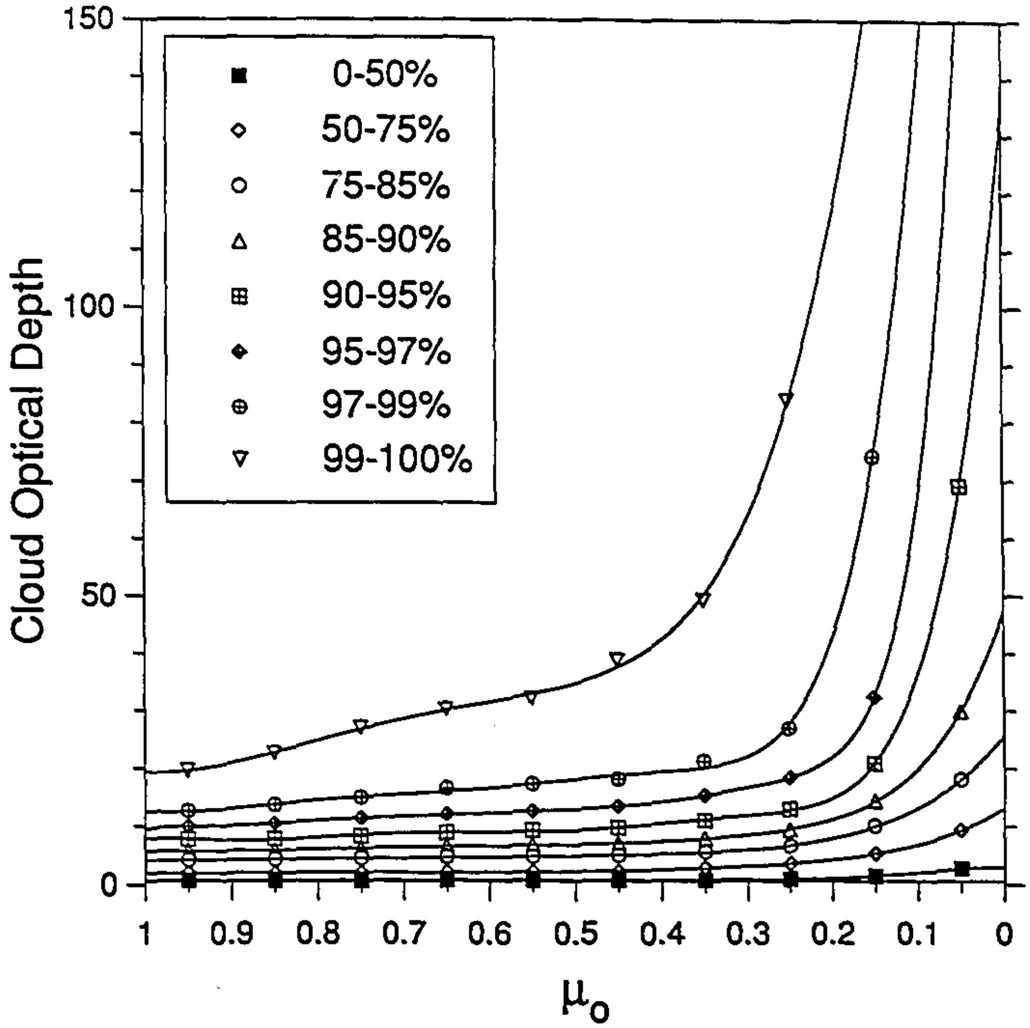

(b)

Figure 2.12 Cloud optical depth averages for different classes of occurrence for (a) the inhomogeneous pixel approximation and (b) the homogeneous approximation. Each line represents an average cloud optical depth for samples lying between the indicated percentile interval.

(Fig. 2.12 (a)) for the (optically) thickest 10% of the clouds, and in the homogeneous pixel approximation (Fig. 2.12 (b)) for the (optically) thickest 1% (99-100% class).

Figs. 2.13 (a) and (b) show the cloud fraction and τ_p frequency distributions resulting from the comparison between the inhomogeneous pixel approximation with the observations. In Fig. 2.13 (a), only pixels identified as cloud-contaminated were included in the cloud fraction frequency distribution. While thresholds were pre-selected to provide an overall average cloud fraction of 0.4 at all μ_o (based on ERBE MLE cloud fractions), no other constraints on the relative frequency distribution were imposed. As shown, the cloud fraction distributions appear quite similar for all μ_o. This is expected since, on average, cloud fraction should be independent of μ_o in the absence of strong latitudinal and diurnal effects. In contrast, τ_p frequency distributions in Fig. 2.13 (b) show a systematic shift towards higher τ_p as μ_o decreases. In fact, for very oblique sun, the frequency of pixels with τ_p >150 was found to be extremely large. This is shown in Fig. 2.14 for the various cloud models considered. For the inhomogeneous approximation, τ_p >150 occurs as much as 50% of the time for μ_o between 0.0 and 0.1 and drops to 0% for μ_o greater than 0.4. This behavior is also observed when the homogeneous pixel approximation is applied. In this case, approximately 5% of the pixels at very oblique sun were found to have τ_p >150.

When the observed reflectance was large, it was interesting to note that the reflectances sometimes exceeded the plane parallel calculations regardless of the cloud fraction or cloud optical depth used in the calculations. As an example, Fig. 2.15 shows a case for a single pixel observation where the reflectance was 54.7%, for μ_o=0.14, μ=0.98 and ϕ=131°. When plane parallel calculations were carried out for f=1, cloud optical depths up to 1000, and three different assumptions of cloud top height, the observed value exceeded the plane parallel value by at least 21% when a cloud top height of 3 km was used, 16% for a cloud top of 6 km, and by 9% when no atmosphere was included

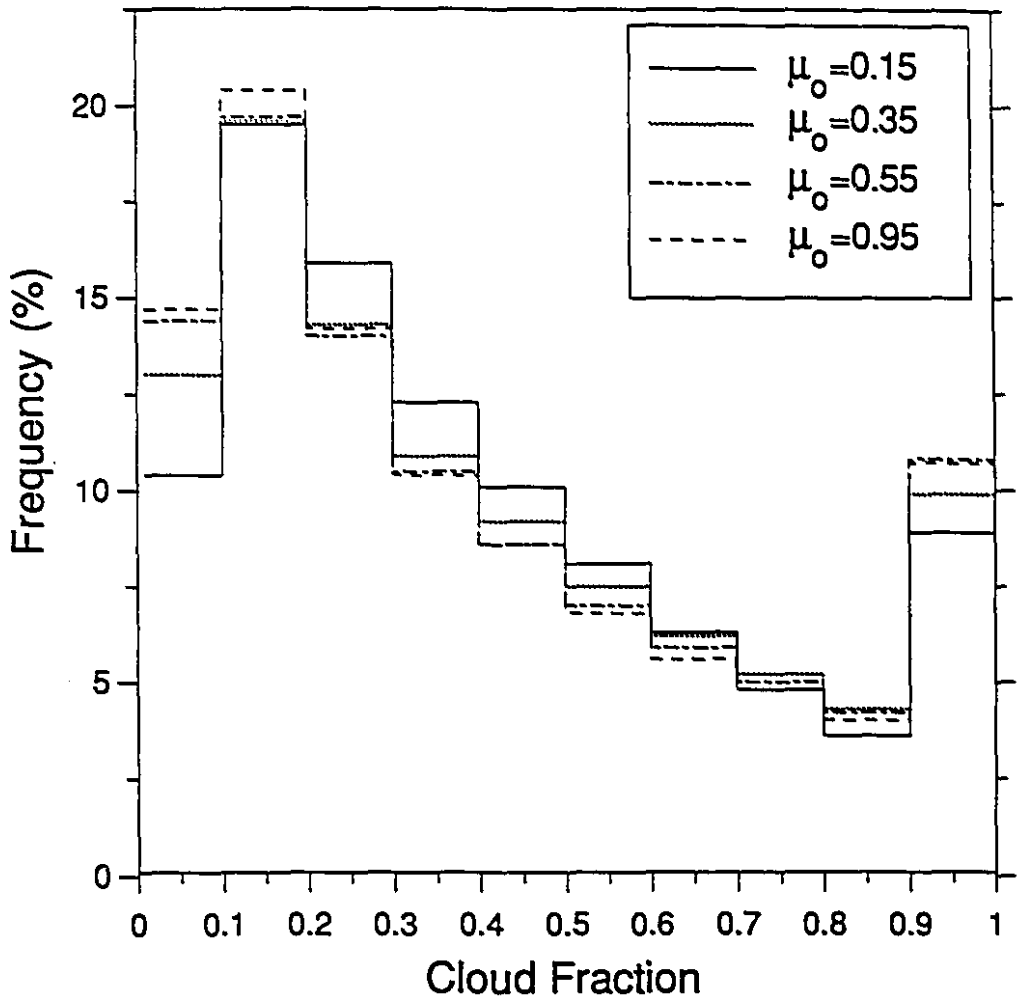

μ_o=0.15
μ_o=0.35
μ_o=0.55
μ_o=0.95
Frequency (%)
0
5
10
15
20
0
0.1
0.2
0.3
0.4
0.5
0.6
0.7
0.8
0.9
1
Cloud Fraction

(a)

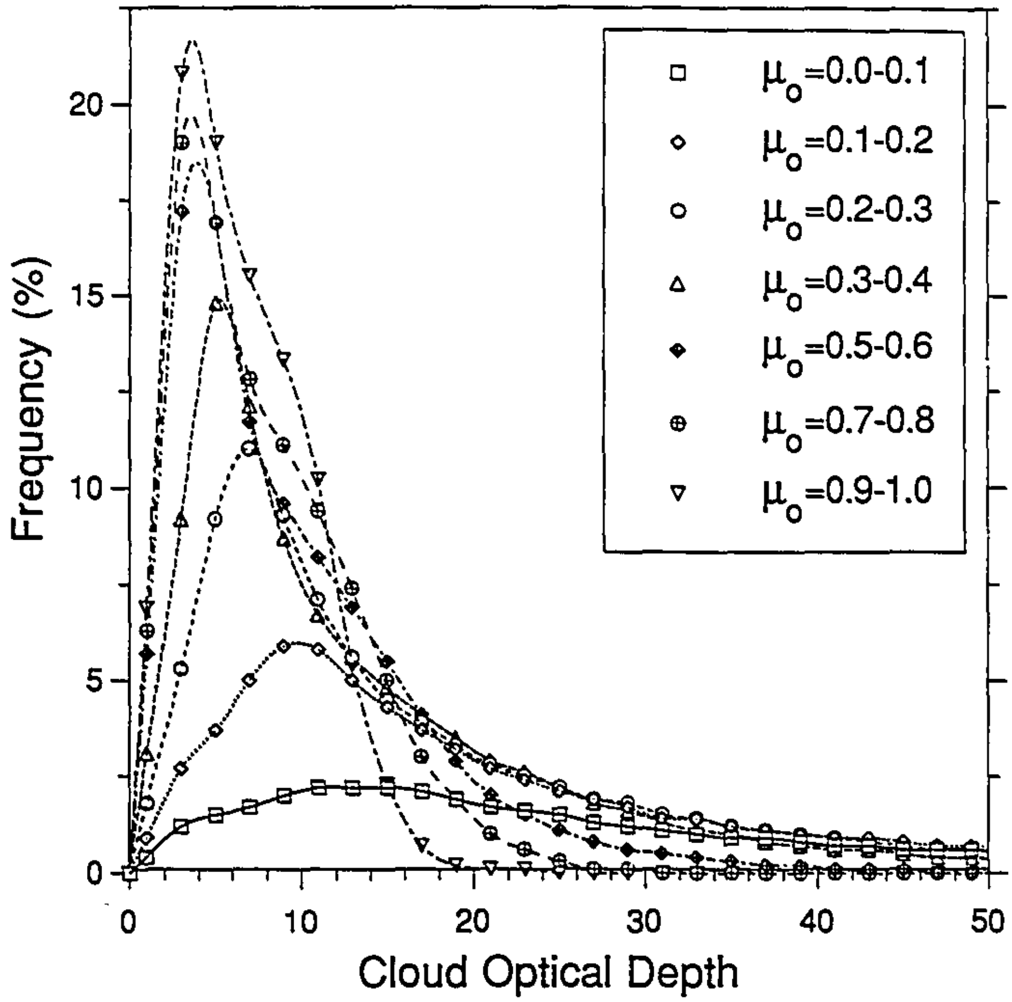

(b)

Figure 2.13 One year (a) cloud fraction and (b) cloud optical depth frequency distributions for various μ_0 obtained using the inhomogeneous pixel approximation.

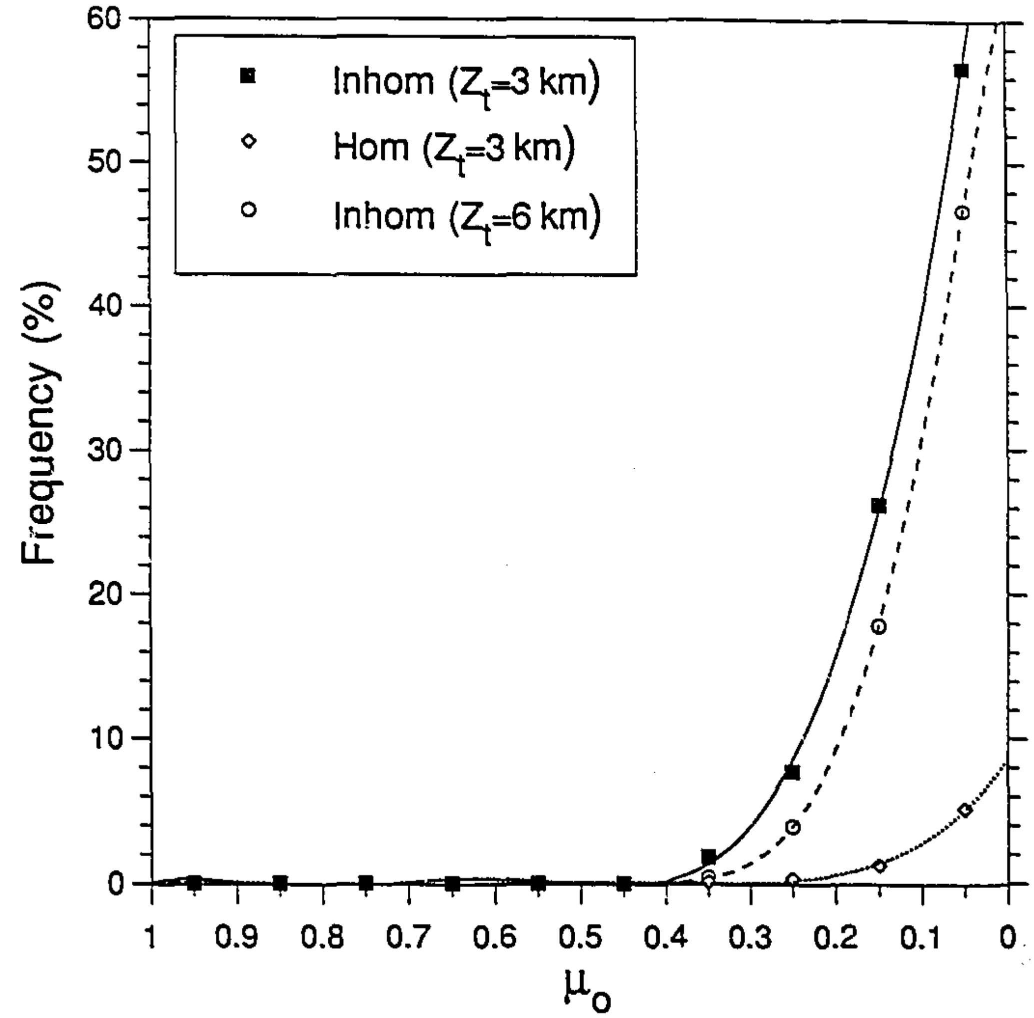

Figure 2.14 The frequency of pixels with cloud optical depths >150 vs μ_o for the inhomogeneous pixel approximation for cloud top heights of 3 km and 6 km, and for the homogeneous pixel approximation for a cloud top height of 3 km.

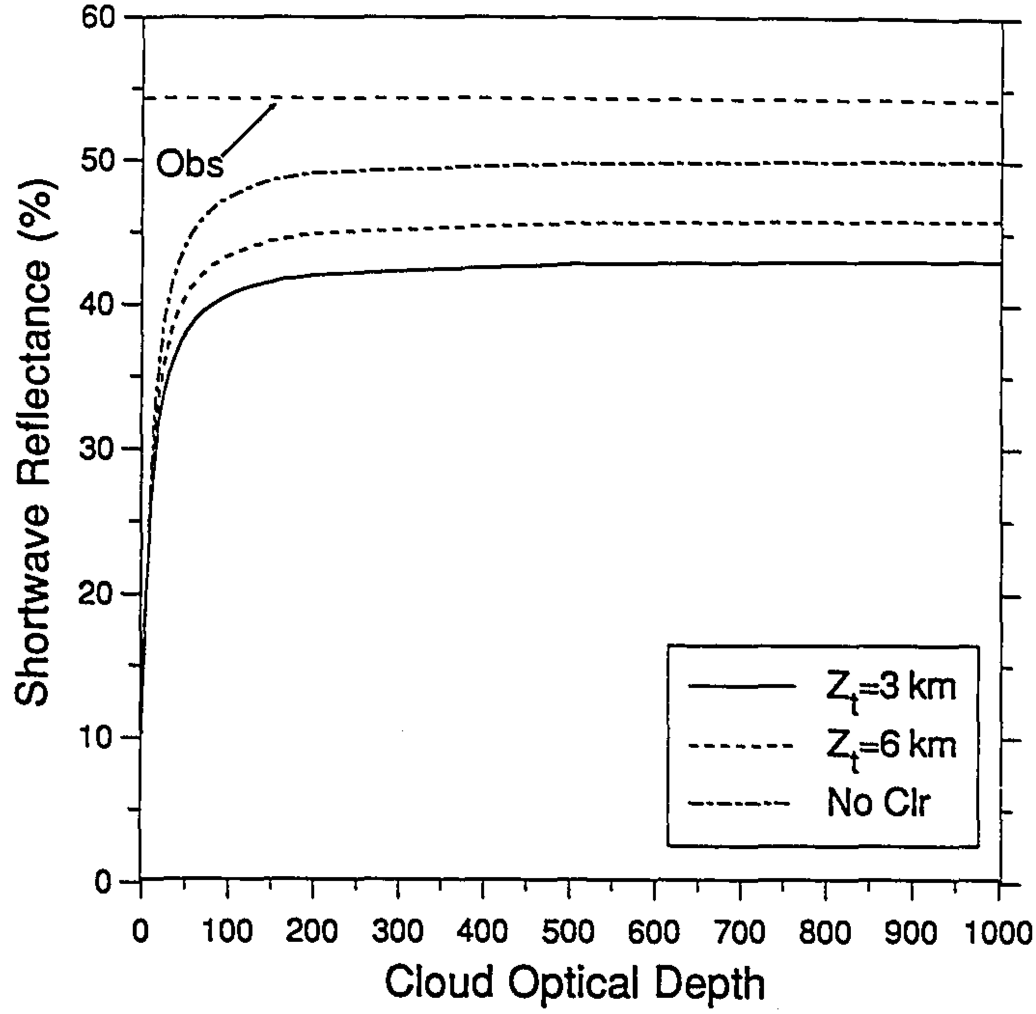

Figure 2.15 Comparison between shortwave reflectance calculations vs cloud optical depth and an observation at μ_o=0.14, μ=0.98 and ϕ=131° (dashed line). Calculations were performed using a cloud fraction of 1.0 and cloud top heights of 3 km and 6 km, as well as for the case when clear sky effects above and below the cloud are not included in the calculation.

above/below the cloud. The occurrence of such cases tended to be restricted to small μ_0 and occurred more frequently as μ_0 decreased.

In order to assess the overall uncertainty in average reflectance due to the μ_0 bias in cloud optical depth, the average observed reflectances were compared with calculated values obtained using only the cloud optical depths and cloud fractions inferred at zenith sun. That is, using the τ_p and f distributions in the $\mu_0 = 0.9$–1.0 bin, average nadir reflectances were calculated at other values of μ_0 and compared directly with the observations. Since the same set of cloud optical depths are used at all μ_0, any differences between the observations and calculations will primarily be due to the optical depth bias. Fig. 2.16 shows the results of this comparison. As expected, large differences between the observed and calculated average reflectances occur as μ_0 decreases. For $\mu_0>0.6$, relative differences in reflectance are less 10%, on average, and increase to ≈30% at very oblique sun angles. When these results are further stratified according to pixel brightness, the differences can be even larger. Fig. 2.17 shows average observed and calculated reflectances separately for samples lying above and below the median reflectance (as deduced from the reflectance frequency distributions used to calculate the means in Fig. 2.16). For the darkest 50% of the samples, the plane parallel model appears to provide reasonable estimates of the reflectance at moderate to high solar elevations, but is in error by more than 10% for $\mu_0<0.45$. For the brightest 50%, however, the discrepancy between observed and plane parallel model reflectances reaches ≈10% for $\mu_0 < 0.6$, rising to ≈37% for $\mu_0 = 0.1$. For the brightest 1% of the population, differences as high as 50% were found (not shown here).

Note that the increase in calculated reflectance with decreasing μ_0 for the darkest 50% is due to the larger relative contribution from the clear sky sub-pixel component. For the darkest scenes, the cloud fractions are generally small and the clouds are thin, so that even though the plane parallel model reflectance of thin clouds decreases slightly with

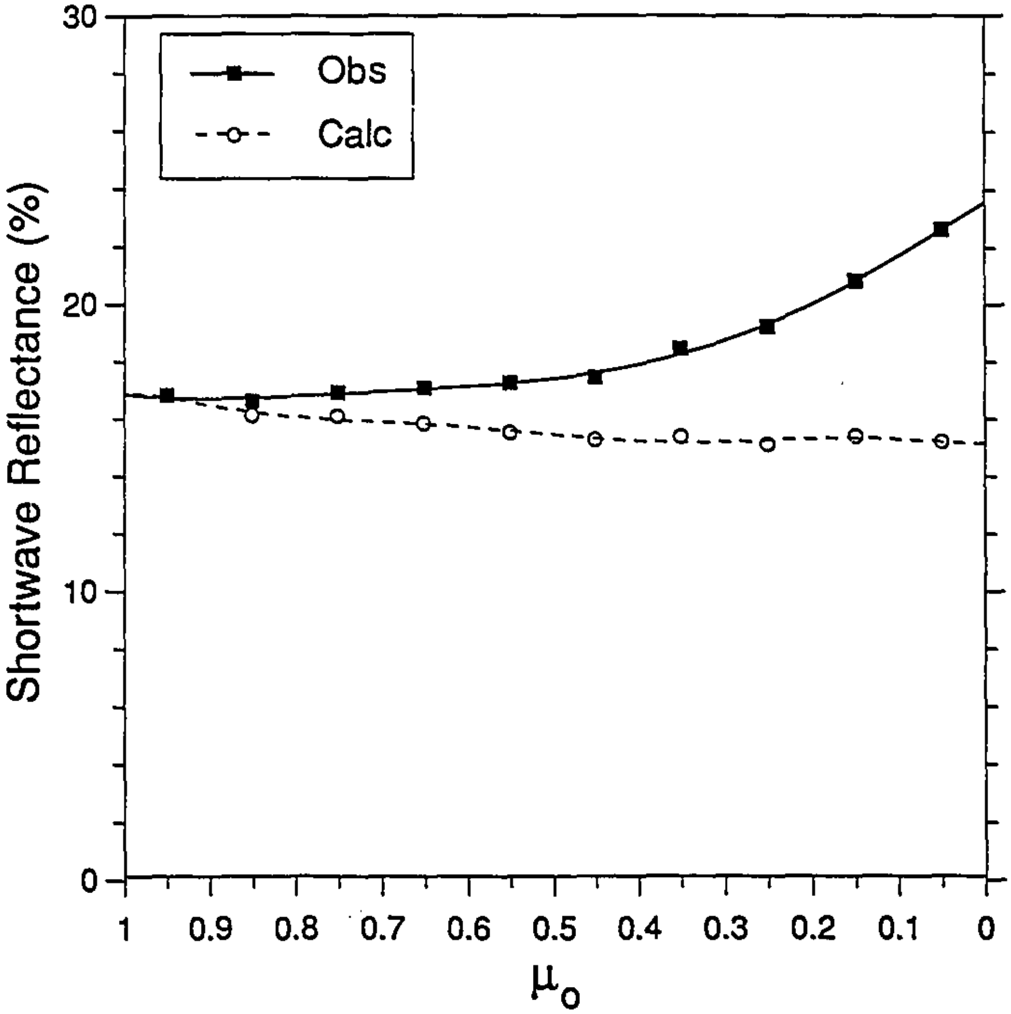

Figure 2.16 Average reflectance vs μ_o for the observations, and for calculations derived using cloud optical depths and cloud fractions from the μ_o=0.9-1.0 bin.

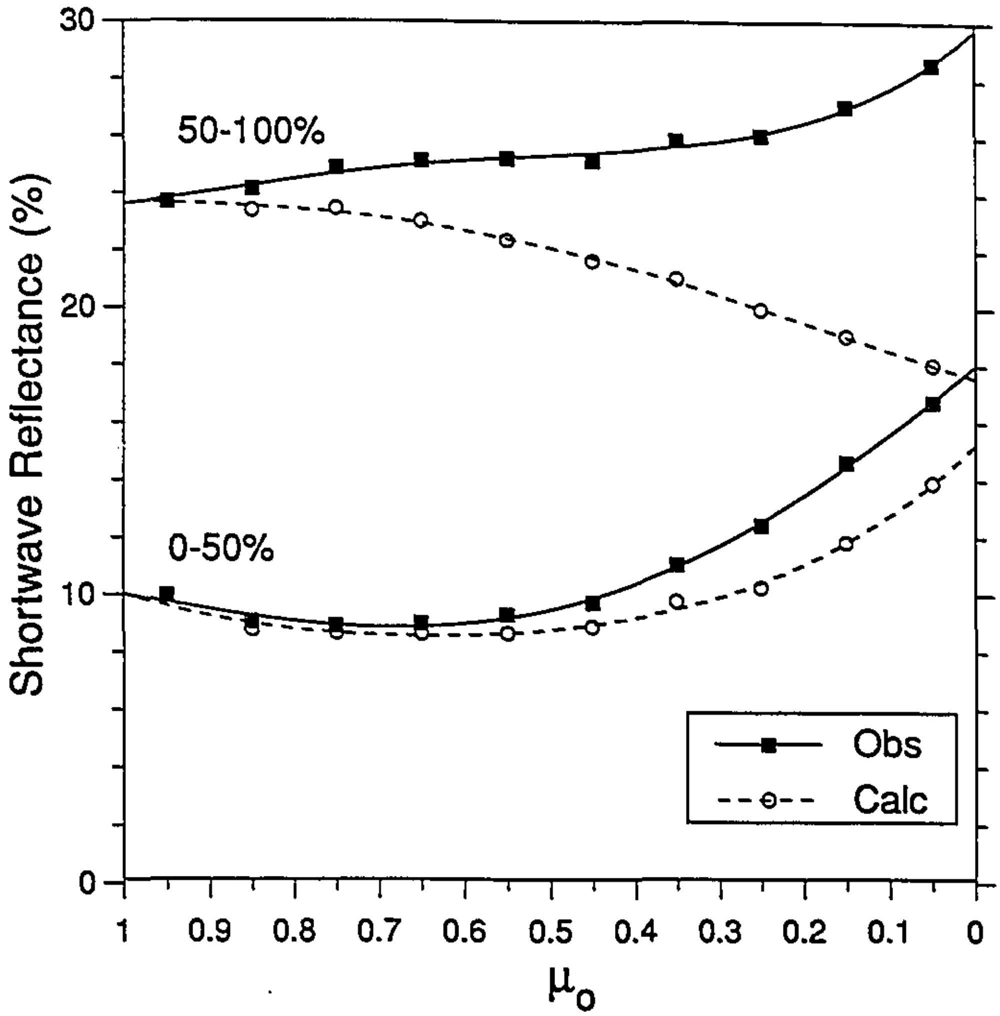

Figure 2.17 Same as Fig. 2.16 but for reflectances lying below the 50th percentile (0-50%) and for pixels lying between the 50th and 100th percentiles (50-100%).

decreasing μ_0, the cloud contribution to the μ_0 dependence in reflectance is not strong enough to reverse the trend of the clear sky contribution.

2.6 Discussion

The tendency for observed nadir reflectances to exceed plane parallel calculations as the sun angle becomes more oblique can also be observed by close examination of results from a limited number of studies in the literature. Unfortunately, past observational studies have tended to be restricted to measurements from satellites in Sun-synchronous orbits, resulting in a high degree of correlation between solar zenith angle and latitude. For this reason, many studies have avoided examining any μ_0 dependencies in the results. One exception is a study by Stuhlmann et al. (1985), in which bidirectional reflectance functions (normalized by upwelling irradiance) from Earth Radiation Budget (ERB) Nimbus-7 observations and plane parallel calculations were compared (Nimbus-7 is in a noon Sun-synchronous orbit). In their comparison, observed bidirectional reflectance functions can be seen to become increasingly larger than the plane parallel values as μ_0 decreases for $\mu_0 < 0.47$.

It is proposed that the reason for the inconsistency between the plane parallel calculations and the observations is due to the neglect of cloud inhomogeneities (3D effects) in the plane parallel model approach. Results from theoretical studies involving comparisons between Monte Carlo simulations of 3D and plane parallel clouds appear to support this. For example, in a comparison between radiances from broken 3D cubical and plane parallel clouds (Kobayashi, 1993), a steady increase in the ratio of the 3D cloud field radiance to that from the plane parallel cloud is observed at nadir as μ_0 gets smaller, in a manner consistent with the results presented here.

While a more detailed examination of 3D effects is deferred until Chapter 4, certain arguments regarding the possible nature of these 3D effects can be made based on the results presented thus far. In general, 3D effects may be attributed to various combinations of (a) non-linear averaging of sub-pixel inhomogeneity, (b) cloud sides, affecting illuminated and viewed cloud cross-sections as well as allowing loss of radiation, (c) cloud top structure, and (d) internal cloud inhomogeneity. Partial sensitivity to effect (a) is indicated by the difference between the homogeneous and inhomogeneous approximations for sub-pixel cloud fraction (although the complete effect of non-linear averaging is likely to be greater than the inhomogeneous approximation made here). Since both approximations show a similar qualitative dependence on μ_0, non-linear averaging of sub-pixel inhomogeneity is not the most likely explanation. Neither would the effect of internal cloud inhomogeneity be expected to explain the μ_0 dependence, since this would likely be stronger at high solar elevations where the observed μ_0 dependence is weak. Accordingly, the 3D effects that are most likely to explain the difference between the observed and 1D-modeled μ_0 dependence are the effects of cloud sides and cloud top structure (Chapter 4).

Regardless of the cause for the discrepancies, however, these results have obvious implications for remote sensing studies involving the use of plane parallel theory to even small cloud thicknesses at very large solar zenith angles—for example, in high latitude regions and at sunrise and sunset at all latitudes. Simply correcting for curvature effects and the air mass above the cloud is clearly not sufficient to produce self-consistent results. The clouds themselves have to be more one-dimensional than is evident from this study—especially by having flatter tops and weaker side effects. The sort of one-dimensional clouds required for the successful application of the plane parallel model do not appear to be statistically important in this data set, which covered oceanic regions from 30°N to 30°S. As a minimum requirement, application of 1D theory to the remote sensing of cloud optical thickness from measurements at nadir should therefore be restricted to thin clouds and small solar zenith angles.

2.7 Summary

The above results have shown that when observed and plane parallel model reflectances at nadir are compared as a function of solar zenith angle (or μ_0), significant differences are observed. Consequently, when used to infer cloud optical depth from observations, the plane parallel approach results in a systematic increase in cloud optical depth with solar zenith angle. On average, the largest increases occur for $\mu_0 \leq 0.45$ when sub-pixel cloud fraction is taken into account. This dependence on μ_0 is also sensitive to cloud optical depth. For thin clouds (optical depths ≤ 6), this dependence tends to be strong only at oblique sun angles, while for thicker clouds with optical depth greater than ≈ 12 at high sun, this dependence on μ_0 occurs for all solar zenith angles. The cause for these discrepancies is likely associated with 3D effects such as the influence of cloud sides and cloud top structure. These will be examined in more detail in Chapter 4.

The overall (relative) uncertainty in average reflectance due to the μ_0 bias in cloud optical depth was estimated to be less than 10% for $\mu_0 > 0.6$, and as large as 30% at very oblique sun angles. While the uncertainty in the nadir reflectance was generally small when the reflectance was low, it still exceeded 10% for $\mu_0 < 0.45$ for the thinnest 50% of the clouds, and tended to increase substantially for brighter clouds. Because of these differences, application of 1D theory to the remote sensing of cloud optical thickness from measurements at nadir should therefore be restricted to thin clouds and small solar zenith angles.

Chapter 3

Plane Parallel vs Observed Reflectance: View and Relative Azimuth Angle Dependence

3.1 Introduction

The previous chapter has shown that cloud optical depths inferred from 1D theory are systematically biased due to a significant difference in the nadir reflectance dependence on μ_0 between observations and plane parallel calculations. A natural follow-up question, then, is how well does the plane parallel model represent the view and relative azimuth angle dependence of the observed reflectance field? In this chapter, this question is addressed by directly comparing plane parallel model and observed reflectances as a function of view and relative azimuth angle. Since much of the methodology relevant to this chapter has already been described in detail in Sections 2.2 and 2.3, only issues not already covered pertaining to the extension of the analysis to all view angles will be provided here.

3.2 Methodology

3.2.1 Plane Parallel Calculations

As in Chapter 2, plane parallel broadband reflectances are represented by the sum of the clear and cloudy contributions from each pixel (Eq. 2.2). Cloud reflectances (R^{CLD}) are inferred from look-up tables of plane parallel model reflectance at 19 view and solar zenith angles between 0° and 89°, and 19 azimuth angles between 0° and 180° (Section 2.3.1).

Clear sky reflectances (R^{CLR}) are obtained from look-up tables derived directly from observations. To construct these look-up tables, the procedure described in Section 2.3.2 was extended. First, a clear sky longwave threshold value at nadir was inferred from pixels identified as clear by the ERBE Maximum Likelihood Estimation Technique (Wielicki and Green, 1989). These accounted for the warmest 17% of all nadir observations. At off-nadir view angles, longwave thresholds were then defined by assuming that the same relative frequency of clear pixels obtained at nadir occurs there. Thus, since 17% of all nadir pixels were identified as clear, longwave thresholds at off-nadir view angles were inferred so as to also isolate the warmest 17% of pixels there. Then, by analyzing the shortwave reflectance frequency distributions of pixels with longwave radiances larger than the longwave thresholds, look-up table values of R^{CLR} were defined from the peak reflectances in the shortwave reflectance frequency distributions. In this manner, R^{CLR} was derived at 10 values of μ_o between 0 and 1, 7 values of μ between 0.3 and 1, and 18 values of ϕ between 0° and 180°.

Since the ERBS field-of-view (FOV) actually increases in size from approximately 1,500 km^2 at nadir to 27,300 km^2 at a view angle of 70°, the above assumption that the relative frequency of clear pixels is the same at all view angles is not strictly correct. As the FOV increases in size, the fraction of clear pixels should actually decrease since larger pixels have a greater likelihood of at least some cloud contamination than smaller pixels. Ye and Coakley (1994b) estimated the frequency of clear pixels to decrease from approximately 17% at nadir to 8% at view angles between 63° and 75°. To examine the effect of this, R^{CLR} values inferred from reflectance frequency distributions of the warmest 17% of all pixels falling in the most oblique μ bin were compared with those obtained when only the warmest 8% of all pixels were considered. Overall, while the frequency distributions showed some differences between these two cases, the peak reflectances (and therefore R^{CLR} values) did not change very much—absolute differences at all μ_o and ϕ were generally less than 1%.

3.2.2 Analysis Approach

The basic approach in comparing the view angle dependence in reflectance between the plane parallel model and the observations involves two steps. First, the plane parallel calculations are normalized on a pixel-by-pixel basis at nadir by inferring cloud fraction (f) and cloud optical depth (τ_p) values which ensure a match between each calculation and nadir pixel observation (Section 2.4.2). Each f and τ_p pair is then used as input to the plane parallel model to generate reflectances in 10 μ_o-bins, 7 μ-bins and 6 ϕ-bins. Once one full year has been processed, the ensemble of plane parallel reflectances is compared directly with the observations. Ideally, it would be desirable to use all μ_o bins in the normalization of the calculations at nadir. However, because cloud optical depths were shown to depend systematically on solar zenith angle (Chapter 2), this would introduce unrealistically large optical depths in the calculations. In order to minimize this effect, normalization of the calculations is restricted to the range of solar zenith angles for which the average cloud optical depth does not depend appreciably on μ_o. Based on Fig. 2.11, this corresponds to μ_o>0.45. To reduce computational times, normalization of the calculations is further restricted to three μ_o bins: μ_o=0.5-0.6, μ_o=0.7-0.8 and μ_o=0.9-1.0. While the optical depth bias still exists in these μ_o bins for thick clouds, the effect is much less pronounced than at smaller μ_o.

3.2.3 Error Analysis

Since one full year of observations are considered, the μ bins are well sampled in general. Uncertainties in the mean observed shortwave reflectance are generally less than 0.5% (absolute reflectance) at all angles except close to the forward scattering peak (ϕ=0°), where the number of samples is much smaller.

One of the largest uncertainties in the plane parallel calculations involves the specification of cloud fraction-cloud optical depth pairs used in the normalization of the plane parallel calculations at nadir. While different combinations of cloud fraction-cloud optical depth pairs may yield the same reflectance at nadir, the corresponding angular reflectance dependence can vary substantially. In order to account for these uncertainties and to ensure that any differences between the observations and plane parallel calculations are not simply due to uncertainties in the normalization procedure, both the inhomogeneous and homogeneous pixel approximations are considered (Section 2.3). Also, as in Chapter 2, three different approximations for the contribution from the clear sky above the cloud top are employed (Z_t=3 km, 6 km, and the case where clear sky effects are neglected). Since the model calculations only account for scattering from water clouds, while the observations also include contributions from ice clouds, additional comparisons are also carried out for the case where thick ice clouds are included/excluded from the analysis.

The fact that the ERBS field-of-view (FOV) size actually increases with view angle introduces another uncertainty since this effect is not accounted for in the plane parallel calculations. Rather, off-nadir reflectances are calculated at the same resolution as at nadir (where the calculations are normalized). In order to examine what effect this has, a separate analysis is performed in Section 3.3.4 on data that has been degraded to a constant resolution equal to that at μ=0.35 (the midpoint of the most oblique μ bin) in all μ bins.

Other uncertainties associated with the plane parallel model calculations include variations in cloud microphysics, uncertainties caused by the use of a coarse spectral resolution in the broadband reflectances ($\leq$ 3%), and uncertainties in ocean surface reflectance contributions from below the cloud layer. These latter uncertainties, however, were found to have much less of an influence on the μ dependence in the calculations. The largest of these was found to be due to cloud microphysics which was estimated to cause relative uncertainties in shortwave reflectance of less than 5% at all μ, based on comparisons between the C.1 cloud model (effective radius of 6 μm) and a cloud model having an effective radius of 10 μm.

3.3 Results

3.3.1 View Angle Dependence

In order to examine the sensitivity in the average observed shortwave reflectance to the inclusion/exclusion of thick ice clouds, clear scenes, and to the effects of pixel area expansion, Fig. 3.1 (a) and (b) show observed shortwave reflectance averages as a function of μ for μ_o=0.1-0.2 and μ_o=0.7-0.8, respectively, both in the back (ϕ=120°-180°) and forward (ϕ=30°-60°) scattering directions. The ϕ=0°-30° interval was excluded from the analysis in order to avoid the effects of sun glint and reduced data sampling in that interval. In Fig. 3.1, mean reflectances from all observations throughout the year ("All Obs") are compared with those obtained when clear sky pixels are excluded ("No Clr"), when both clear sky pixels and pixels consisting of thick ice clouds are excluded ("No Clr/Cirr"), and when the data are degraded (based on Section 3.3.4) to a constant spatial resolution at all μ equal to that at μ=0.35 for the case where clear sky pixel are excluded ("Degr (No Clr")). As shown, when clear scenes are excluded from the averaging, the average reflectance increases by of roughly 10-15% (relative increase), but little change is observed in the relative μ dependence. If scenes consisting of thick ice clouds are also removed from the analysis, this reduces the average shortwave reflectances to values comparable to the "All Obs" case. Thus, exclusion of both thick ice clouds and clear scenes appears to have a canceling effect. When the FOV size at all μ is constant ("Degr (No Clr")), the average shortwave reflectance decreases by $\leq$ 5% (relative difference) at nadir relative to the "No Clr" case at full resolution. Thus, while the average observed shortwave reflectance shows some sensitivity to the way in which the observations are averaged, this sensitivity appears to be weak and does not have much of an effect on the μ dependence in the shortwave reflectance.

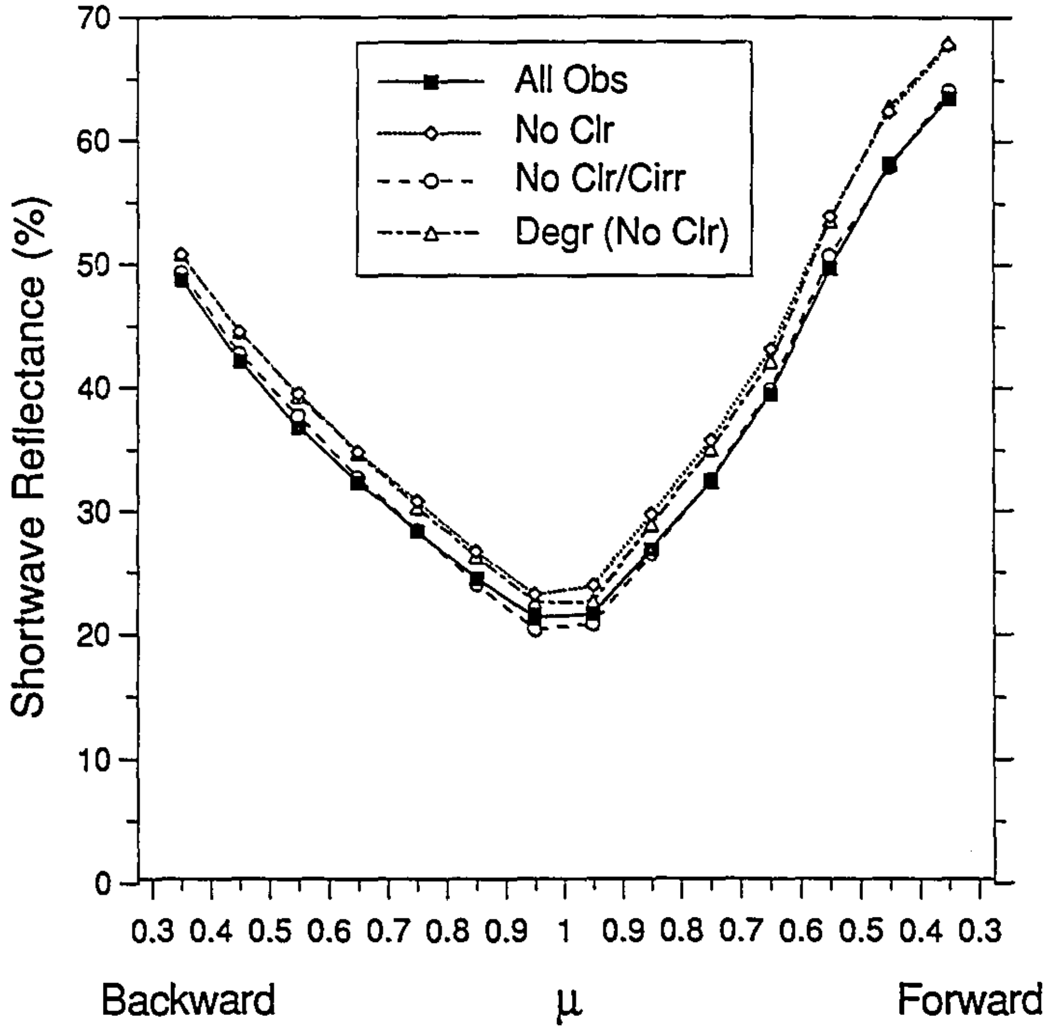
All Obs
No Clr
No Clr/Cirr
Degr (No Clr)
Shortwave Reflectance (%)
0
10
20
30
40
50
60
70
0.3 0.4 0.5 0.6 0.7 0.8 0.9 1 0.9 0.8 0.7 0.6 0.5 0.4 0.3
Backward
μ
Forward

(a)

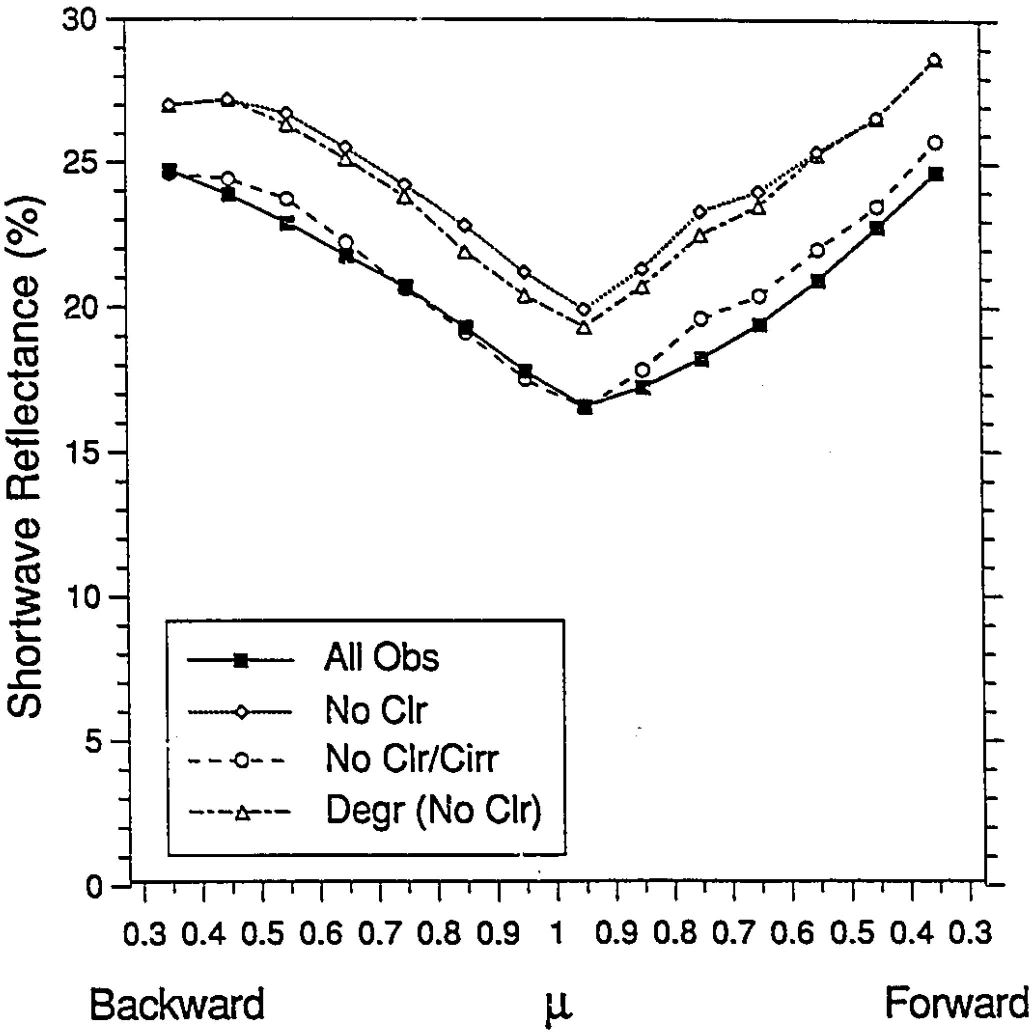

(b)

Figure 3.1 Observed shortwave reflectance averages as a function of μ in the backscattering direction (ϕ=120°-180°) and in the forward scattering direction (ϕ=30°-60°) for (a) μ_0=0.1-0.2; and (b) μ_0=0.7-0.8.

Figs. 3.2 (a) shows the cloud optical depth distributions inferred from the normalization of the plane parallel calculations at μ_o=0.5-0.6, μ_o=0.7-0.8 and μ_o=0.9-1.0. In this figure, results for the inhomogeneous approximation involving three different assumptions for the clear sky contribution above the cloud are shown (i.e. "Z_t=3 km", "Z_t=6 km", "No Atm"), together with a case with Z_t=3 km in which thick ice clouds are excluded from the analysis ("Z_t=3 km (No Cirr)"), and a case involving the homogeneous pixel approximation with Z_t=3 km ("Z_t=3 km (Hom)"). As shown, the largest influence on the cloud optical depth distribution is determined by whether the inhomogeneous or the homogenous pixel approximation is used. Since all pixels are assumed to have a cloud fraction of unity in the homogeneous pixel approximation, the frequency of very thin clouds tends to be much larger for this case. The average cloud optical depth obtained using the homogeneous approximation was 5.4 ("Z_t=3 km (Hom))", compared to 9.5 for the inhomogeneous approximation ("Z_t=3 km"). As the cloud top height increases, attenuation above the cloud decreases, and inferred cloud optical depths decrease—average cloud optical depths for the "Z_t=6 km" case and the "No Atm" case were 7.8 and 6.8, respectively. Removing thick ice clouds in the analysis also appears to have an effect on the cloud optical depth frequency distribution ("Z_t=3 km (No Cirr)"). For this case the average cloud optical depth was reduced to 7.6.

Fig. 3.2 (b) shows cloud fraction frequency distributions obtained when thick ice clouds are included ("Include Cirr") and excluded ("No Cirr") from the analysis. Compared with the cloud optical depth distributions in Fig. 3.2 (a), a much stronger sensitivity to the presence of thick ice clouds is observed in the cloud fraction frequency distributions. As shown, the frequency of overcast pixels almost doubles when the thick ice clouds are included.

Average shortwave reflectances calculated using the cloud fraction-cloud optical depth distributions in Fig. 3.2 are compared directly with the observations (excluding clear

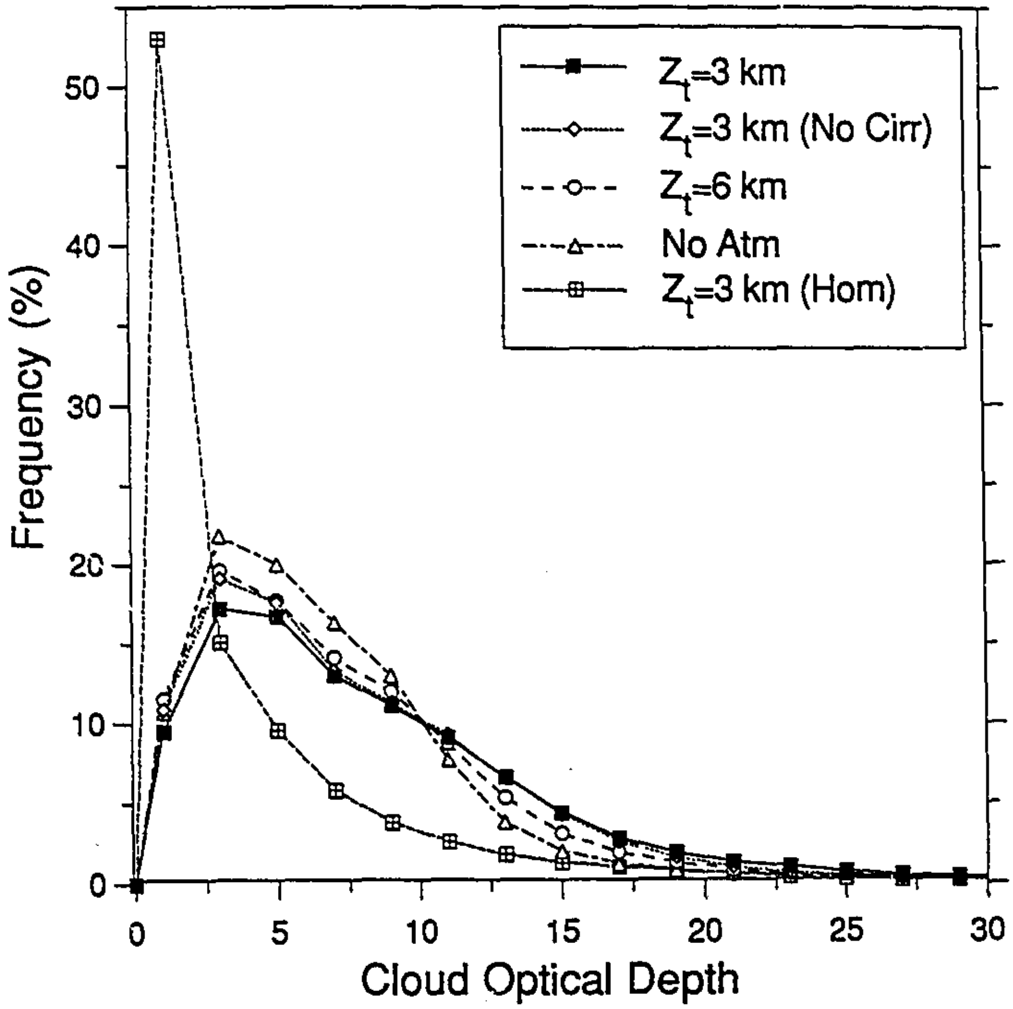

Z_t=3 km
Z_t=3 km (No Cirr)
Z_t=6 km
No Atm
Z_t=3 km (Hom)
Frequency (%)
Cloud Optical Depth
0
10
20
30
40
50
0
5
10
15
20
25
30

(a)

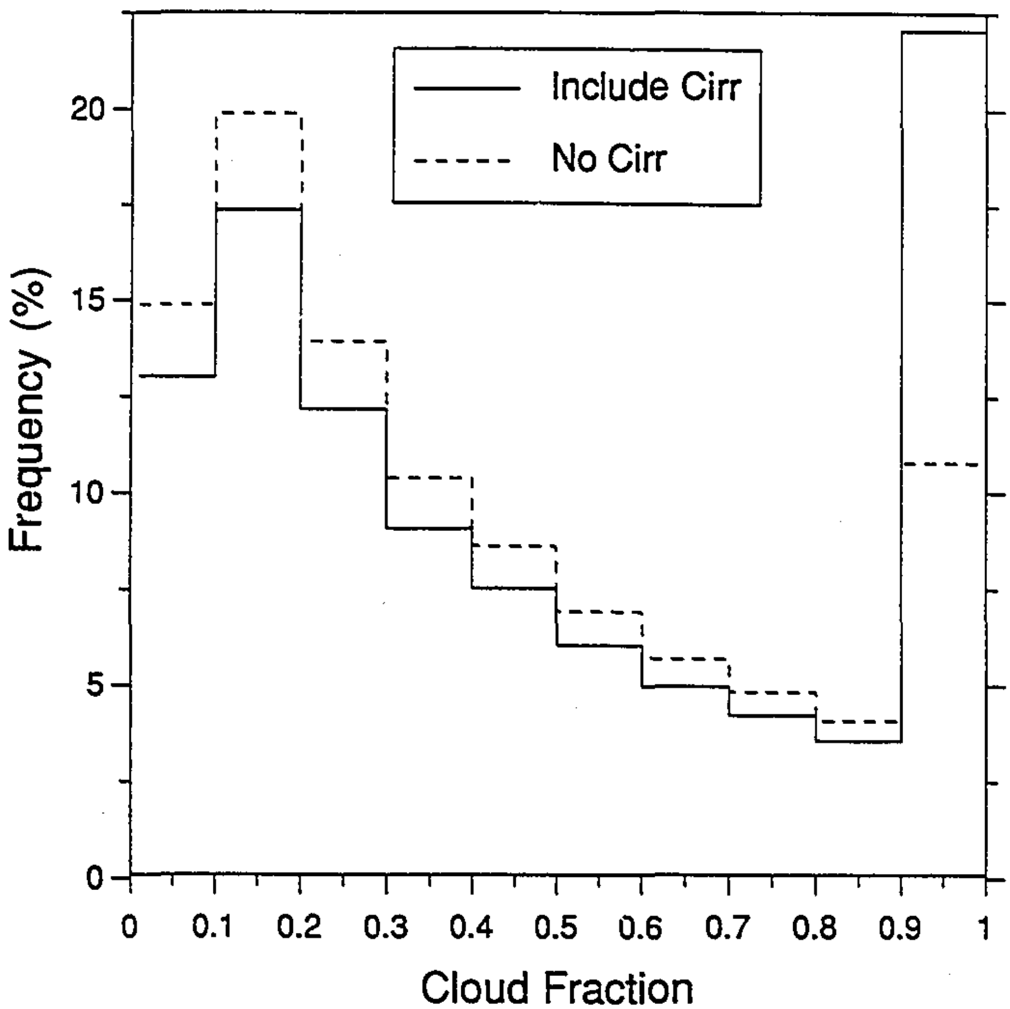

(b)

Figure 3.2 (a) Cloud optical depth and (b) cloud fraction distributions inferred from the normalization of the plane parallel calculations from nadir observations at μ_0=0.5-0.6, μ_0=0.7-0.8 and μ_0=0.9-1.0. "Z_t=3 km" refers to the case where a cloud top height of 3 km is used, "Z_t=6 km" is for a cloud top height of 6 km, "No Atm" is for the case where the clear sky above the cloud is neglected, "Z_t=3 km (Hom)" refers to the homogeneous pixel approximation for a cloud top at 3 km, and "Z_t=3 km (No Cirr)" refers to a cloud with Z_t=3 km in which thick ice clouds are excluded from the analysis.

pixels) in Figs. 3.3 (a) and (b) for μ_o=0.1-0.2 and μ_o=0.7-0.8, respectively. In both cases, the same ϕ intervals as in Fig. 3.1 are used. For μ_o=0.7-0.8, the plane parallel reflectances match the observations quite closely, regardless of what assumptions are made in the calculations. In fact, relative differences are generally less than 5% at all μ. At μ_o=0.1-0.2, while the overall μ dependence in the plane parallel results appears to be qualitatively consistent with the observations in the backscattering direction, the observations are noticeably larger at all μ. In the forward scattering direction, the observations generally fall within the range of plane parallel reflectances for μ<0.65, but show a rather different μ dependence—observed reflectances appear to level off between μ=0.5 and μ=0.3, whereas the calculations show a steady increase.

This figure also clearly illustrates the sensitivity in the average calculated reflectances to the model assumptions. While the sensitivity is small at nadir, it becomes increasingly larger as μ decreases. This is especially true of the "No Atm" and "Z_t=3 km" cases in Fig. 3.3 (a). When no atmosphere above the cloud is included, reflectances at oblique view angles tend to be larger due to the absence of atmospheric attenuation. It is more pronounced at small μ because of the greater path length scattered radiation must travel through before reaching the top of the atmosphere. Consequently, reflectances show a larger increase with decreasing μ when attenuation above the cloud is small. While it is less pronounced in the backscattering direction, it is nonetheless noticeable. In the forward direction, reflectances for the "No Atm" case can actually exceed those for the "Z_t=3 km" case by as much as ≈30% (relative difference) for μ=0.3-0.4.

Figs. 3.4 (a) and (b) show the absolute differences in average reflectance between the observations and calculations in the backscattering direction as a function of μ_o and μ for the "Z_t=3 km" and the "No Atm" cases, respectively. For μ_o>0.45, plane parallel reflectances are generally consistent with the observations at all μ. At smaller μ_o, differences tend to increase with decreasing μ_o, reaching values as high as 10% (absolute

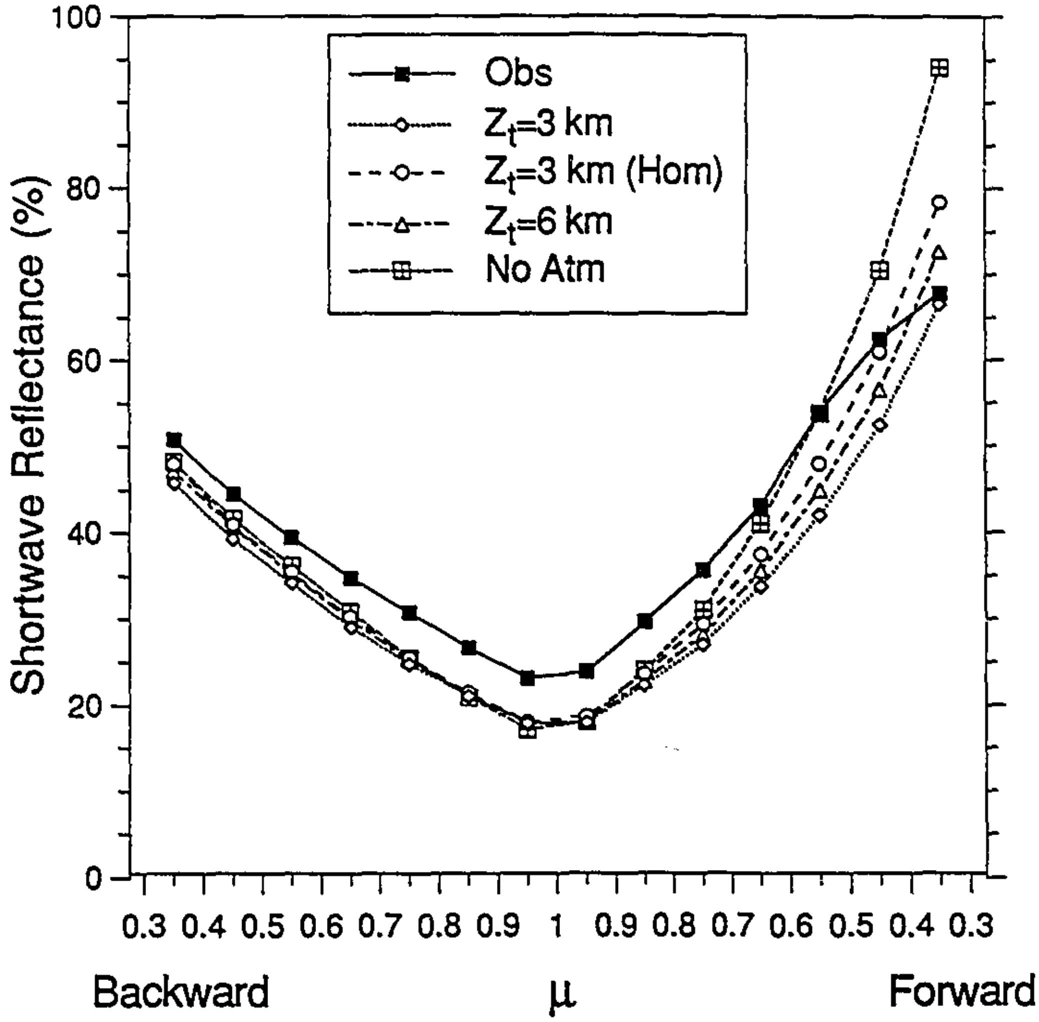
Obs
Zt=3 km
Zt=3 km (Hom)
Zt=6 km
No Atm
Shortwave Reflectance (%)
0
20
40
60
80
100
0.3 0.4 0.5 0.6 0.7 0.8 0.9 1 0.9 0.8 0.7 0.6 0.5 0.4 0.3
Backward
μ
Forward

(a)

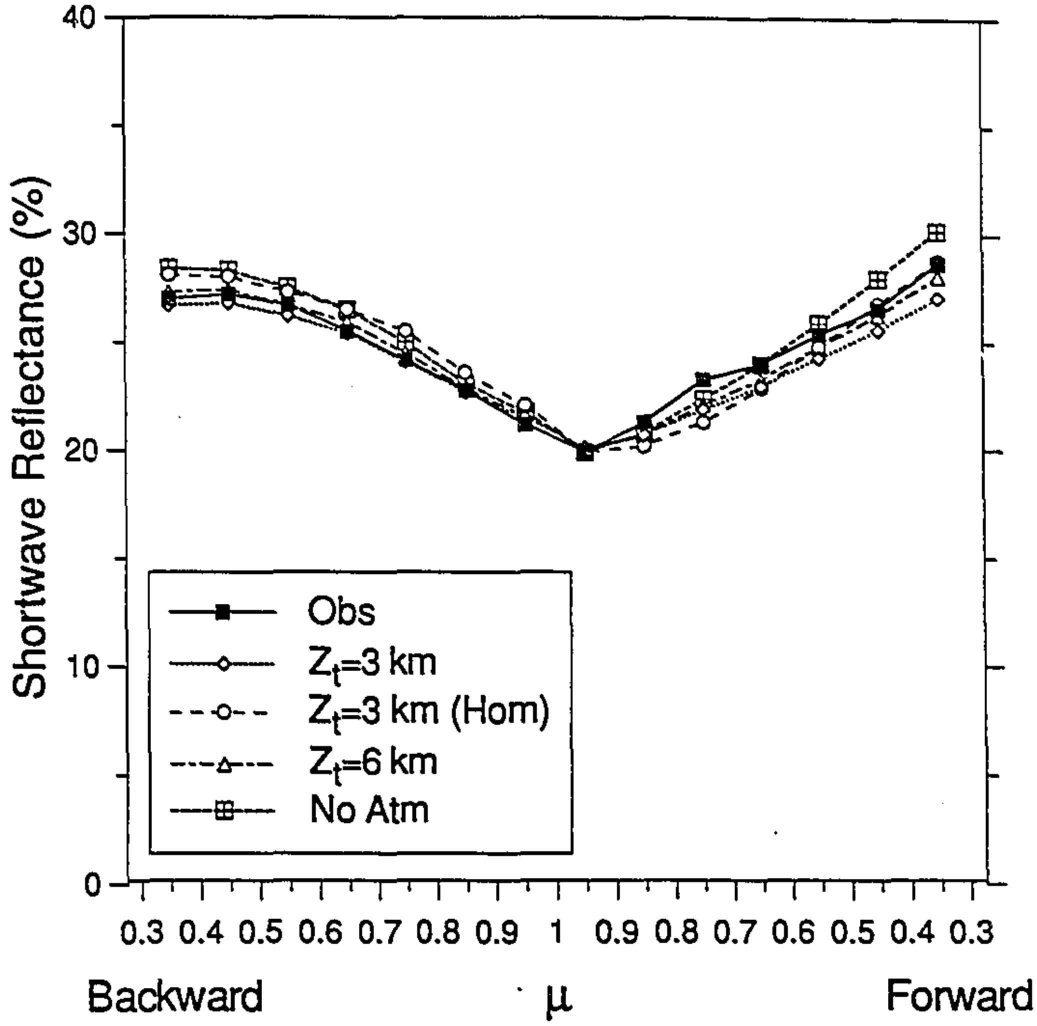

(b)

Figure 3.3 Average shortwave reflectances for the observations and calculations as a function of μ for (a) μ_0=0.1-0.2 and (b) μ_0=0.7-0.8.

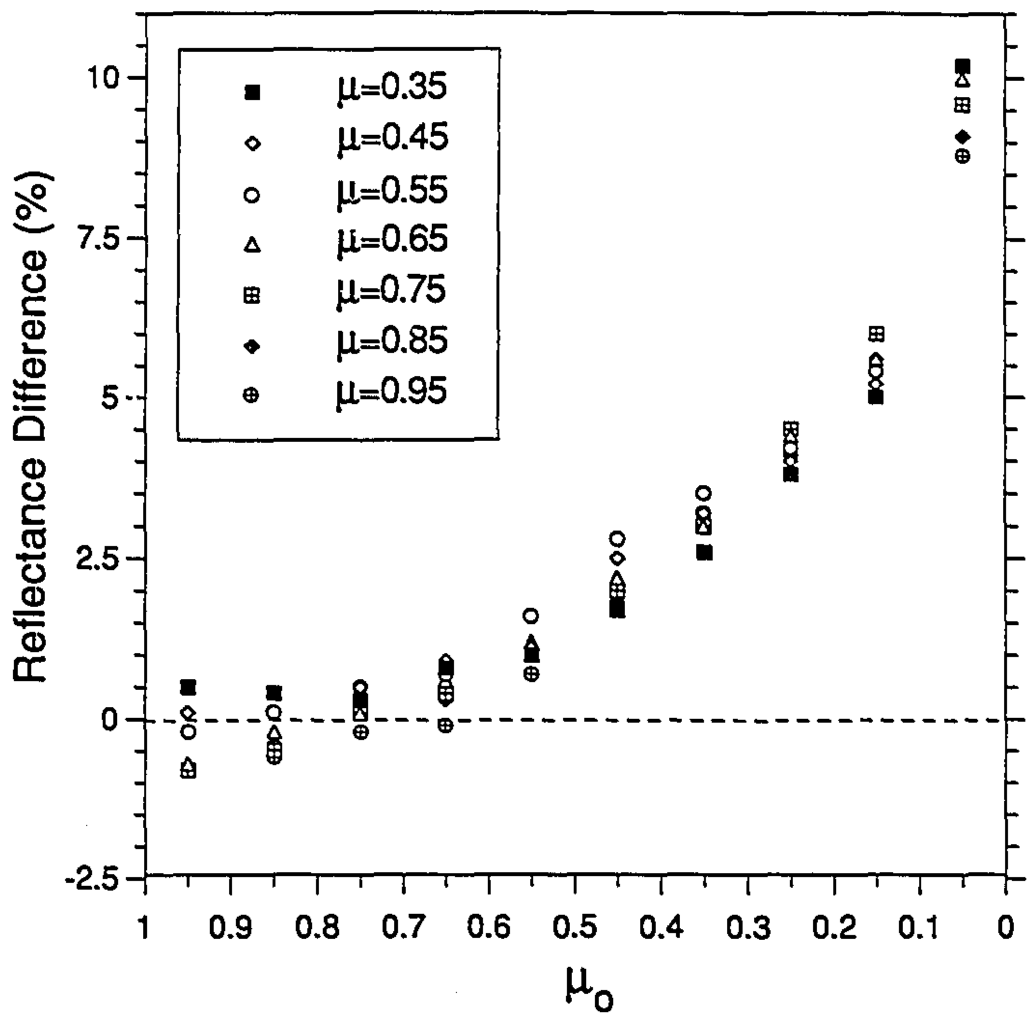

μ=0.35
μ=0.45
μ=0.55
μ=0.65
μ=0.75
μ=0.85
μ=0.95
Reflectance Difference (%)
10
7.5
5
2.5
0
-2.5
1
0.9
0.8
0.7
0.6
0.5
0.4
0.3
0.2
0.1
0
μ_o

(a)

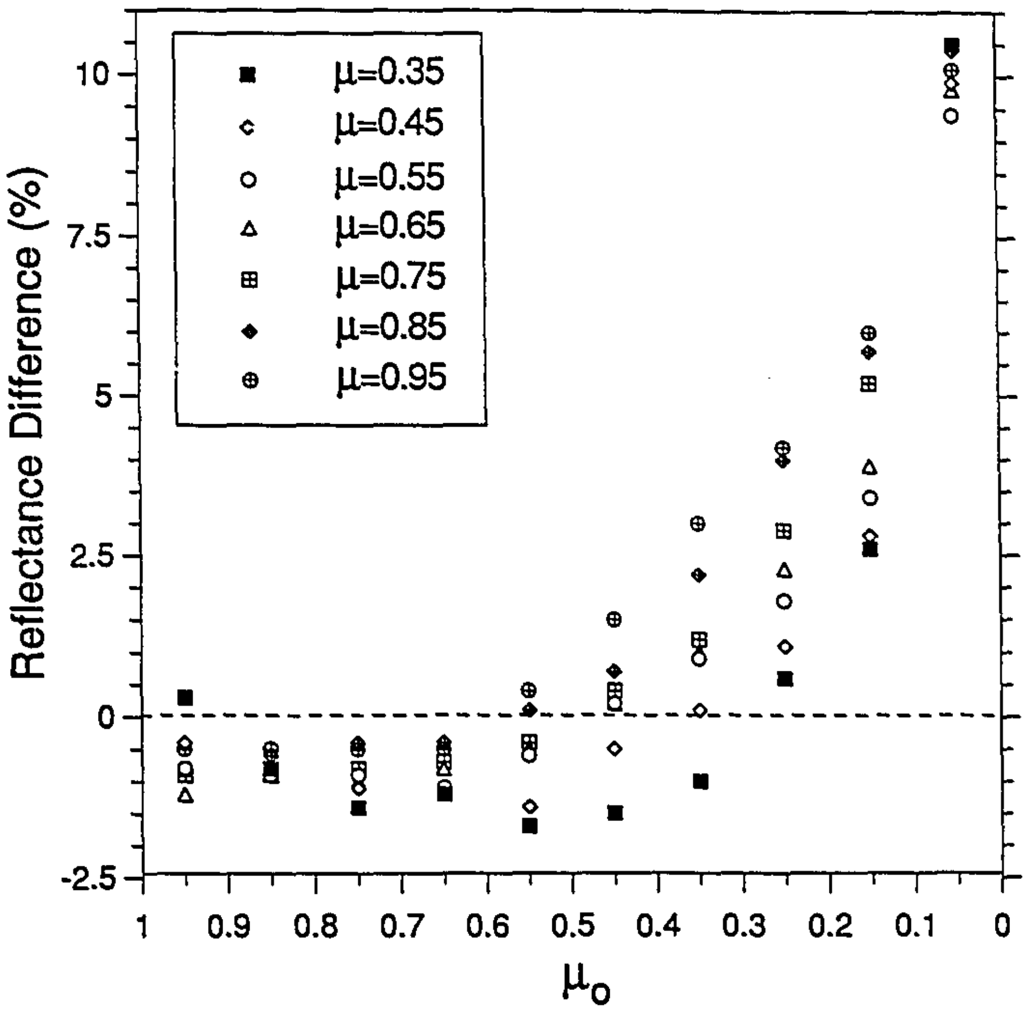

Reflectance Difference (%)
10
7.5
5
2.5
0
-2.5
1
0.9
0.8
0.7
0.6
0.5
0.4
0.3
0.2
0.1
0
μo
μ=0.35
μ=0.45
μ=0.55
μ=0.65
μ=0.75
μ=0.85
μ=0.95

(b)

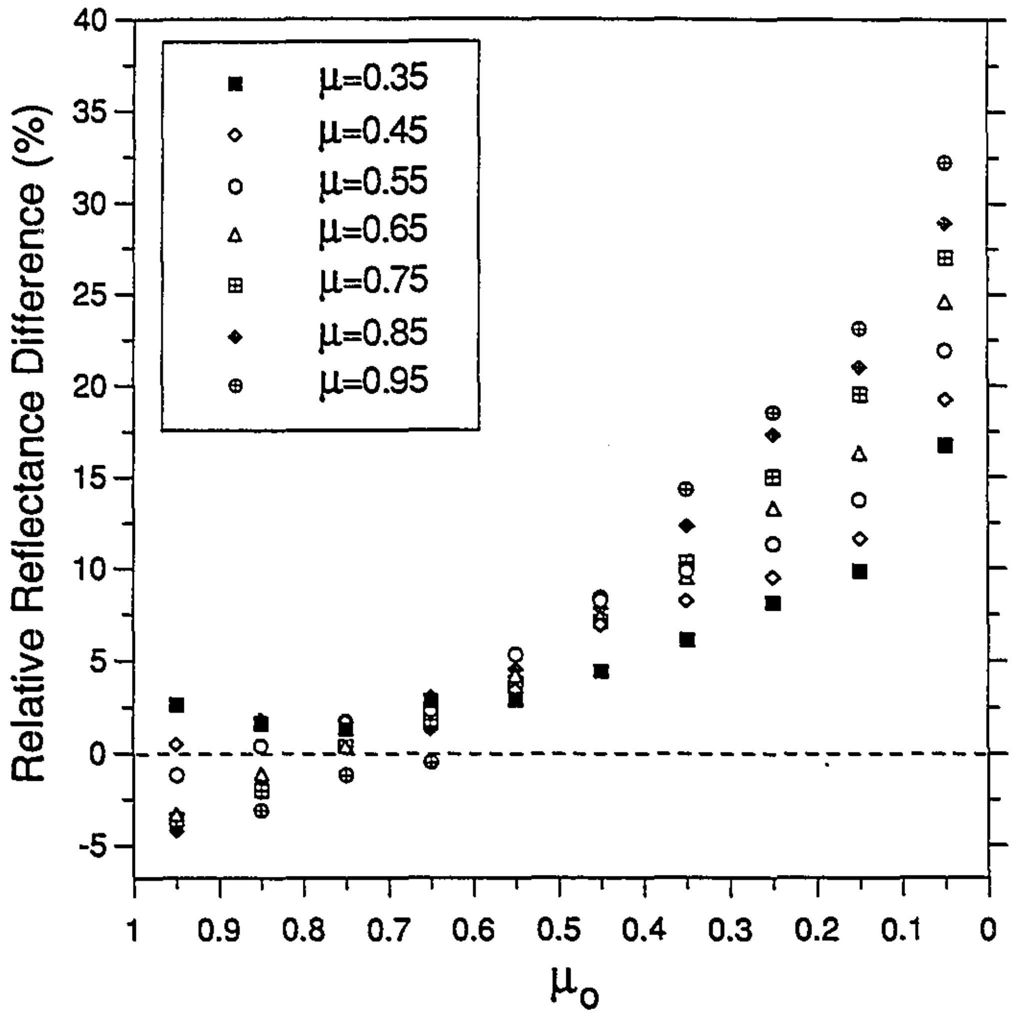

(c)

Figure 3.4 Reflectance differences between the observed and calculated reflectances as a function of μ_0 and μ in the backscattering direction for (a) the "Z_t=3 km" case and (b) the "No Atm" case. Fig. 3.4 (c) shows the relative reflectance differences corresponding to Fig. 3.4 (a).

reflectance) at μ_o=0.0-0.1. Thus, the μ_o reflectance bias observed at nadir in Chapter 2 also appears to affect off-nadir reflectances as well. Interestingly, for the "Z_t=3 km" case (Fig. 3.4 (a)), there does not appear to be any systematic μ dependence in the differences, however. In that case, the increase in reflectance difference with decreasing μ_o is similar at all μ. When the atmosphere above the cloud is neglected (Fig. 3.4 (b)), a much stronger μ dependence is observed—differences tend to be larger at nadir than at oblique view angles. Thus, while inclusion of atmospheric effects may lead to larger reflectance errors at small μ, it nonetheless provides a μ dependence in the average reflectance which is closer to that of the observations (therefore removing any μ-dependent bias in the difference).

The absence of a strong μ dependence in the absolute differences between the average observed and plane parallel reflectances in the backscattering direction is surprising. Minnis (1989) showed that when cloud amounts were examined at different view angles using collocated Geostationary Operational Environmental Satellite (GOES) West and East radiances, the cloud amounts tended to increase with view angle. While the low spatial resolution of the ERBS scanner and the fact that the measurements are broadband may play a role, it is unlikely that these would change this basic result. In another study, Coakley (1991) used high resolution (1 km) monochromatic measurements from the Advanced Very High Resolution Radiometer (AVHRR) to compare the anisotropy of 0.63 μm radiation reflected by uniform and broken stratocumulus cloud layers off the coast of California during the three week period of the First International Satellite Cloud Climatology Project Regional Experiment (FIRE) Intensive Field Observations (IFO). For the range of μ_o considered (μ_o=0.4-0.65 and μ_o=0.7-0.9), differences in reflectance between uniform and broken cloud layers showed no change with μ. Unfortunately, they did not perform any comparisons at smaller μ_o. Rossow (1989) found similar results. In that study, the ISCCP radiative model (which represents clouds as single, homogeneous layers over scales of 4-16 km) was used to infer cloud optical depths from one month of collocated Meteosat-2 and GOES-5 East scenes viewed by each satellite at different μ. Differences in cloud optical depth retrievals as a function of the difference in μ for the two satellites were shown to be small (≤ 5 for most of the samples), suggesting that the angle dependence in radiance is reasonably well represented by the plane parallel model. Unfortunately, it was not mentioned what solar zenith angles were considered in that study, as the results were not stratified by μ_o.

Fig. 3.4 (c) shows the relative reflectance differences corresponding to the results in Fig. 3.4 (a). Because the average reflectances increase with decreasing μ, while absolute differences show less variability, relative reflectance differences inevitably increase with μ. On average, relative errors in the backscattering direction are generally $\leq 20\%$ for $\mu \leq 0.5$, and increase with μ.

Figs. 3.5 and 3.6 show the observed and calculated ("Z_t=3 km") reflectance frequency distributions corresponding to the mean reflectances in Figs. 3.3 (a) and (b), respectively. At μ_o=0.1-0.2 (Fig. 3.5 (a) through (d)), observed and calculated reflectance frequency distributions look quite different at nadir. While the peak reflectance occurs at roughly the same point, the observed reflectance distributions are much broader in appearance, and show a much smaller frequency close to the peak reflectance than do the plane parallel results. In contrast, the shape of the observed and calculated reflectance distributions look remarkably similar at small μ, both in the back and forward scattering directions. Despite this similarity, however, the peak reflectances are not the same. For example, in the backscattering direction, the peak in the observed reflectance distribution at μ=0.3-0.4 (Fig. 3.5 (a)) occurs at $\approx$47%, whereas the corresponding calculated reflectance peak in Fig. 3.5 (b) occurs at $\approx$42%. Thus, while the differences between observed and calculated average reflectances show little sensitivity to μ for the "Z_t=3 km" case, a stronger μ dependence is apparent in the differences between the reflectance frequency distributions.

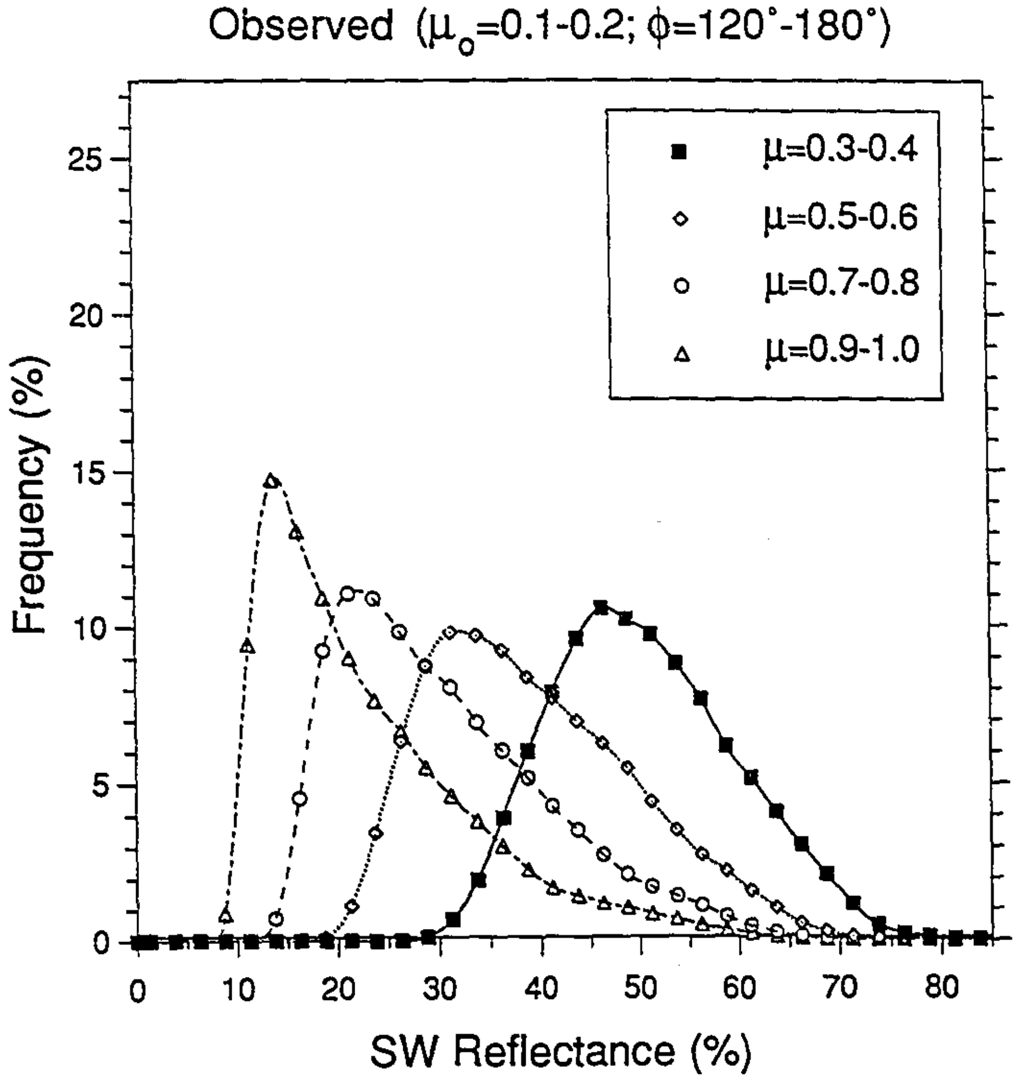

Observed (μ_o=0.1-0.2; ϕ=120°-180°)
μ=0.3-0.4
μ=0.5-0.6
μ=0.7-0.8
μ=0.9-1.0
Frequency (%)
SW Reflectance (%)
0
5
10
15
20
25
0
10
20
30
40
50
60
70
80

(a)

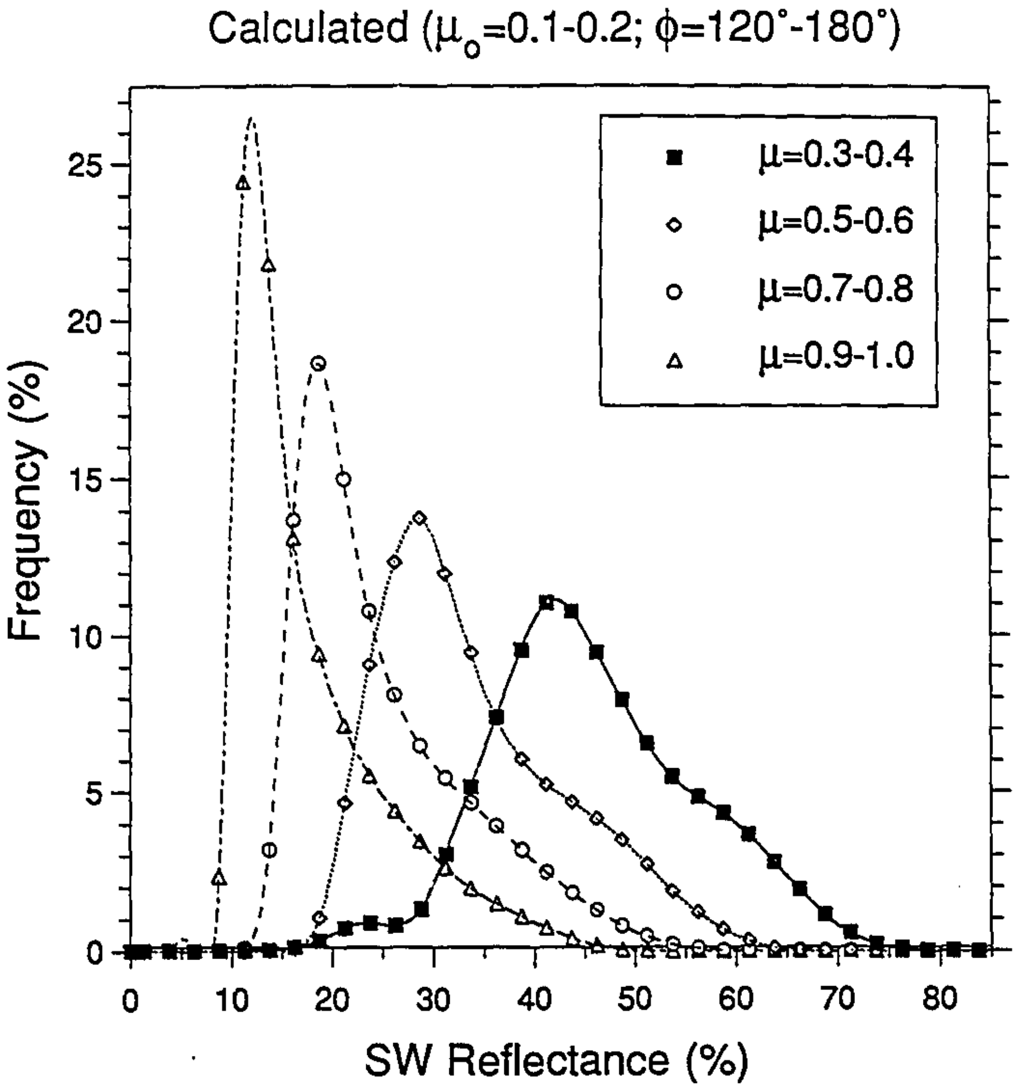

Calculated (μ_o=0.1-0.2; ϕ=120°-180°)
μ=0.3-0.4
μ=0.5-0.6
μ=0.7-0.8
μ=0.9-1.0
Frequency (%)
SW Reflectance (%)
0
5
10
15
20
25
0
10
20
30
40
50
60
70
80

(b)

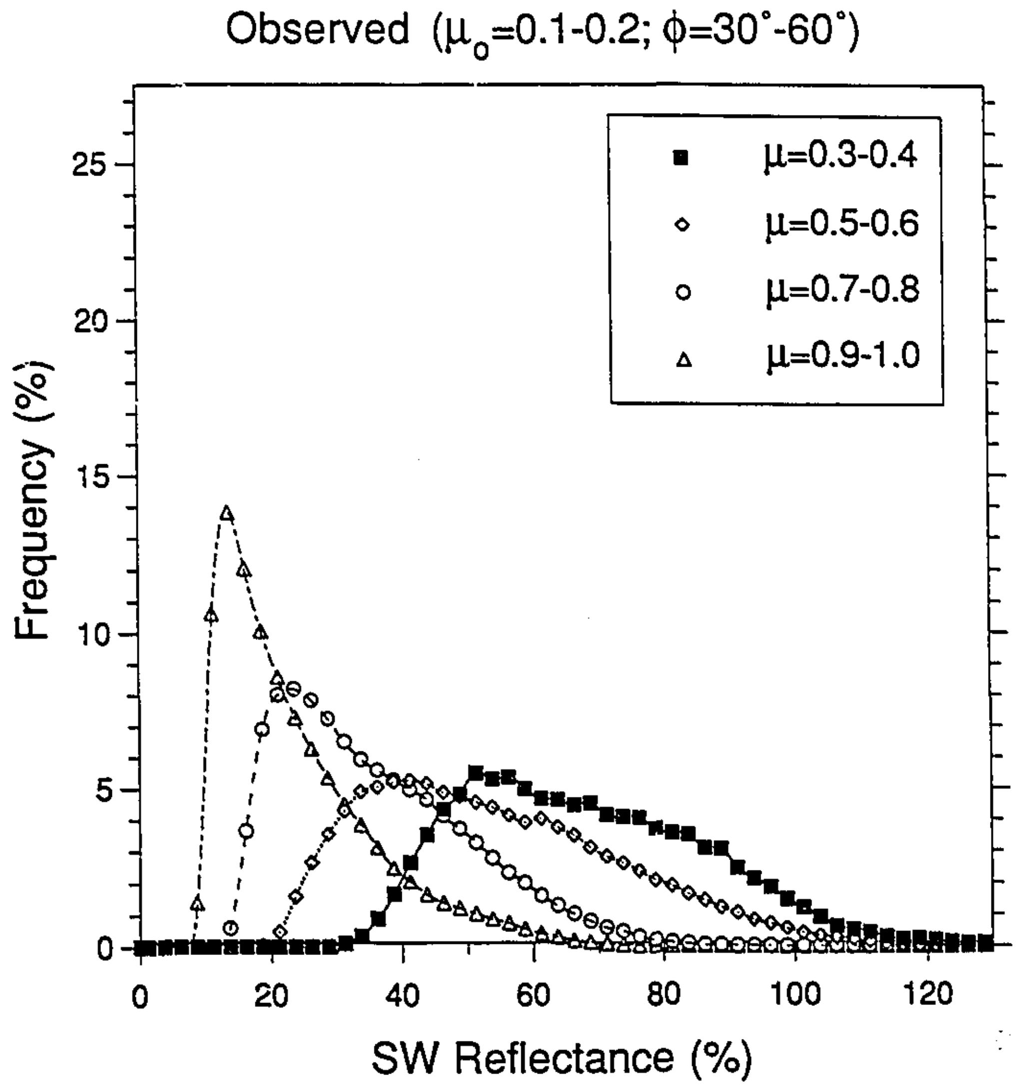

Observed (μ_o=0.1-0.2; ϕ=30°-60°)
μ=0.3-0.4
μ=0.5-0.6
μ=0.7-0.8
μ=0.9-1.0
Frequency (%)
0
5
10
15
20
25
0
20
40
60
80
100
120
SW Reflectance (%)

(c)

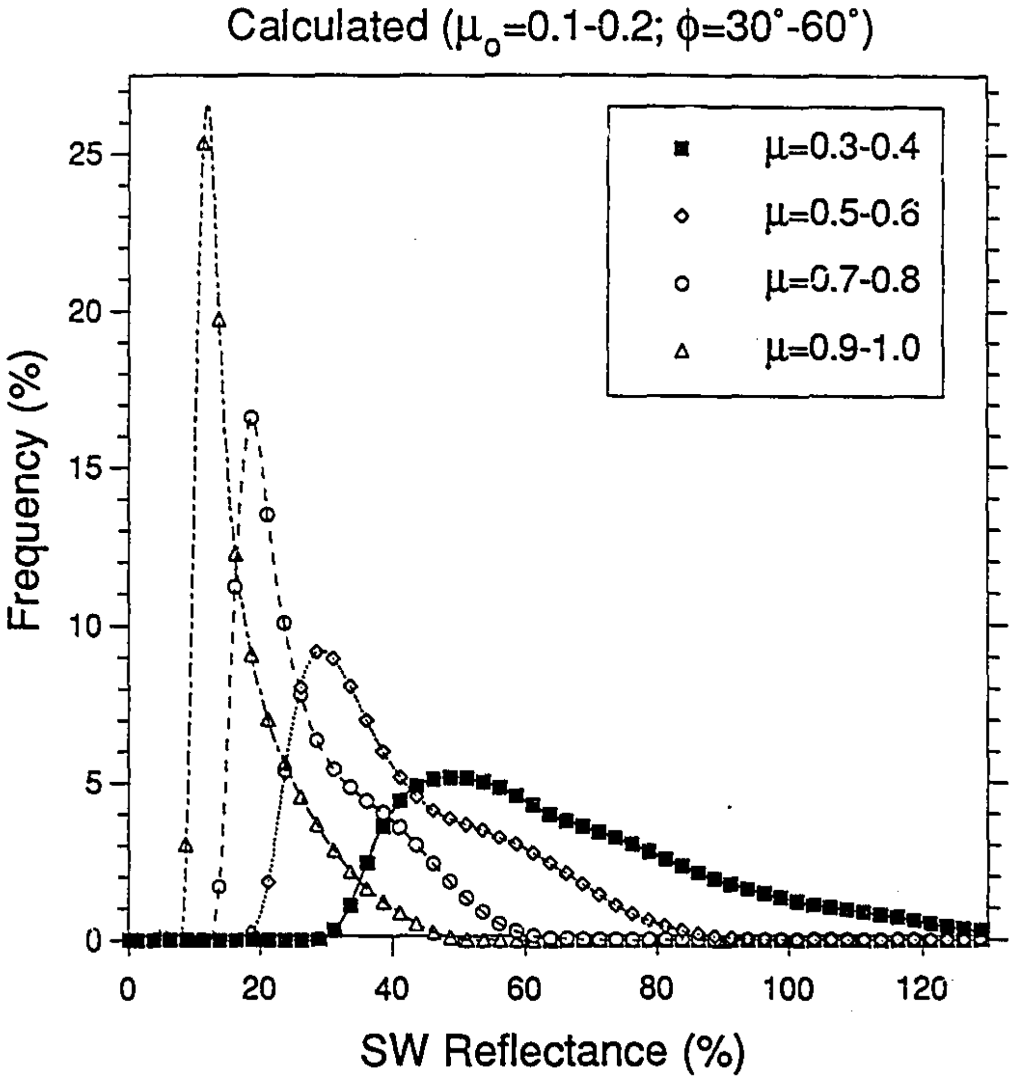

(d)

Figure 3.5 Observed and calculated reflectance frequency distributions as a function of μ for μ_o=0.1-0.2 in the backscattering direction (Figs. 3.5 (a) and (b)) and in the forward scattering direction (Figs. 3.5 (c) and (d)).

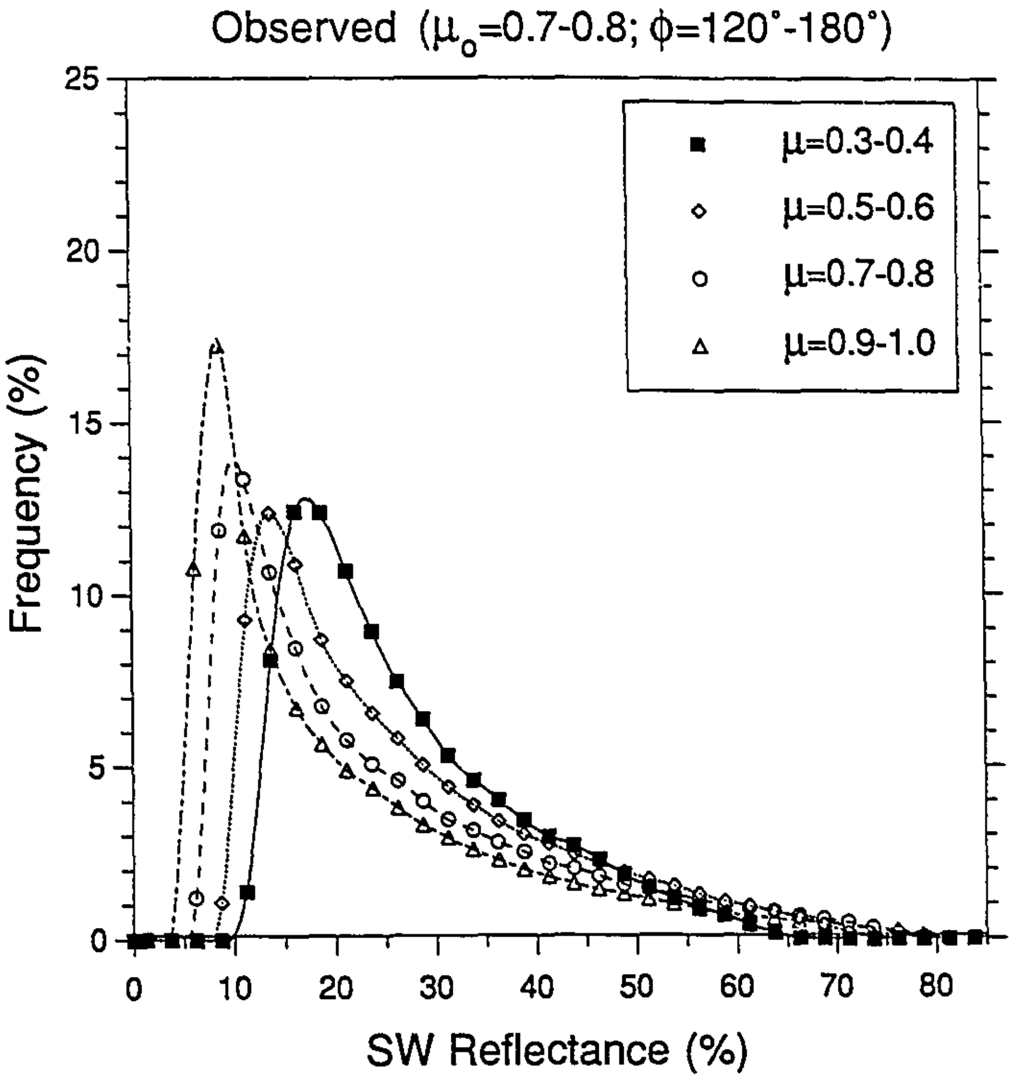

Observed (μ_o=0.7-0.8; ϕ=120°-180°)
Frequency (%)
SW Reflectance (%)
μ=0.3-0.4
μ=0.5-0.6
μ=0.7-0.8
μ=0.9-1.0
0
5
10
15
20
25
0
10
20
30
40
50
60
70
80

(a)

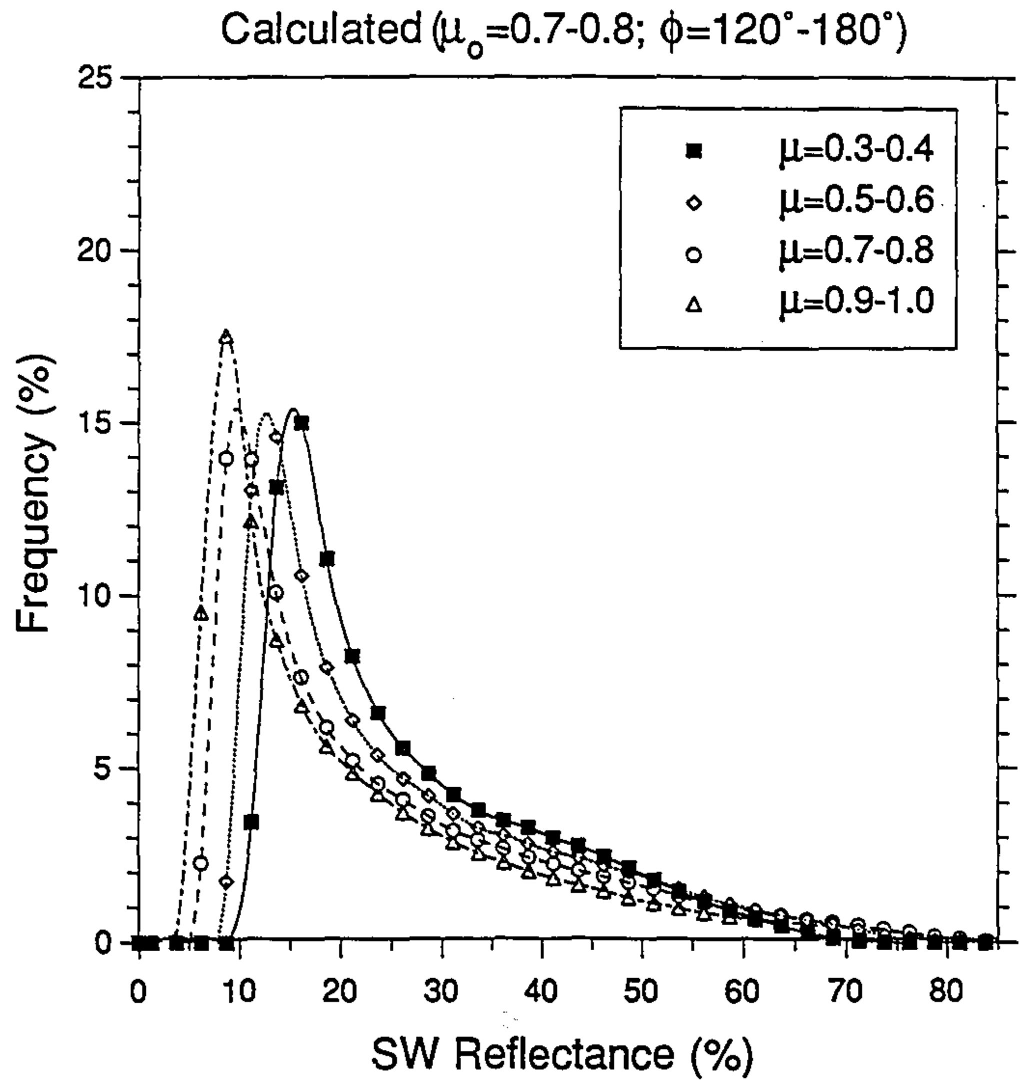

(b)

Figure 3.6 Observed and (b) calculated reflectance frequency distributions as a function of μ for μ_o=0.7-0.8.

In contrast, at μ_0=0.7-0.8 (Fig. 3.6 (a) and (b)), the observed and plane parallel reflectance frequency distributions are quite consistent at all μ.

3.3.2 Dependence On Cloud Brightness

In order to examine how the observed and calculated reflectances depend on cloud brightness (or equivalently cloud thickness), average shortwave reflectance values were calculated for different reflectance classes of occurrence derived from the observed and calculated reflectance frequency distributions. Fig. 3.7 shows observed and calculated reflectance averages (for the "Z_t=3 km" case) for reflectances lying in the 0-25% and 75-100% percentile intervals for μ_0=0.1-0.2. For the darkest clouds (0-25% percentile interval), the plane parallel reflectances are in good agreement with the observations (relative reflectance differences $\leq$ 15%). For the 75-100% percentile interval, reflectance differences are large at nadir (as in Chapter 2), but decrease with decreasing μ in the backscattering direction. In the forward direction, differences are larger, and there is a tendency for reflectances to level off at the most oblique view angles.

To examine these results more closely, Figs. 3.8 (a) through (d) show differences between observed and plane parallel reflectances for various percentile intervals under four different conditions. In Fig. 3.8 (a), the inhomogeneous pixel approximation is assumed with Z_t=3 km, while Fig. 3.8 (b) uses the same approximation but excludes scenes consisting of thick ice clouds. Fig. 3.8 (c) includes thick ice clouds but uses the homogeneous pixel approximation with Z_t=3 km, and Fig. 3.8 (d) assumes Z_t=6 km in the inhomogeneous pixel approximation. In the backscattering direction, all cases show the reflectance difference to be least sensitive to pixel brightness at oblique view angles (relative difference $\leq$ 15%), and most sensitive at nadir. Consequently, reflectance differences increase slightly with decreasing μ for the thinnest (darkest) 25% of the cases, show a smaller variability for the intermediate classes (e.g. 25-50% and 50-75%), and decrease for the 75-100% class. The lack of a strong dependence on pixel brightness at

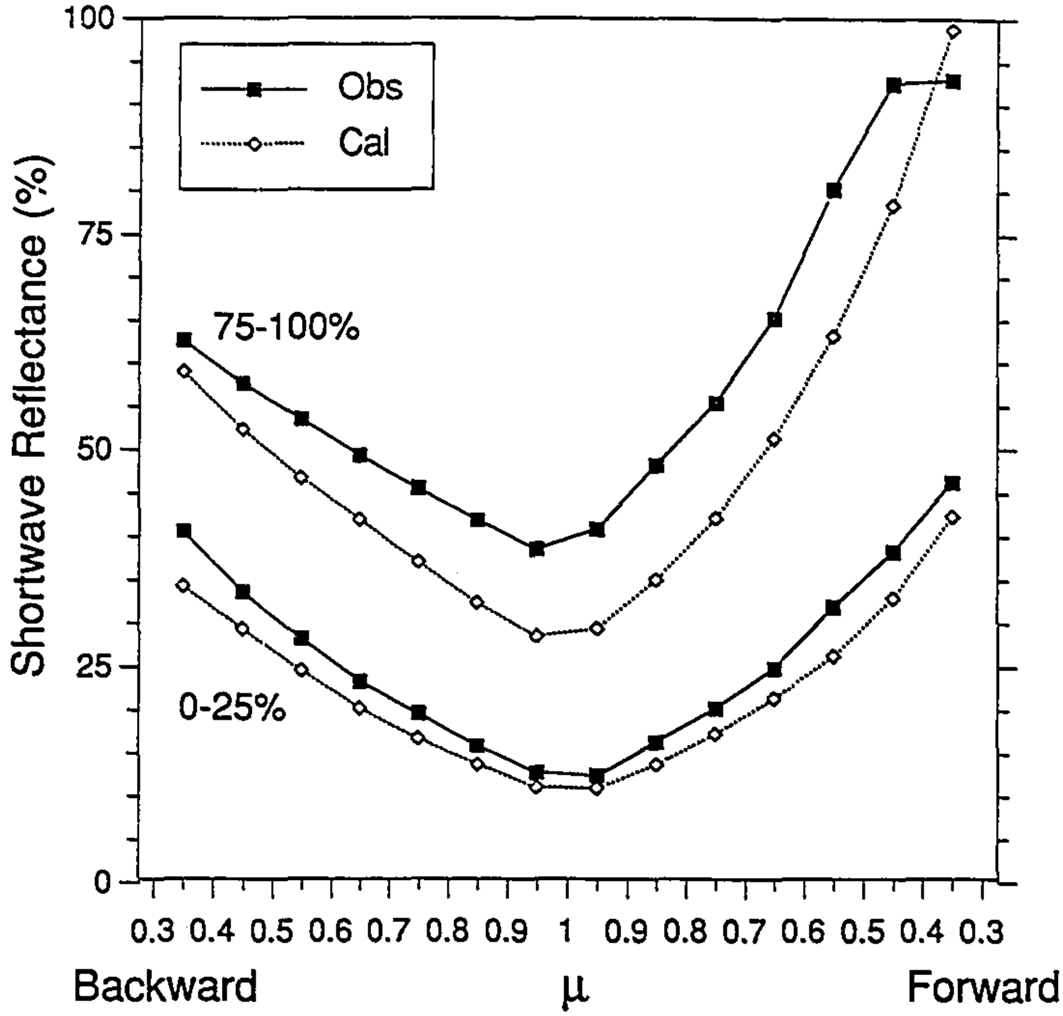

Figure 3.7 Observed and calculated reflectance averages for reflectances lying between the 0-25% and 75-100% percentile intervals for μ_o=0.1-0.2.

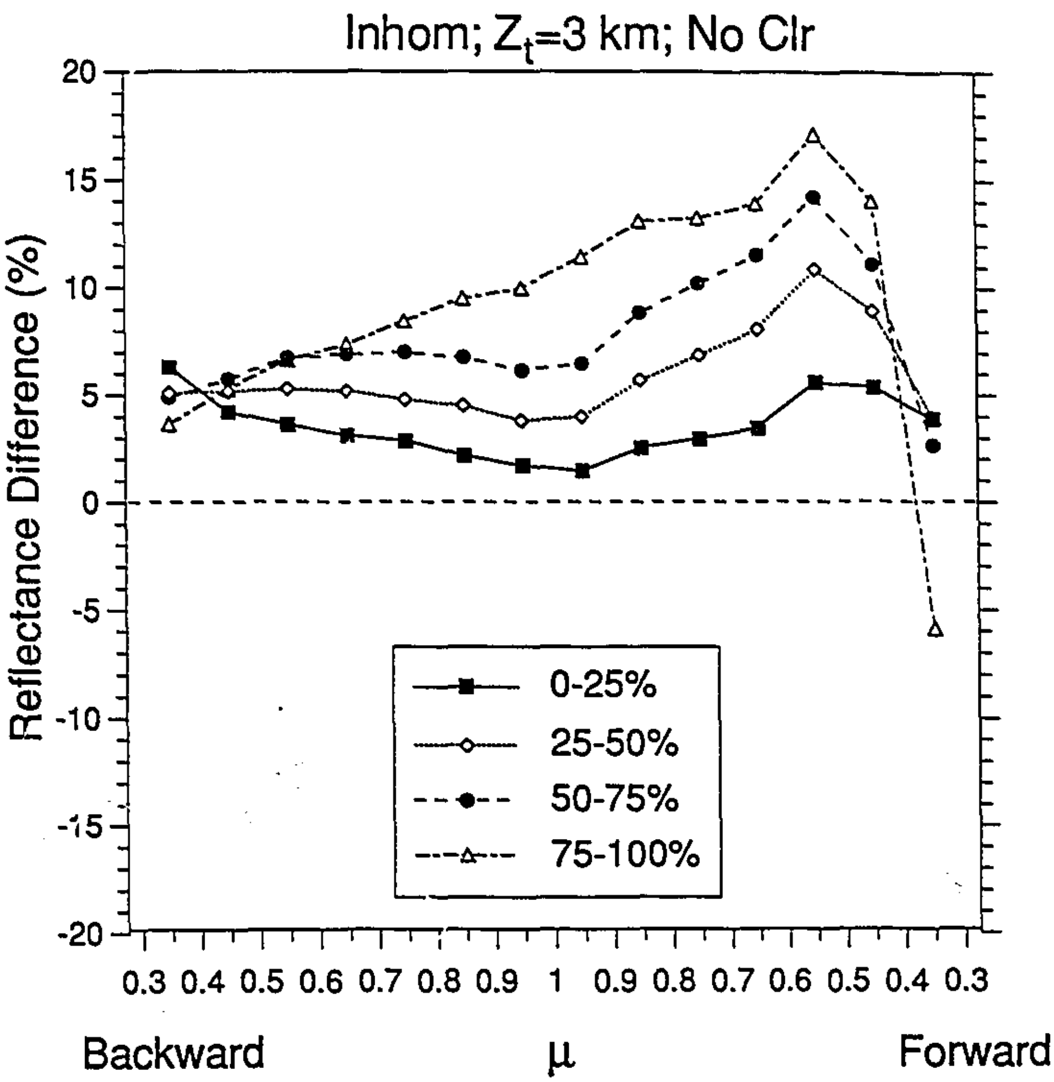

Inhom; Z_t=3 km; No Clr
Reflectance Difference (%)
20
15
10
5
0
-5
-10
-15
-20
0-25%
25-50%
50-75%
75-100%
0.3 0.4 0.5 0.6 0.7 0.8 0.9 1 0.9 0.8 0.7 0.6 0.5 0.4 0.3
Backward
μ
Forward

(a)

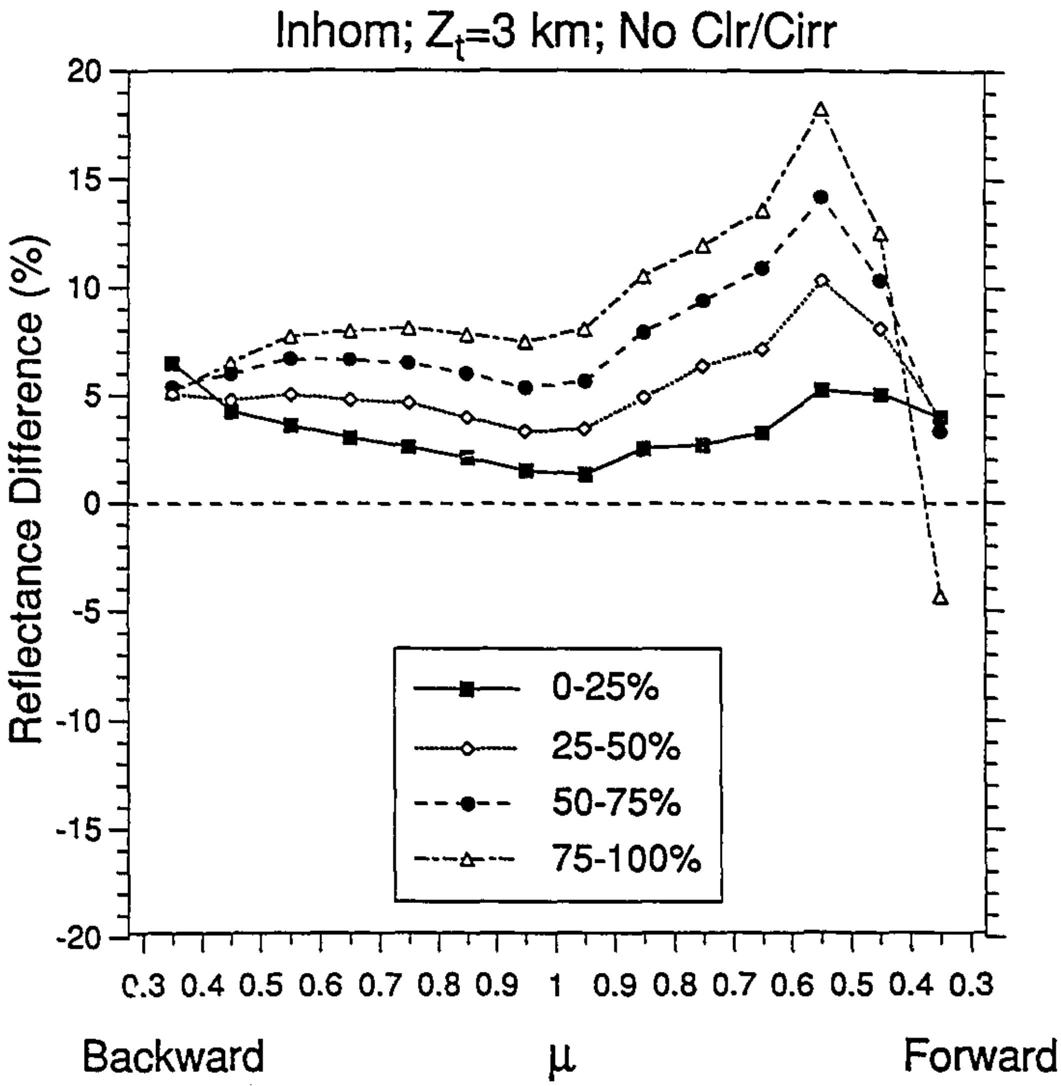
Inhom; Z_t=3 km; No Clr/Cirr
Reflectance Difference (%)
20
15
10
5
0
-5
-10
-15
-20
0-25%
25-50%
50-75%
75-100%
0.3 0.4 0.5 0.6 0.7 0.8 0.9 1 0.9 0.8 0.7 0.6 0.5 0.4 0.3
Backward
μ
Forward

(b)

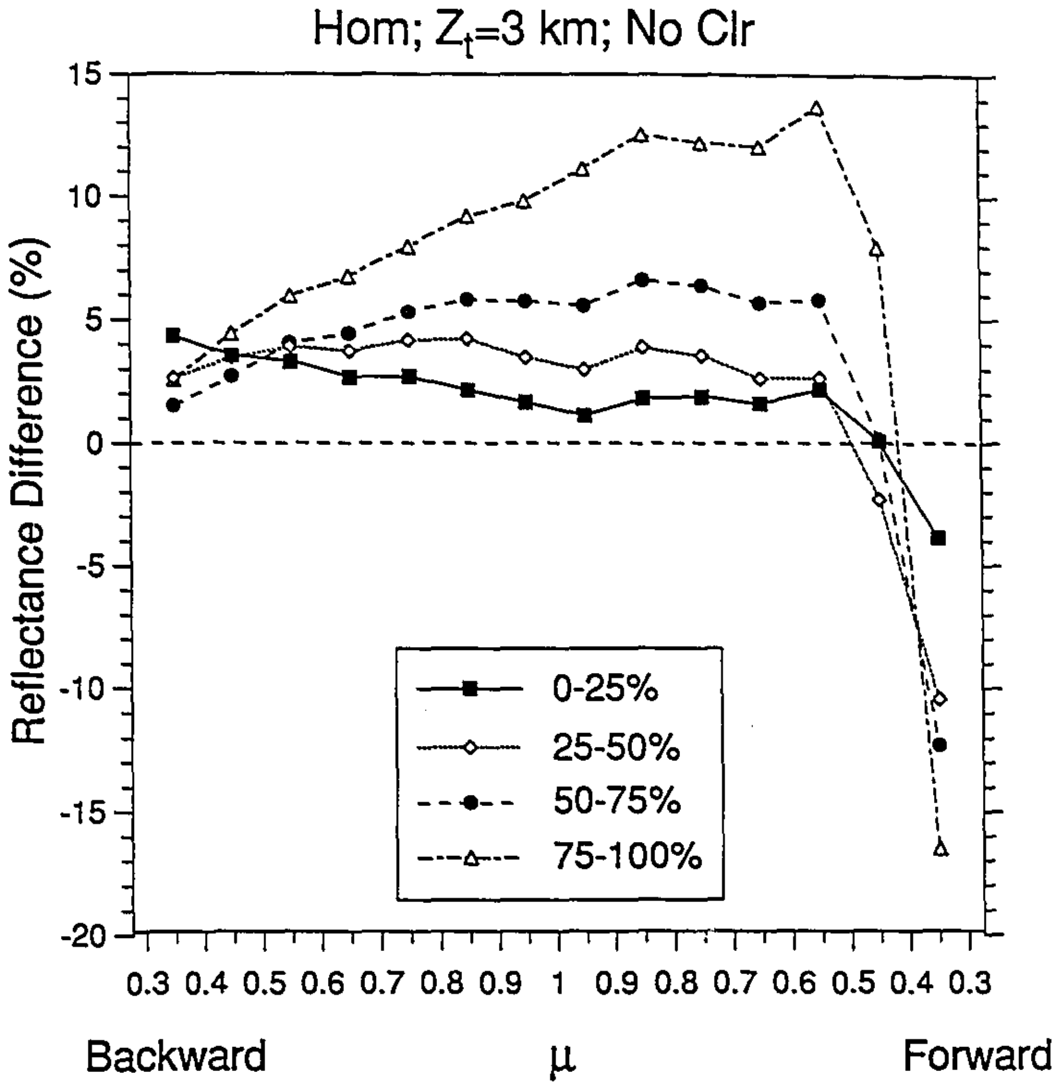
Hom; Z_t=3 km; No Clr
Reflectance Difference (%)
15
10
5
0
-5
-10
-15
-20
0-25%
25-50%
50-75%
75-100%
0.3 0.4 0.5 0.6 0.7 0.8 0.9 1 0.9 0.8 0.7 0.6 0.5 0.4 0.3
Backward
μ
Forward

(c)

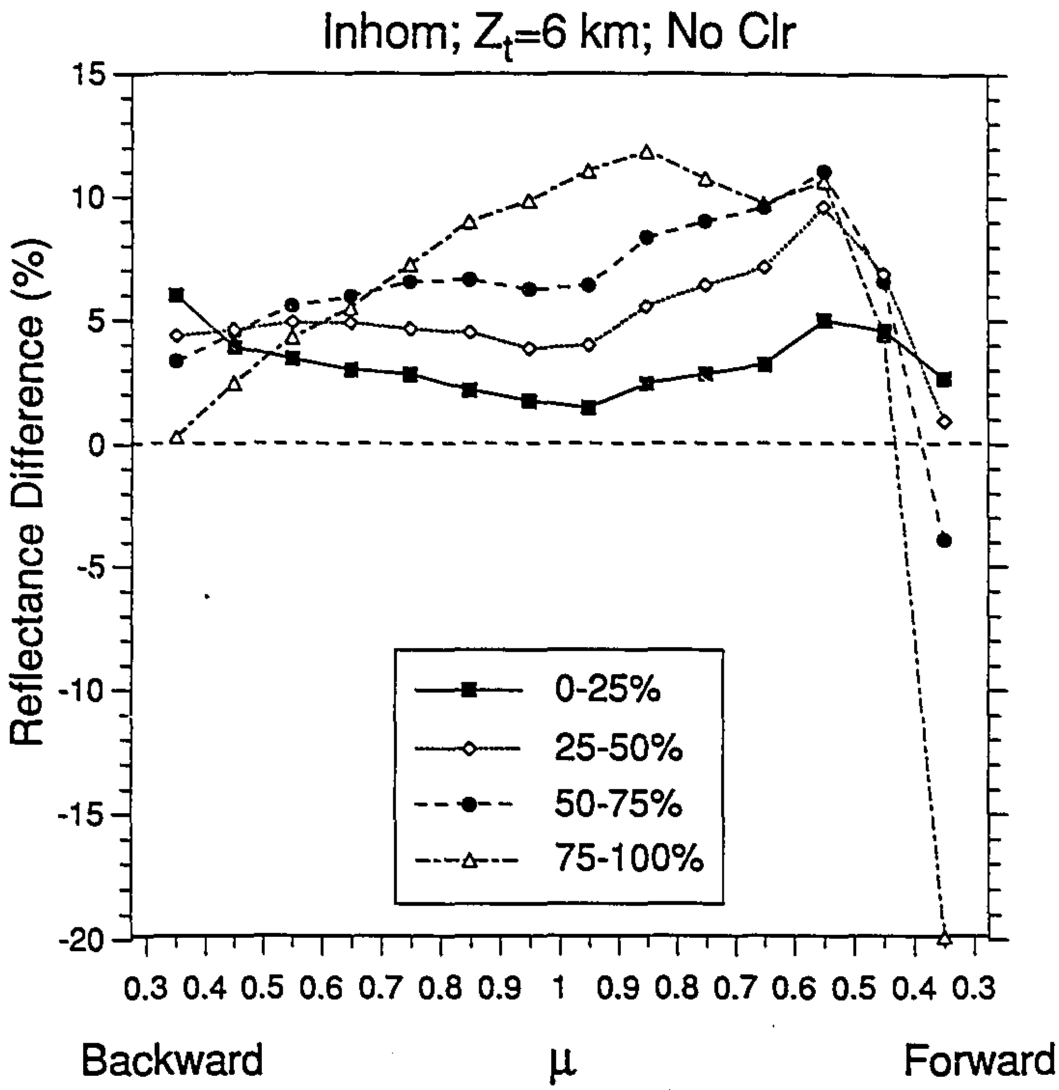

(d)

Figure 3.8 Reflectance differences between the observations and calculations for: (a) inhomogeneous approximation with Z_t=3 km; (b) same as (a) but excludes thick ice clouds; (c) homogeneous approximation with Z_t=3 km; and (d) inhomogeneous approximation with Z_t=6 km.

oblique view angles results from the fact that the shape of the observed and calculated reflectance frequency distributions are so similar at small μ (Fig. 3.5 (a) and (b)). In contrast, since the nadir observed frequency distribution has a much higher frequency of large reflectances, differences tend to be greater for the brightest clouds.

While these results show some sensitivity to the assumptions used in the analysis, the overall behavior is quite similar in each case. The largest discrepancy in the backscattering direction occurs in Fig. 3.8 (d), which shows a much smaller reflectance difference for the brightest 25% of the cases at small μ when a cloud top height of Z_t=6 km is assumed in the calculations. This is likely because the calculations are more sensitive to the attenuation above the cloud at large values of cloud fraction and cloud optical depth (i.e. for brighter clouds). When attenuation above the cloud is low and τ_p and f are large, calculated reflectances tend to increase more strongly with decreasing μ. Since this sensitivity is less pronounced at smaller τ_p and f (i.e. darker clouds), this behavior is not observed in the other percentile intervals in Fig. 3.8 (d).

In the forward scattering direction, reflectance differences show a larger sensitivity to pixel brightness. For μ>0.5, differences increase slightly with decreasing μ, and then suddenly decrease at very oblique view angles. In fact, for the brightest clouds, plane parallel reflectances exceed the observations at μ=0.3-0.4 in all of the cases shown. The reason for this behavior is due to the tendency for the observed reflectances to level off at small μ (Fig. 3.3 (a); Fig. 3.7). Differences are especially large when the clear sky attenuation above the cloud is low—the calculations exceed the observations by as much as 20% (Fig. 3.8 (d)). When reflectance differences were compared for different percentile intervals at μ_o=0.7-0.8 (not shown), no appreciable dependence on pixel brightness was observed, and relative differences remained less than ≈5% at all μ.

Overall, these results show that regardless of pixel brightness (or cloud thickness), the plane parallel model provides reflectances that are within ≈20% (relative difference) of the observations at small μ and μ_o in the backscattering direction, and within ≈5% for μ_o>0.45. In the forward scattering direction, while the plane parallel reflectances tend to exceed observed values for the brightest clouds at small μ and μ_o, this is highly sensitive to what model assumptions are used in the calculations.

3.3.3 Relative Azimuth Dependence

Fig. 3.9 (a) compares average observed and plane parallel reflectances as a function of relative azimuth for μ_o=0.1-0.2 at μ=0.3-0.4. Errors in the mean observed reflectances are larger in certain ϕ bins due to reduced sampling and because a smaller bin size was used in this comparison (10° instead of 30°). Overall, the plane parallel model appears to provide a reasonable representation of the ϕ dependence in the observations. In the forward scattering direction, both the observed and plane parallel reflectances increase rapidly with decreasing ϕ, and the observations fall well within the range of values provided by the plane parallel model. The sensitivity to the effect of the clear sky above the cloud and to the type of approximation used in the normalization of the calculations (i.e. either "inhomogeneous" or "homogeneous") is also clearly illustrated. For ϕ<70°, the calculations appear to be more sensitive to the attenuation by the atmosphere above the cloud than to the details of the normalization procedure.

In the side and backscattering directions, the ϕ dependence in the calculations is also fairly similar to that of the observations, regardless of what model assumptions are used in the calculations. The largest differences occur between ϕ=70°-140° and between 170°-180°, where observed reflectances are approximately 6% larger than the plane parallel values (≈15%-20% relative difference). Between ϕ=140°-170°, differences are generally less than 3% (≈6% relative difference).

For μ=0.7-0.8, Fig. 3.9 (b) shows that the ϕ dependence in the observations is very well represented by the plane parallel model calculations. While the observations exceed

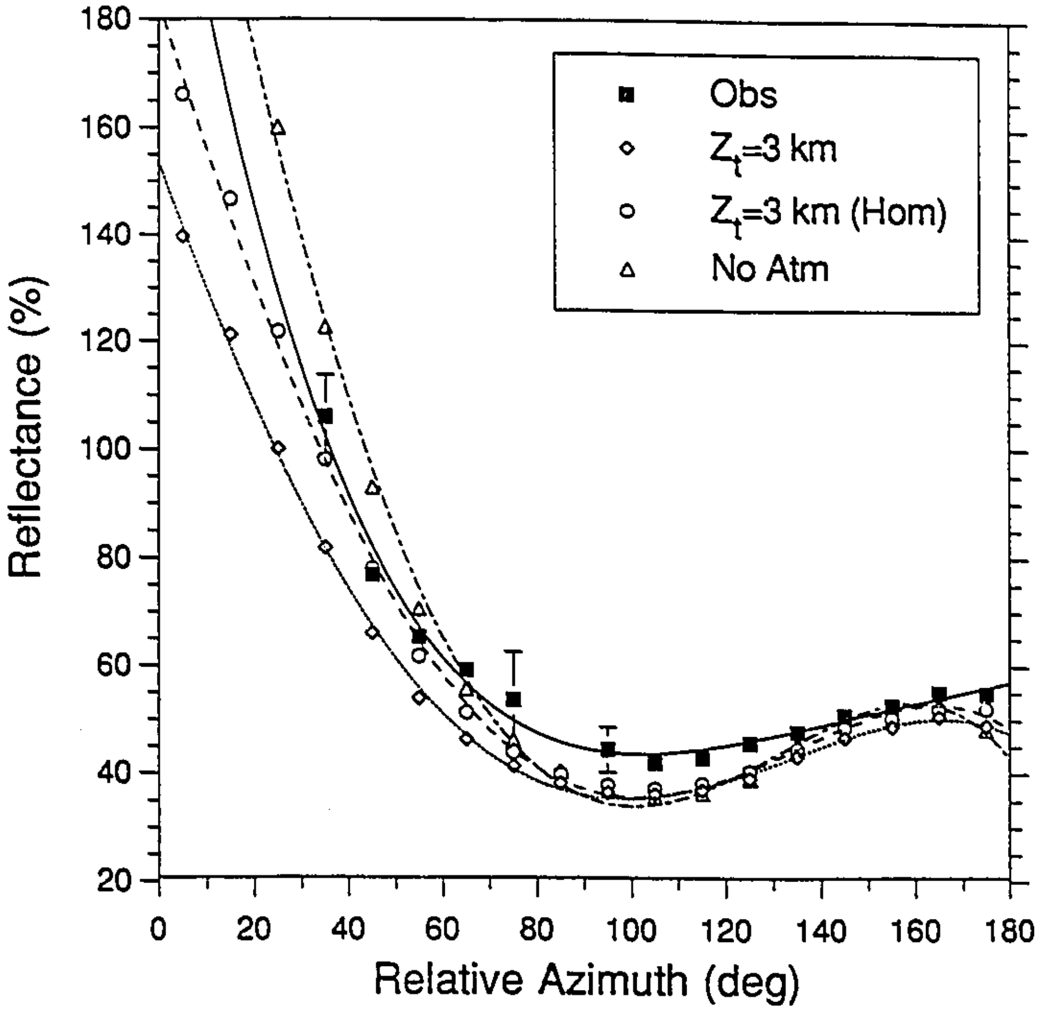

180
160
140
120
100
80
60
40
20
0
20
40
60
80
100
120
140
160
180
Reflectance (%)
Relative Azimuth (deg)
Obs
Z_t=3 km
Z_t=3 km (Hom)
No Atm

(a)

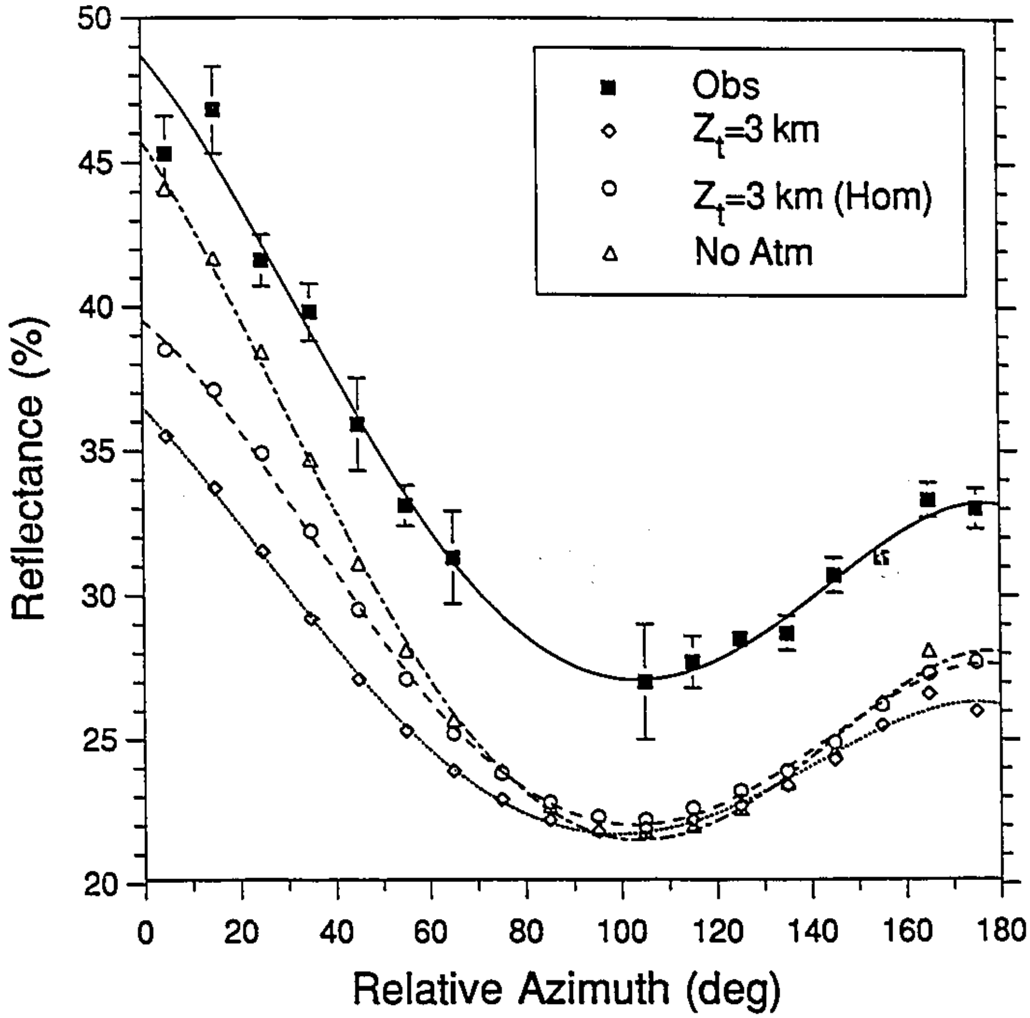

(b)

Figure 3.9 Average observed and plane parallel reflectances as a function of relative azimuth for μ_0=0.1-0.2 at (a) μ=0.3-0.4 and (b) μ=0.7-0.8.

the calculations by a constant amount of ≈6% (≈20% relative difference), the observed and calculated reflectances do however vary with ϕ in a very similar manner.

3.3.4 Pixel Area Expansion

In order to examine whether the neglect of pixel area expansion in the calculations affects the results, comparisons between observations and calculations were also performed after degrading the data in each field-of-view to a constant spatial resolution equal to that at μ=0.35 (following Ye and Coakley, 1994a). The data is degraded by averaging reflectances from an appropriate number of neighboring pixels whose combined area matches that of a single pixel at μ=0.35. This analysis accounts for the approximate 35% overlap in neighboring ERBS pixels (Kopia, 1986). Table 3.1 shows the number of pixels in each μ bin used to construct the constant FOV's along with their combined total area ("Simulated Pixel Area") and the relative difference from the actual pixel area at μ=0.35. As shown, relative differences between the simulated pixel areas and the actual ERBS pixel area at μ=0.35 are less than 10%.

μ bin	No. Of Pixels	Simulated Pixel Area (km^2)	Simulate Pixel Area Error (%)
0.35	1	25,782.9	0.0
0.45	2	23,580.5	-8.5
0.55	3	23,588.5	-8.5
0.65	7	25,573.1	-0.8
0.75	11	26,175.8	1.5
0.85	16	26,217.9	1.7
0.95	20	23,829.5	-7.6

Table 3.1 Number of ERBS pixels in each μ bin required to construct fields-of-view of constant area equal to the ERBS pixel resolution at μ=0.35. Also shown are the simulated pixel area and their associated errors.

Figs. 3.10 (a) and (b) show the cloud fraction and cloud optical depth frequency distributions at the full and degraded pixel resolutions, respectively. In Fig. 3.10 (a), cloud fraction frequency distributions were derived both when clear pixels were excluded from the analysis, and for comparison purposes, when all pixels (including the clear pixels) were considered. In both cases, differences between the full and degraded resolution cloud fraction frequency distributions tend to be small. In general, degrading the pixel resolution causes only a slight reduction in the frequency of very small (f=0.0-0.1) and of very large (f=0.9-1.0) cloud fractions. These differences are much smaller than what has been observed in studies involving high resolution sensors (Wielicki and Parker, 1992). Differences between full and degraded resolution cloud optical depth frequency distributions were also found to be slight (Fig. 3.10 (b))—average cloud optical depths for these cases were 9.4 for the full resolution case and 8.9 for the degraded resolution case.

Shortwave reflectance frequency distributions at μ_o=0.1-0.2 and μ_o=0.7-0.8 for both the full and degraded resolution observations and calculations are provided in Fig. 3.11 (a) and (b), respectively. As shown, degrading the pixel resolution has very little effect on the frequency distributions. Overall, relative differences between full and degraded resolution reflectance standard deviations were found to be less than 10%. Thus, the neglect of pixel area expansion in the calculations does not appear to have much of an influence on the comparisons.

While the effect of pixel area expansion may be small when compared with a constant FOV size equal to that at μ=0.35, it is not immediately clear how these results would change if a smaller constant FOV size, such as that corresponding to pixels at nadir, were used at all μ. Unfortunately, this cannot be examined using ERBS data alone, but would require measurements from a higher resolution sensor (e.g. AVHRR). In all likelihood, this would probably result in a stronger increase in reflectance with decreasing μ since cloud-contaminated scenes viewed obliquely would generally contain more cloud within

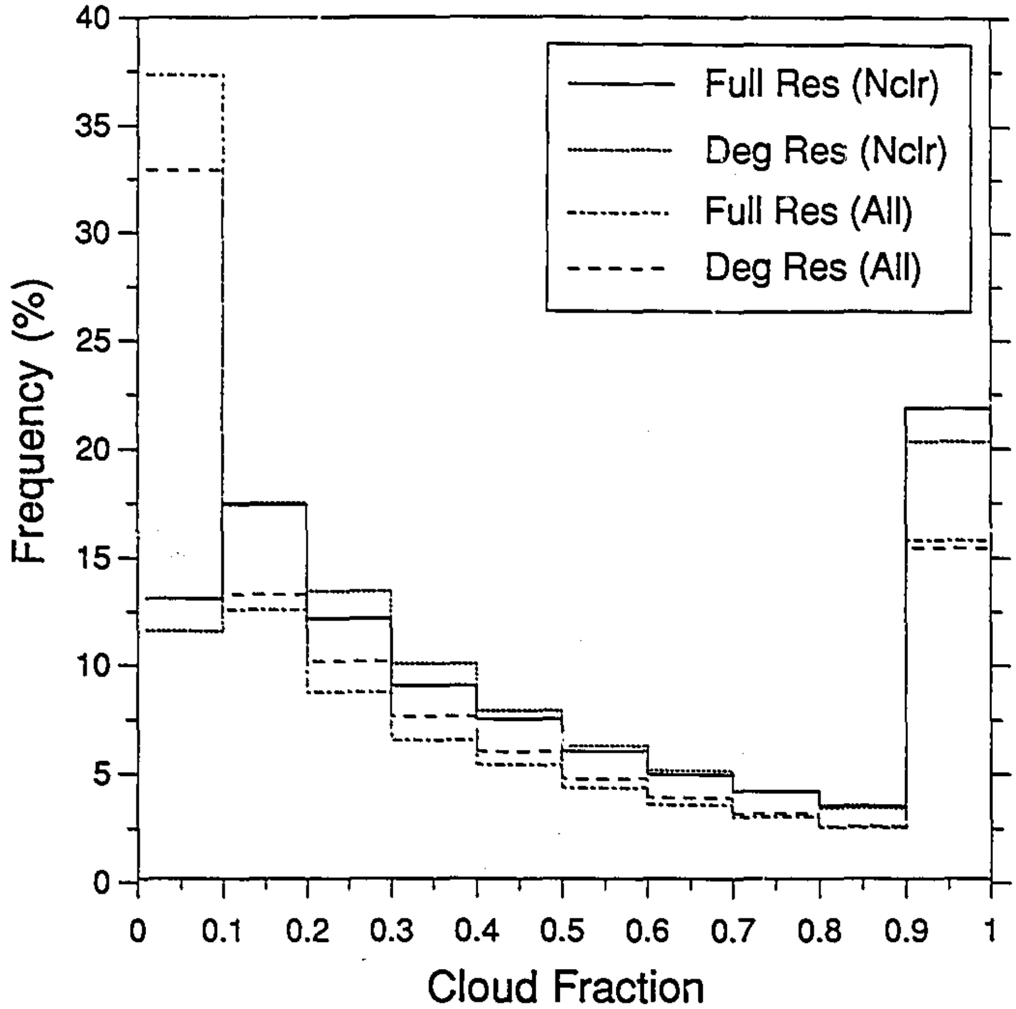

Full Res (Nclr)
Deg Res (Nclr)
Full Res (All)
Deg Res (All)
Frequency (%)
Cloud Fraction
0
5
10
15
20
25
30
35
40
0
0.1
0.2
0.3
0.4
0.5
0.6
0.7
0.8
0.9
1

(a)

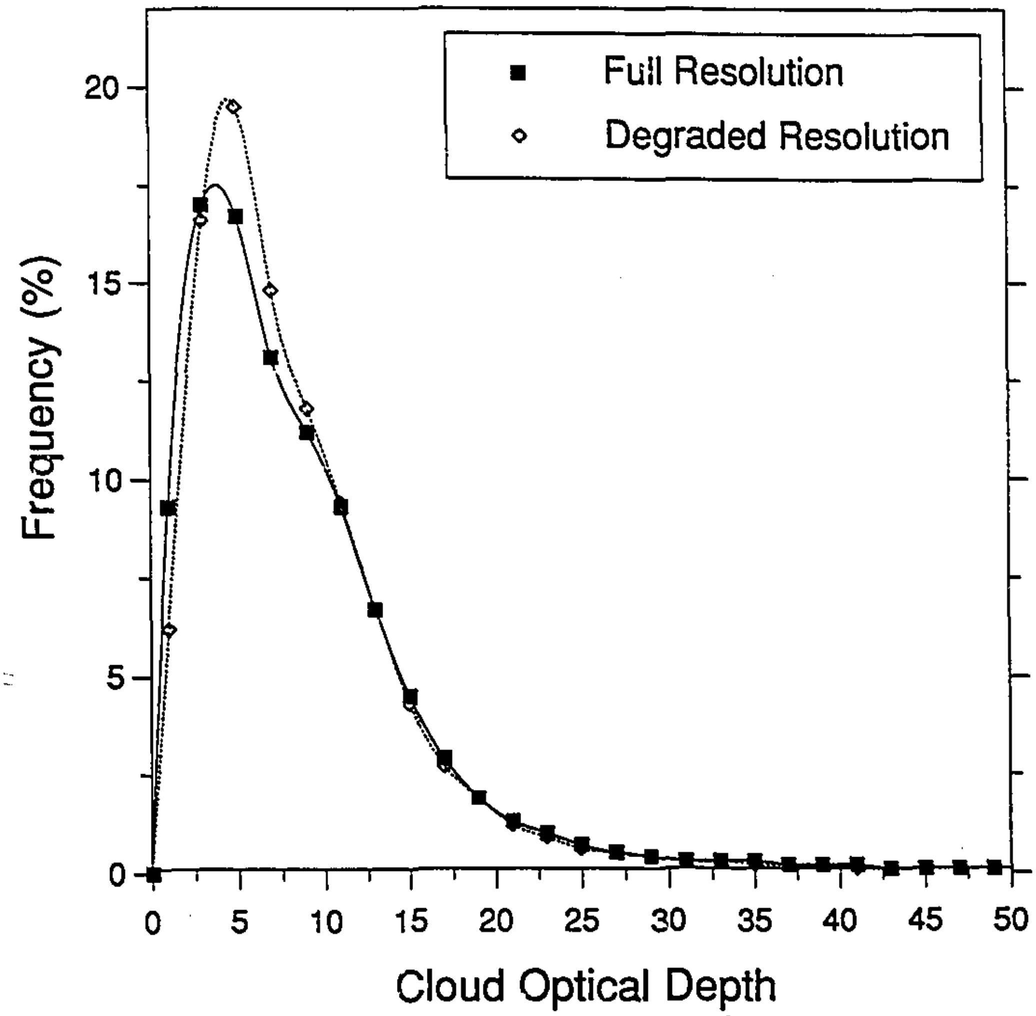

(b)

Figure 3.10 (a) Cloud fraction and (b) cloud optical depth frequency distributions obtained from nadir observations for the full and degraded pixel resolutions.

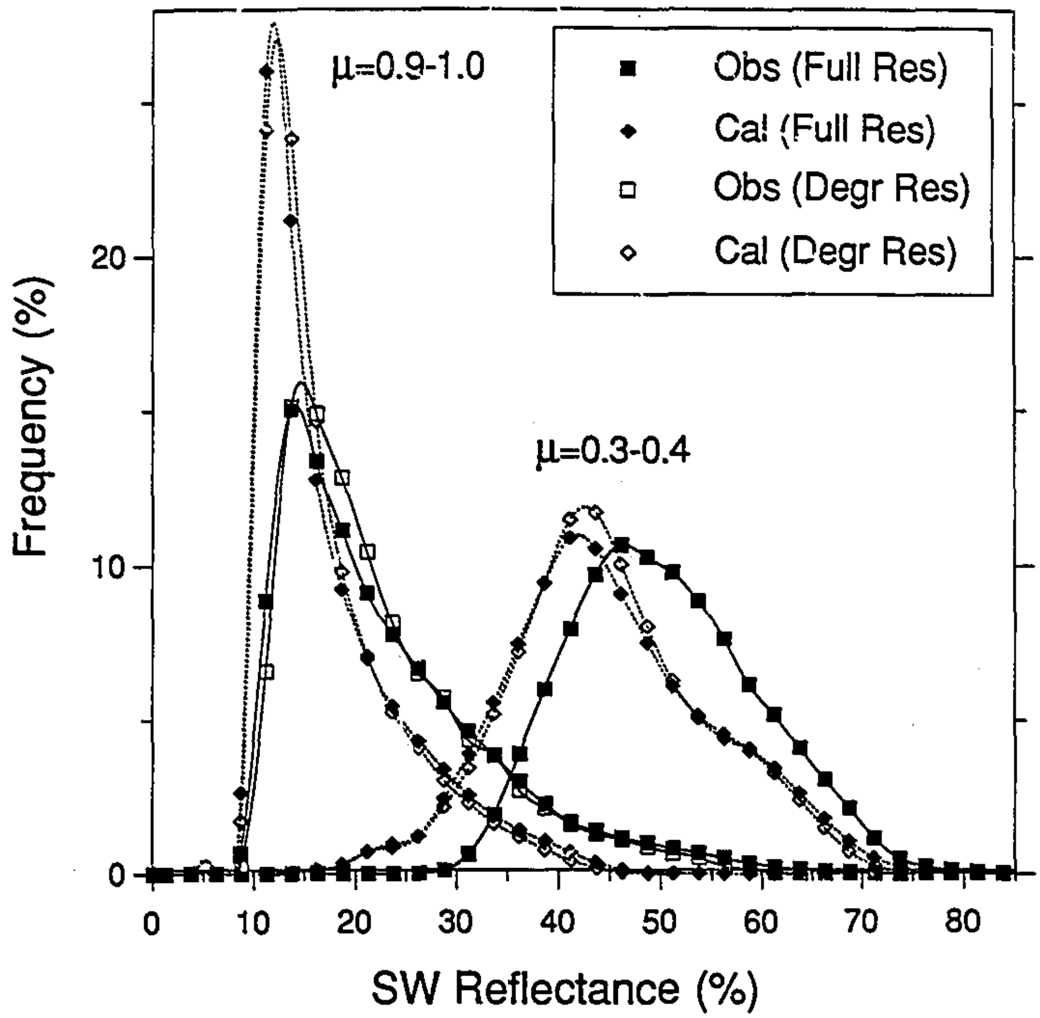

μ=0.9-1.0
μ=0.3-0.4
Obs (Full Res)
Cal (Full Res)
Obs (Degr Res)
Cal (Degr Res)
Frequency (%)
SW Reflectance (%)
0
10
20
30
40
50
60
70
80

(a)

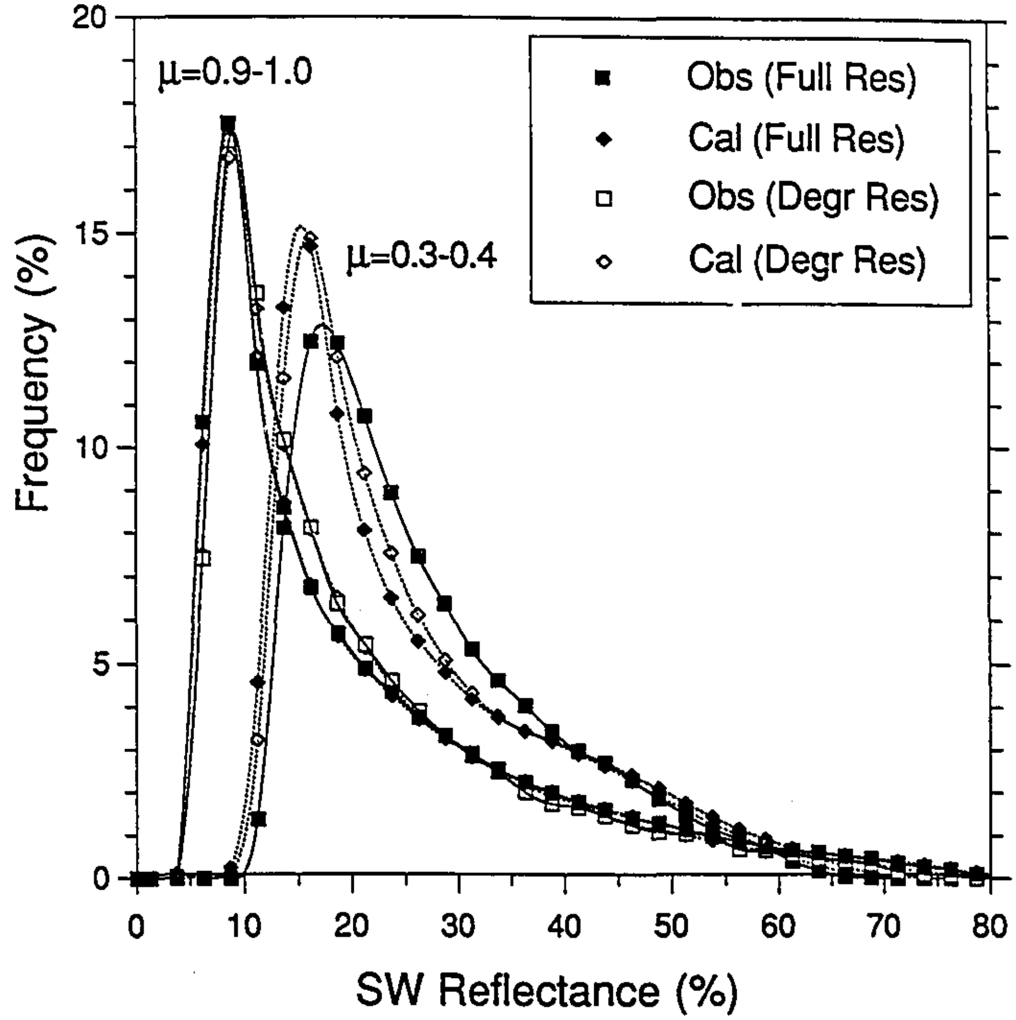

(b)

Figure 3.11 Shortwave reflectance frequency distributions for (a) μ_o=0.1-0.2 and (b) μ_o=0.7-0.8 for the full and degraded resolution observations and calculations.

the pixel. However, if the sensitivity to pixel resolution at small μ is at all similar to that shown in Fig. 3.11 for μ=0.9-1.0, the magnitude of any such changes would likely be small.

3.3.5 Reciprocity

Because of limitations associated with orbit-dependent sampling biases inherent in satellite measurements, there is often a need in remote sensing applications to "fill in" missing or unreliable data in certain view and solar zenith angle bins by using empirical or theoretical techniques. This problem often arises at very oblique view angles (e.g. μ<0.3) where satellite measurements may be less dependable, and at low sun elevations, where data is often missing. In the latter case, the problem is typically encountered when measurements are taken from instruments in sun-synchronous orbits, where there is a high degree of correlation between solar zenith angle and latitude.

A common theoretical approach which is often used in dealing with this problem is a simplified version of the Helmholtz Principle of Reciprocity. For a (locally) one-dimensional horizontally homogeneous medium, the general Helmholtz principle of reciprocity reduces to a simple directional principle for plane parallel atmospheres given by the reciprocal relation $R_A(\mu_A,\mu_B,\phi) = R_B(\mu_B,\mu_A,\phi)$, where R_A is the reflectance in the direction (μ_A, ϕ) due to insolation from the direction (μ_B, ϕ), and vice versa for R_B (Chandrasekhar, 1950). Thus, if measurements are missing in certain angular bins, measurements from the corresponding reciprocal incident and view angle bins can be used to "fill-in" the missing data.

Strictly speaking, however, this principle only really applies for plane parallel atmospheres. Therefore, it can be also interpreted as a necessary (but not sufficient) condition for the application of plane parallel theory to the analysis of real measurements (Davies, 1994). If observations violate directional reciprocity, then direct application of 1D theory to real measurements would be inappropriate. In order to test whether or not real measurements satisfy reciprocity. Davies (1994) compared autocorrelation functions for reciprocal pairs of reflected shortwave radiances measured by the ERBS scanner for April-July 1985 within 30° of the equator. When autocorrelations at zenith sun as a function of μ were compared with those measured at nadir as a function of μ_o, differences tended to be quite large when clouds were present (for clear scenes reciprocity was obeyed). As a result, it was concluded that directional reciprocity does not apply at the ERBS pixel scale owing to inherent horizontal inhomogeneities in real measurements containing clouds.

It is not immediately clear from that study how these horizontal inhomogeneities affect the reflection field. For example, is reciprocity violated because horizontal inhomogeneities cause the μ dependence in reflectance to change (compared to 1D theory), or is it because of their effect on the μ_o dependence and thus the scene illumination? To gain some insight, it is useful to directly compare observations with calculations based on 1D theory. While it is not feasible to use the spatial autocorrelation function for this purpose, a suitable alternative is to use the shortwave reflectance standard deviation. Using the same approach outlined in the previous sections, observed and calculated standard deviations were compared for reciprocal pairs as a function of μ and μ_o (all pixels were degraded to the resolution at μ=0.35).

Results of this comparison are provided in Fig. 3.12 which shows observed and plane parallel model reflectance standard deviations for the reciprocal sets of angles at μ=0.9-1.0 as a function of μ_o, and μ_o=0.9-1.0 as a function of μ in the backscattering direction. Note that in the latter case, standard deviations could only be obtained for μ>0.3 since beyond this point, the observations are unreliable (Section 2.1). As shown, the observed standard deviations for the reciprocal pairs are quite different, whereas the calculated values are virtually identical (a slight difference in the calculated values occurs because of minor differences in the R^{CLR} values). In all cases, observed standard deviations are found to

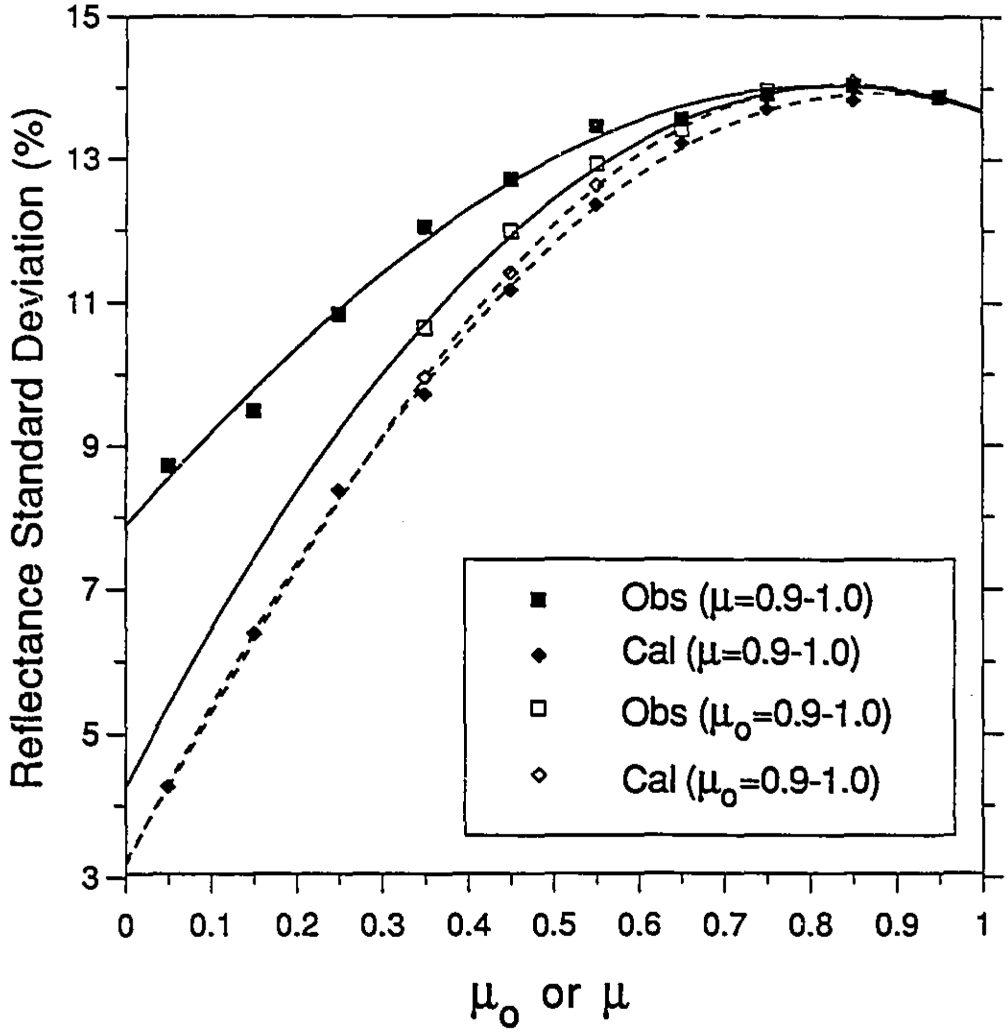

Figure 3.12 Observed and plane parallel model reflectance standard deviations for the reciprocal sets of angles μ=0.9-1.0 as a function of μ_o, and μ_o=0.9-1.0 as a function of μ in the backscattering direction.

exceed the corresponding plane parallel values. Interestingly, the largest deviation from 1D theory occurs in the nadir observations for different μ_o, and these differences become progressively larger as μ_o decreases.

Thus, when scenes containing clouds are illuminated obliquely and observed at nadir, the statistical properties in the reflectance field appear to be more sensitive to horizontal inhomogeneities than when the same scenes are viewed obliquely for overhead sun. Consequently, the main reason for the breakdown in reciprocity in the observations appears to be due to the difference in the way observed reflectances depend on μ_o compared to 1D theory.

3.4 Discussion

While the results presented in this chapter are generally consistent with what theoretical studies show, there are some notable differences. At high sun elevations, the fact that plane parallel reflectances showed excellent agreement with the observations is consistent with 3D results. Kobayashi (1993) showed that for sun angles close to zenith, differences between 3D and plane parallel cloud reflectances tend to be smaller at oblique view angles than at nadir, where diffusive leakage through the sides of 3D clouds tends to lower the reflectance relative to 1D clouds. Given that the plane parallel reflectances were normalized at nadir for large μ_o in the present study, we can only really confirm that at oblique view angles, these results are consistent. At smaller μ_o, the tendency for reflectance differences to increase is also apparent in theoretical studies (e.g. Davies, 1984; Bréon, 1992; Kobayashi, 1993). In the backscattering direction, these studies have shown that 3D clouds tend to scatter more radiation due to the influence of the cloud sides. However, the lack of any μ dependence in the reflectance differences between the observations and plane parallel calculations is surprising. This behavior is only apparent in theoretical results for clouds of low aspect ratio. Reflectances from vertically extensive 3D clouds generally show a much stronger increase with view angle than what the observations presented here have shown. The reason for this discrepancy is unclear. While it may be tempting to conclude that real clouds viewed obliquely at low spatial resolutions behave more like horizontally extensive layers, this doesn't make intuitive sense especially given that tropical clouds were considered here. Rossow (1989) notes that since the pixel size is of order or greater than the path length of visible radiation, multiple scattering within and between clouds may eliminate most of the deviations from 1D behavior. This is also an unlikely explanation since cloud fractions in the present study are estimated to be quite low on average (≈0.4)—so that multiple scattering between clouds is likely to be quite small on average. Another possible reason may be associated with the absorption properties of the clouds. Past studies have shown that theoretical models may actually underestimate the absorption by clouds compared to observations (Stephens and Tsay, 1990). While increasing the absorption could lead to a slightly weaker view angle dependence in the reflectance from 3D clouds, and thus reduce differences between 3D and 1D calculations in the backscattering direction, previous broadband comparisons of cloud albedo between theory and observations do not support this. Stephens and Tsay (1990) cite examples in the literature which show that while much more absorption occurs in observations than what is predicted by theory at near infrared wavelengths (≈1.0 μm), broadband results are generally quite consistent.

In the forward scattering direction, the tendency for plane parallel reflectances to be larger than the observations at small μ is qualitatively consistent with 3D theory. This can be attributed to the leakage of radiation through the sides of the clouds (Chapter 4).

3.5 Summary

This chapter has shown that, on average, differences between observed and plane parallel reflectances are less sensitive to changes in μ and ϕ than they are upon μ_o. In general, reflectance differences tend to increase with decreasing μ_o at all μ. Thus, the μ_o reflectance bias observed at nadir in Chapter 2 also appears to affect off-nadir reflectances as well. Provided atmospheric effects above the cloud are taken into account, observed reflectances exceed plane parallel values in the backscattering direction by roughly a constant amount, on average, at all μ. When stratified by pixel brightness (or cloud thickness), however, reflectances at oblique view angles show a different result from that at nadir: reflectance differences were $\leq 5\%$ at oblique view angles for $\mu_o>0.45$, and $\leq 20\%$ at smaller μ_o, regardless of cloud thickness. In the forward scattering direction, the calculated reflectances show more sensitivity to the model assumptions, and consequently, observed reflectances generally fall within the range of plane parallel model values. Despite this, the observations do show a very different behavior at small μ—observed reflectances appear to level off between μ=0.5 and μ=0.3, whereas the calculations show a steady increase.

Overall, the relative azimuth dependence in the observations was found to be well represented by the plane parallel model at all μ and μ_o. A very large sensitivity to the model assumptions (especially to attenuation by the clear sky above the cloud top) was however observed in the forward scattering direction.

Chapter 4

Monte Carlo Simulations

4.1 Introduction

In this chapter, we turn to Monte Carlo model simulations in order to examine whether the results in Chapters 2 and 3 are consistent with what is expected based on 3D cloud theory. The approach used is to compare 3D and plane parallel cloud reflectances directly, in a manner similar to the comparisons between the observations and plane parallel calculations in the previous chapters. The aim here is to see whether the two sets of comparisons show similar qualitative results. If 3D effects are indeed responsible for the differences between the observations and plane parallel calculations, then similar differences should appear in the comparisons between the 3D and 1D cloud models.

The 3D cloud effects considered in this chapter are associated with the external properties of the clouds (i.e. the external inhomogeneities). In particular, the influence of the cloud sides and the cloud top structure (i.e. "bumpiness") on the reflectance field are examined in detail. Internal inhomogeneities, which result from small-scale liquid water content variations within clouds are not included in the 3D simulations. While the omission of internal inhomogeneities may have some effect on the reflectance at high solar elevations (Cannon, 1970; Cahalan, 1989; Davis et al., 1990), their effect is likely smaller than larger scale inhomogeneities (e.g. cloud vs clear regions, external cloud properties), and should not affect the reflectance field at small μ_0.

The following section briefly describes the Monte Carlo method and the cloud fields considered in the simulations. Then, comparisons between 3D and 1D calculations are performed as a function of μ_0 (Section 4.3) and as a function of view angle (Section 4.4).

Similarities and differences between the 3D and 1D model comparisons and the results in Chapters 2 and 3 are highlighted throughout.

4.2 Monte Carlo Method

The Monte Carlo method of solving radiative transfer problems has widely been used in the past to examine the radiative properties of 3-D cloud fields (Busygin et al., 1973; McKee and Cox, 1974; Wendling, 1977; Davies, 1978; Welch and Wielicki, 1984; Kobayashi, 1988; Barker and Davies, 1992). The method involves a numerical simulation of the interaction between photons and a scattering medium based on physical laws governing these interactions. Photons are traced through the medium (taking optical thickness, phase function and single scattering albedo into account) until they escape the medium. Each interaction is governed by the path length between successive collisions of the photon, and the travel directions before and after one interaction.

In this study, the Monte Carlo code was provided by Várnai (1995, personal communication). Simulations are carried out at a wavelength of 0.865 μm using a Mie phase function for the Sc_{top} cloud model of Welch et al. (1980). While the model can handle atmospheric effects and surface reflection, these were not included here in order to concentrate specifically on clouds. This should not have much effect on the results since, at 0.865 μm, atmospheric effects tend to be small, and surface contributions are low over ocean anyway. The model divides the cloud field into boxes/grid points, each having a resolution r. It assumes periodic boundary conditions, so that photons leaving one side of a cloud field boundary come back at the opposite side. In all simulations, the number of photons used was 10^6, which gives a reflectance uncertainty of less than 1% (Várnai, 1995, personal communication).

The advantage of the Monte Carlo approach is that it can determine radiative properties of any cloud geometry. Here simulations are carried out using stochastic, isotropic, scale-invariant broken cloud fields (Barker and Davies, 1992). The cloud fields are characterized by continuous power spectra, and as a first approximation, their structure is represented by the cloud fraction and the slope of the wavenumber spectrum of cloud optical depth. For cloud fields which have isotropic spectral densities, the ensemble averaged, one-dimensional spectra $\langle S_k \rangle$ scale according to k^{-s}, where k is the wavenumber and s is the cloud field scaling exponent. The greatest departure from plane parallel clouds occurs for s=0 (white noise), and as s increases, the number of small clouds decreases, and the variability across individual clouds decreases (i.e. clouds become more plane parallel). In the present study, stochastic cloud fields are generated for various cloud fractions (f) and domain optical depths (τ_d) using the following scaling: $\langle S_k \rangle \sim k^{-1}$ for $k \leq 6$, and $\langle S_k \rangle \sim k^{-3.6}$ for $k > 6$. Cloud fields are defined over a 512x512 grid with a gridpoint resolution r=68.7 m, and a constant β_e=30 km^{-1} is assumed (i.e. no internal inhomogeneities). Fig. 4.1 illustrates the cloud field for f=0.5 and τ_d=5. While this scene does appear to have characteristics which resemble a real cloud scene, it clearly does not represent the entire range of cloud variability that can be encountered over the course of one year. Nevertheless, it does serve to demonstrate, at least qualitatively, the kinds of differences that may be expected between 3D and 1D cloud reflectances. In order to examine the effect of cloud top structure, Monte Carlo simulations are also carried out using simple cloud shapes consisting of paraboloids, cones and cylinders for various aspect ratios.

4.3 Results

4.3.1 Nadir Simulation

As an illustration of how 3D effects can influence the μ_0 dependence in nadir reflectance, Fig. 4.2 shows a comparison between reflectances generated using the 3D cloud field ("R_{3D}") in Fig. 4.1 with plane parallel model calculations ("0.5 $R_P(\tau_p$=7.1)"). The plane parallel calculations were normalized at μ_0=0.95 by adjusting the cloud optical depth to fit the 3D result (taking cloud fraction into account). A cloud optical depth of

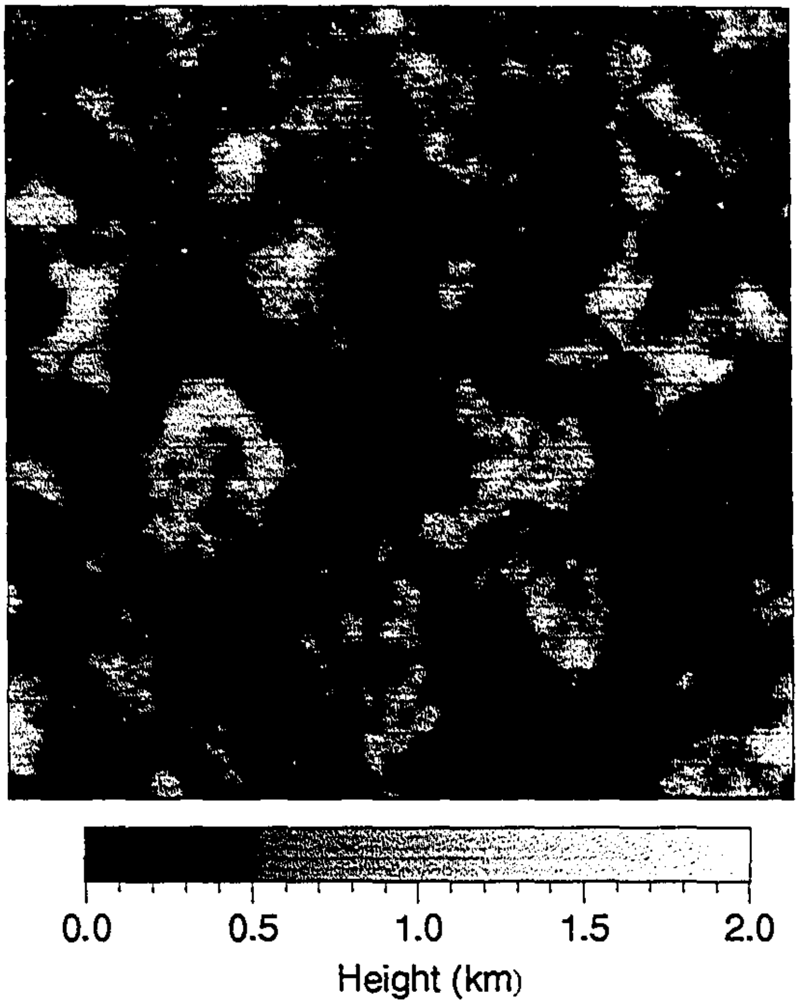

Figure 4.1 Stochastic cloud field used as input to Monte Carlo model calculations.

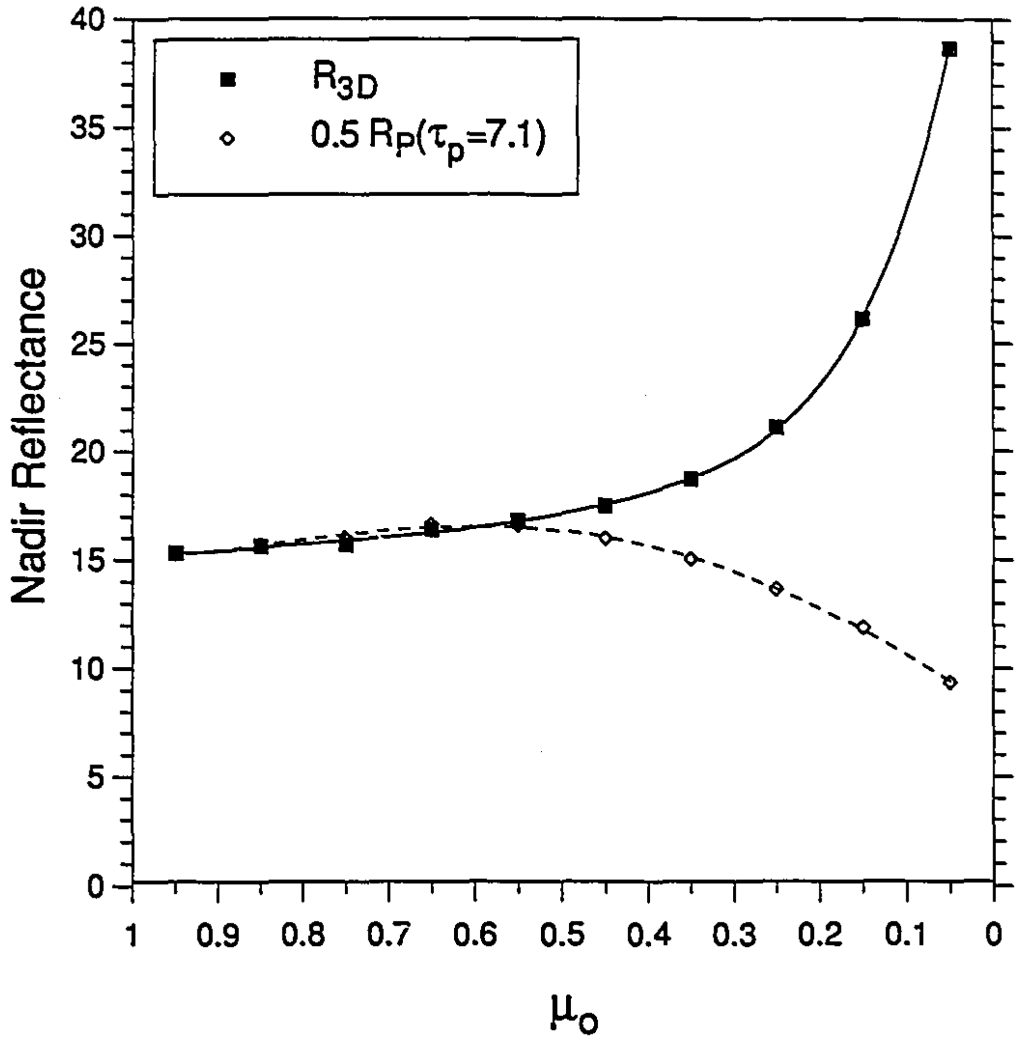

Figure 4.2 Nadir reflectance as a function of μ_o for the cloud field in Fig. 4.1 ("R_{3D}") and a plane parallel calculation normalized to R_{3D} at μ_o=0.95.

τ_p=7.1 was found to provide the best match in this case. As shown, the 3D reflectances increase with decreasing μ_o, while the opposite occurs for the 1-D result. This is qualitatively consistent with what was obtained from observations in Chapter 2, and illustrates the importance of 3D effects in explaining the discrepancies between the observations and 1-D theory.

To examine how these results depend on f, Fig 4.3 compares 3D reflectances for f=0.25, 0.50, 0.75 and 1.0 at τ_d=5, with a plane parallel calculation at the same optical depth. Since τ_d is kept constant, the average cloud optical thickness in the 3D cloud fields ($<\tau_{3D}>$) is inversely proportional to f (e.g. $<\tau_{3D}>$=20 for f=0.25; $<\tau_{3D}>$=10 for f=0.5; etc.). Thus, the cloud fields become more homogeneous with increasing f. For large μ_o, 1D reflectances are larger than 3D values because of diffusive leakage through the sides of the 3D clouds. This is a classic result which has appeared in many other studies involving Monte Carlo simulations (e.g. McKee and Cox, 1974; Wendling, 1977; Davies, 1978; Kobayashi, 1993). It also explains why a plane parallel cloud optical depth of only 7.1 rather than 10 provides a match between the 3D and 1D reflectance at μ_o=0.95 in Fig. 4.2. As μ_o decreases, 3D cloud reflectances increase rather substantially for f<1, while the case with f=1 decreases in a manner which is similar to the 1D result. This apparent agreement with 1D theory occurs because the cloud top is fairly uniform for this case, not because the cloud field is overcast. Reflectances for an overcast cloud field with larger horizontal variability in its cloud top structure (i.e. a bumpier cloud) can also deviate quite strongly from 1D results.

To illustrate, Fig. 4.4 shows reflectances generated from overcast cloud fields which were constructed by inserting a flat cloud base of optical depth τ_b=5 beneath the f=0.50 and f=0.75 cloud fields used in Fig. 4.3. These results are labeled "$<f_{3D}>$=0.50; $<\tau_{3D}>$=15", and "$<f_{3D}>$=0.75; $<\tau_{3D}>$=11.6", respectively, where $<f_{3D}>$ is the fraction of the domain containing bumpy cloud of average optical depth $<\tau_{3D}>$. Also plotted is a case

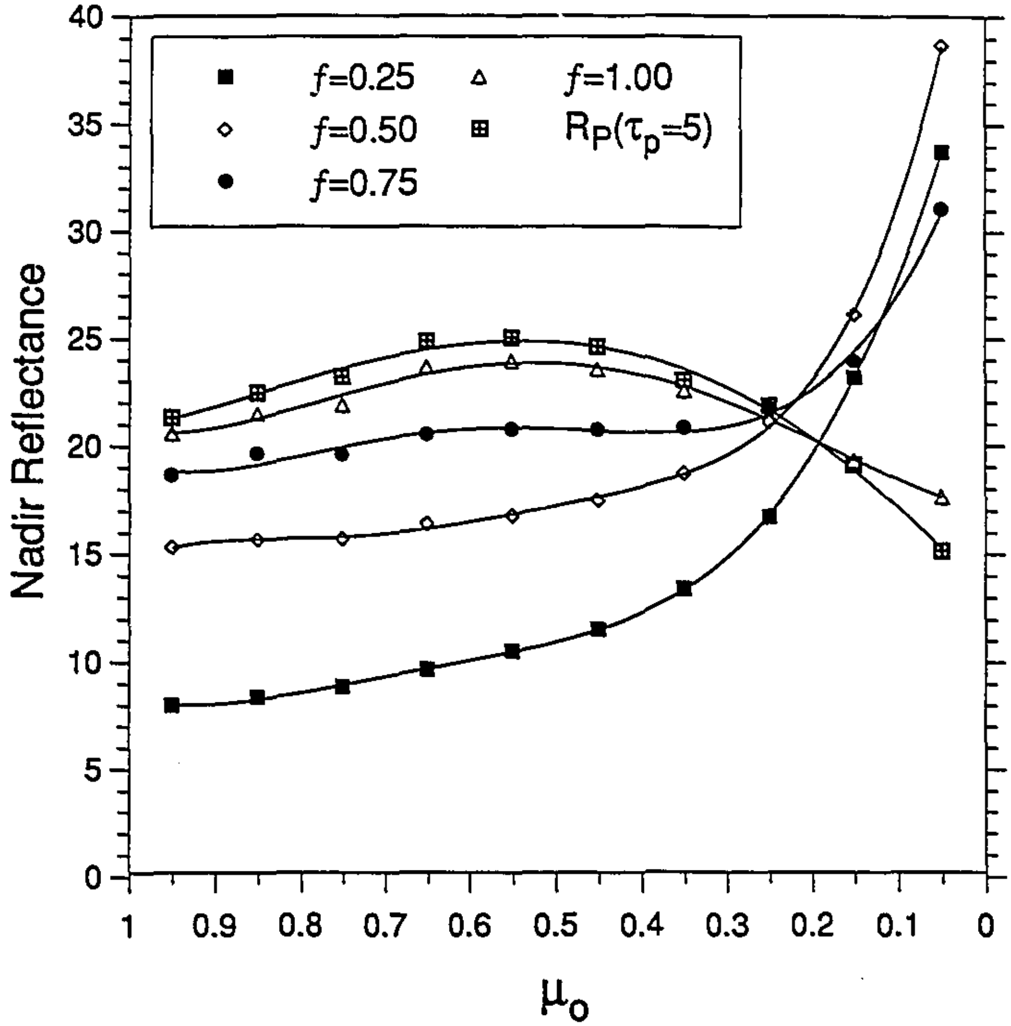

Figure 4.3 3D nadir reflectances as a function of μ_o for various cloud fractions (f) together with a plane parallel calculation at an optical depth $\tau_P=5$.

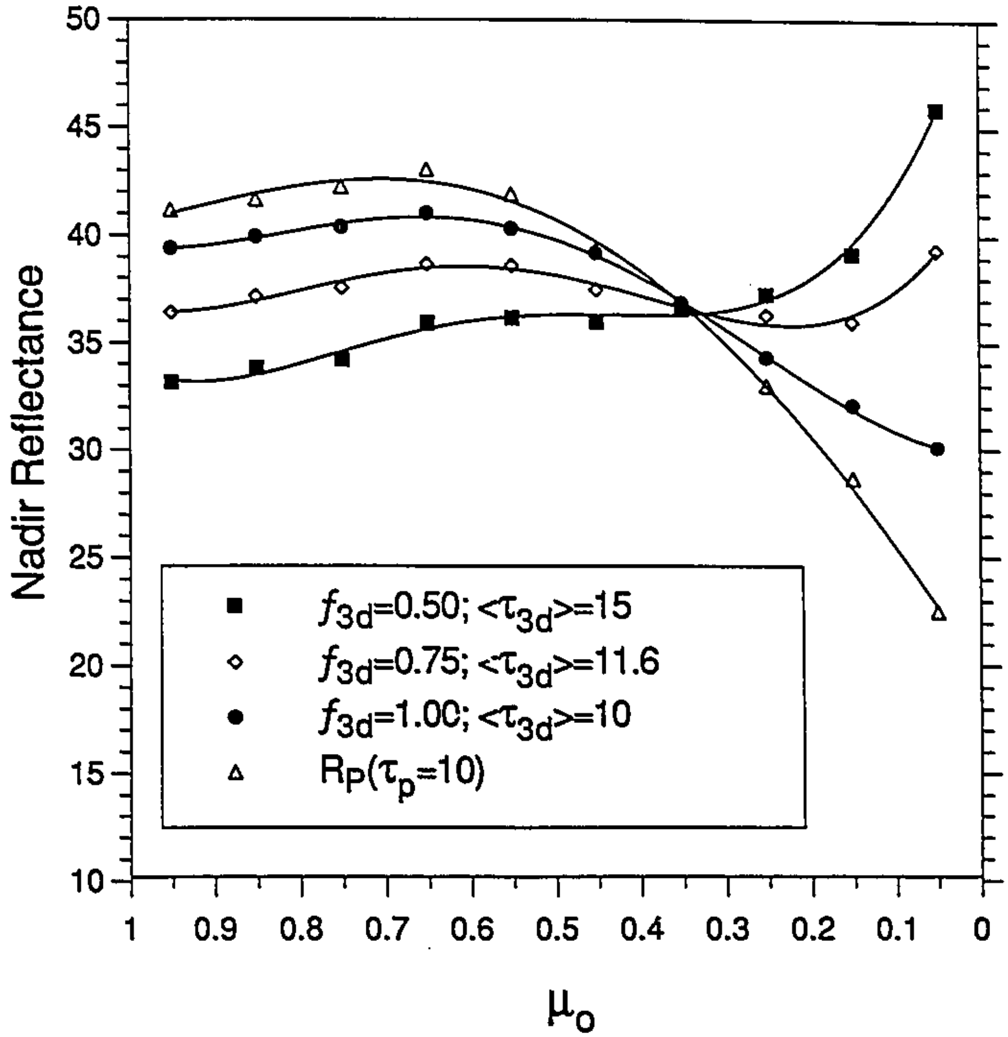

Figure 4.4 Reflectances generated from overcast cloud fields constructed by inserting a flat cloud base of optical depth τ_b=5 beneath the f=0.50 and f=0.75 cloud fields in Fig. 4.3. <f_{3D}> is the fraction of the domain containing bumpy cloud of average optical depth <τ_{3D}>. Also plotted is a plane parallel calculation at an optical depth of 10 ("$R_P(\tau_p$=10)").

with "$<f_{3D}>=1.0$; $<\tau_{3D}>=10$", and the plane parallel calculation at an optical depth of 10 ("$R_P(\tau_p=10)$"). For the "$<f_{3D}>=0.50$; $<\tau_{3D}>=15$" case (the most bumpy cloud field), a systematic increase in reflectance with decreasing μ_0 is obtained, while for the "$<f_{3D}>=0.75$; $<\tau_{3D}>=11.6$" case, the increase is less severe and occurs only at very low sun. Thus, provided the cloud tops are sufficiently inhomogeneous, significant differences between 3D and 1D results can occur even for overcast clouds. This result is somewhat surprising since many previous studies have shown that differences between 3D and 1D cloud fluxes tend to decrease substantially as cloud fraction approaches unity (Welch and Wielicki, 1984).

It has long been recognized that one of the main reasons for differences between the radiative properties of 3D and plane parallel clouds at low sun elevations is the influence of side illumination (McKee and Cox, 1974; Davies, 1978). As the sun becomes more oblique, a greater fraction of the incident solar radiation is intercepted by the sides of 3D clouds, resulting in more upward scattering than from a cloud of infinite extent. As a result, fluxes from 3D clouds tend to be larger. The degree to which side illumination occurs for a given cloud depends on cloud shape and cloud aspect ratio (defined as the ratio of the vertical dimension to the horizontal dimension). For a cloud field, the illumination enhancement also depends on the cloud fraction and the distribution of the cloud elements within the scene (Welch and Wielicki, 1984; Kobayashi, 1988). Past studies have focused on simple parameterizations of reflected flux in terms of an "effective cloud fraction", defined as the equivalent cloud fraction of a planiform field of clouds with the same vertical optical thickness required to give the same flux as that from a finite cloud field (Weinman and Harshvardhan, 1982; Harshvardhan and Thomas, 1984; Welch and Wielicki, 1984; Kobayashi, 1988). These parameterizations are, however, highly idealized due to the simple cloud geometries employed, and do not apply to remote sensing problems since this involves radiances/reflectances in a particular direction, not the overall flux.

To examine the effect of side illumination on the nadir reflectance dependence on μ_0, cloud fractions for the stochastic cloud fields were derived with respect to the solar direction in separate, slightly modified Monte Carlo simulations (Várnai, personal communication). In these simulations, once a photon hits a cloud, it is not allowed to continue its path. The number of photons intercepted by cloud divided by the number of incident photons gives the cloud fraction viewed from the solar direction. This definition of cloud fraction is equivalent to that obtained by the product of cloud fraction at μ_0=1 and the area enhancement ratio, defined as the ratio of the cloud area at μ_0 projected onto a horizontal surface to the cloud area at μ_0=1 (Welch and Wielicki, 1984). Fig. 4.5 shows cloud fraction ($f^*(\mu_0)$) as a function of μ_0 for the cloud field in Fig. 4.1 (f=0.5), as well as for cases with f=0.25 and f=0.75. Comparing these with the nadir reflectances in Fig. 4.3, there does indeed appear to be a strong link between the corresponding curves—the $f^*(\mu_0)$ curves show a dependence on μ_0 which is quite similar to that of the nadir reflectance.

If enhanced cloud illumination were the only factor in explaining the increase in nadir reflectance with decreasing μ_0, we might expect agreement between 3D and plane parallel results if the enhancement effect were taken into account in the plane parallel calculations. As a test, the plane parallel calculations were modified by scaling the reflectance at a given τ_p by $f^*(\mu_0)$ instead of f. Fig. 4.6 shows reflectances for the 3D cloud field in Fig. 4.1, together with a plane parallel calculation which assumes f=0.5 at all μ_0, and a case which uses $f^*(\mu_0)$. While this new approach increases reflectances at small μ_0, reflectances are still much lower than those for the 3D case. Similar results were obtained in comparisons at f=0.25 and f=0.75 (not shown). Thus, while side illumination appears to

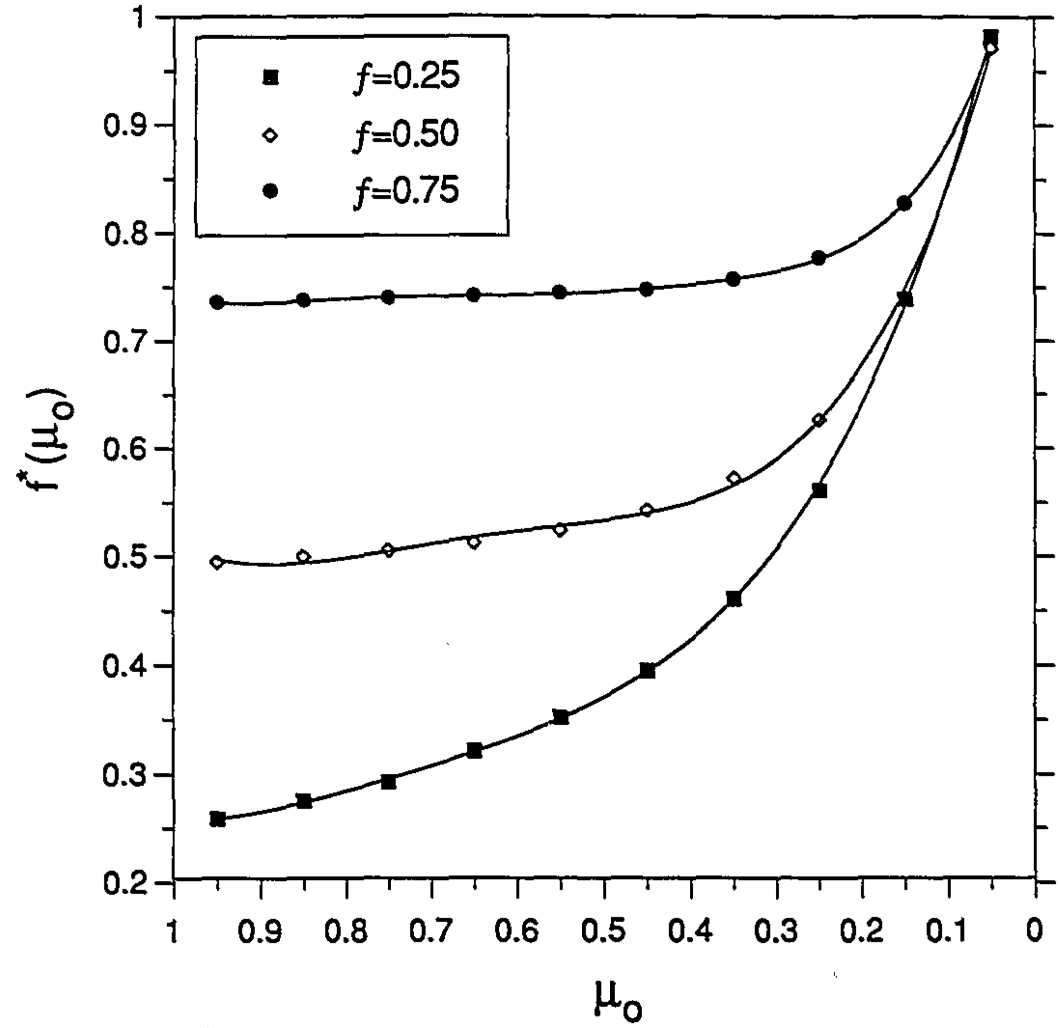

Figure 4.5 Cloud fraction as viewed from the solar direction (($f^*(\mu_o)$) for cloud fields with nadir cloud fraction f=0.25, f=0.50 and f=0.75.

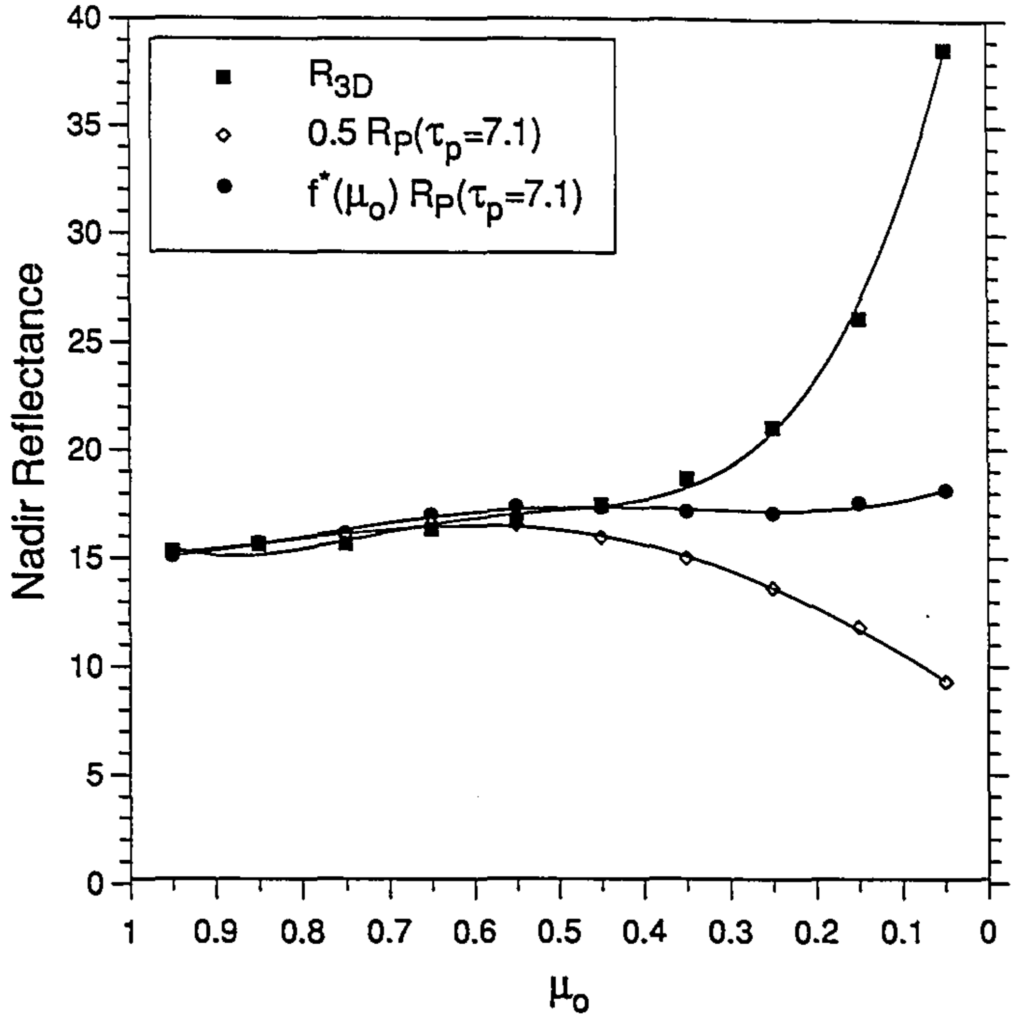

Figure 4.6 Comparison between the same curves plotted in Fig. 4.2 with a plane parallel result which accounts for the change in cloud fraction with μ_o ("$f^*(\mu_o)$ $R_P(\tau_p$=7.1)").

explain some of the discrepancy between 3D and 1D reflectances at small μ_0, it likely isn't the only cause.

This is not unexpected since, as was shown in Fig. 4.4, significant differences between 1D and 3D reflectances can also occur for overcast clouds, where no enhancement in cloud fraction occurs ($f^*(\mu_0)$=1 at all μ_0). Instead, differences in that case appeared to be most sensitive to the cloud top structure. From a modeling viewpoint, this is an extremely difficult feature to describe since it is highly variable from cloud to cloud (and even within one cloud for that matter). Further, it isn't clear what properties of cloud top structure are important.

One property which may prove to be important is the slope of illuminated cloud top surfaces. Since the angle of incidence of incoming solar radiation relative to a sloped surface is much different from that for a flat surface, this may substantially alter the reflected radiation upwards. However, since real clouds can be highly irregular in shape, many different cloud slopes are presented to the solar beam, making it difficult to study this effect directly.

To simplify the problem, it is useful to consider simple cloud geometries. Here we consider separate simulations for cloud fields consisting of isolated paraboloids, cones, and cylinders. The cloud fields are defined so as to ensure a constant cloud fraction of f=0.21 and an average cloud optical depth of $<\tau_c>$=10, so that the domain optical depth is held fixed at τ_d=2.1. By changing the gridpoint resolution r, while keeping the vertical size and cloud fraction constant, simulations are carried out for different aspect ratios α. For a cone, α is related to the slope (γ) of the surface through: $\gamma = \tan^{-1}(2\alpha)$, so that increasing α causes an increase in γ. For the cylinder, changes in α do not affect the slope of the cloud surface, but does affect the proportion of solar radiation illuminating the top and side of the cloud.

Fig. 4.7 shows nadir reflectances as a function of μ_o for α=0.05, 0.1, 0.2, 0.5 and 1.0 for an isolated cone (Fig. 4.7 (a)) and an isolated cylinder (Fig. 4.7 (b)), together with plane parallel calculations at τ_p=10 and f=0.21. At large μ_o, 3D reflectances tend to be smaller than the plane parallel values because of diffusive leakage through the cloud sides, which is most pronounced at large α. At μ_o=0.4-0.5, reflectances are similar for all α. This may be due to an increase in side illumination, especially at large α. At small μ_o, the reflectances are quite sensitive to α. For α=1, they remain fairly constant (Fig. 4.7 (a)), or decrease steadily (Fig. 4.7 (b)) with decreasing μ_o. A similar tendency is also observed at α=0.5 and α=0.2 for the cylinder case, although it is not as pronounced. This likely occurs because radiation can escape more readily through the antisolar side of clouds with large α, since the horizontal path length through these clouds is much shorter than for clouds with small α. When $\alpha \leq 0.2$, the strongest increase in reflectance occurs at small μ_o—a result which is qualitatively quite similar to the observational results in Fig. 2.5. While much of this increase can be attributed to enhancement in side illumination, this does not appear to be the only factor in explaining the differences here either. To illustrate, Fig. 4.8 provides ratios of reflectances from the cone field at α=0.2 to 1D reflectances which do not account for side illumination ("$R_{3D}/(f\ R_P)$"), together with ratios obtained when side illumination is included ("$R_{3D}/(f^*(\mu_o)\ R_P)$"). As shown, even though including the enhancement effect reduces the ratio by as much as a factor of 2 for μ_o=0.05, the cone reflectances are still larger than the 1D values by a factor of 1.7 at μ_o=0.05.

To examine how the slope of the cloud top affects the ratio when cloud enhancement is taken into account (i.e. when we consider the ratio $R_{3D}/(f^*(\mu_o)\ R_P)$), comparisons between the different cloud shapes were performed for various cloud aspect ratios. Figs. 4.9 (a) through (c) show $R_{3D}/(f^*(\mu_o)\ R_P)$) for a paraboloid, cone and cylinder at (τ_c=10), together with a second cylinder which is twice as thick (τ_c=20). These are plotted for α=0.05 (Fig. 4.9 (a)), α=0.1 (Fig. 4.9 (b)), and α=0.2 (Fig. 4.9 (c)). When the cloud fields

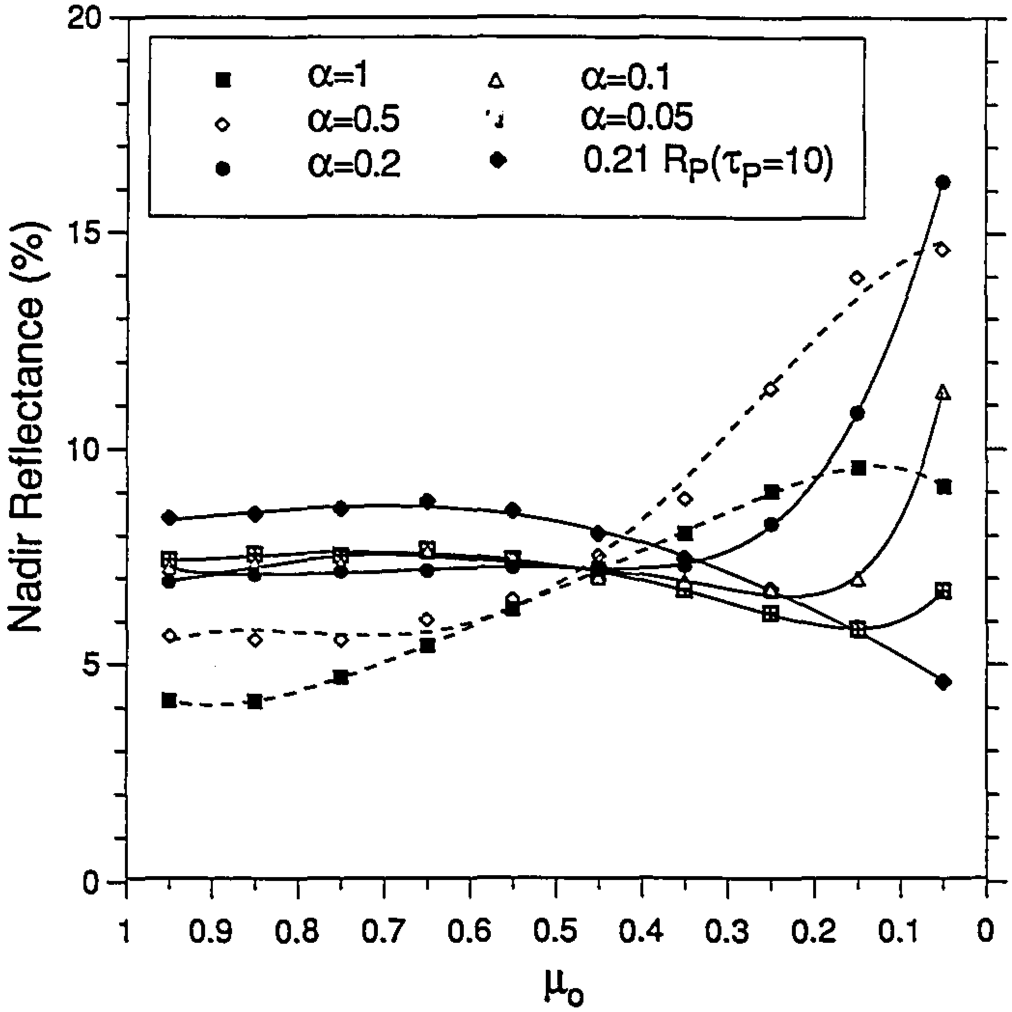

α=1
α=0.1
α=0.5
α=0.05
α=0.2
0.21 Rp(τp=10)
Nadir Reflectance (%)
20
15
10
5
0
1
0.9
0.8
0.7
0.6
0.5
0.4
0.3
0.2
0.1
0
μo

(a)

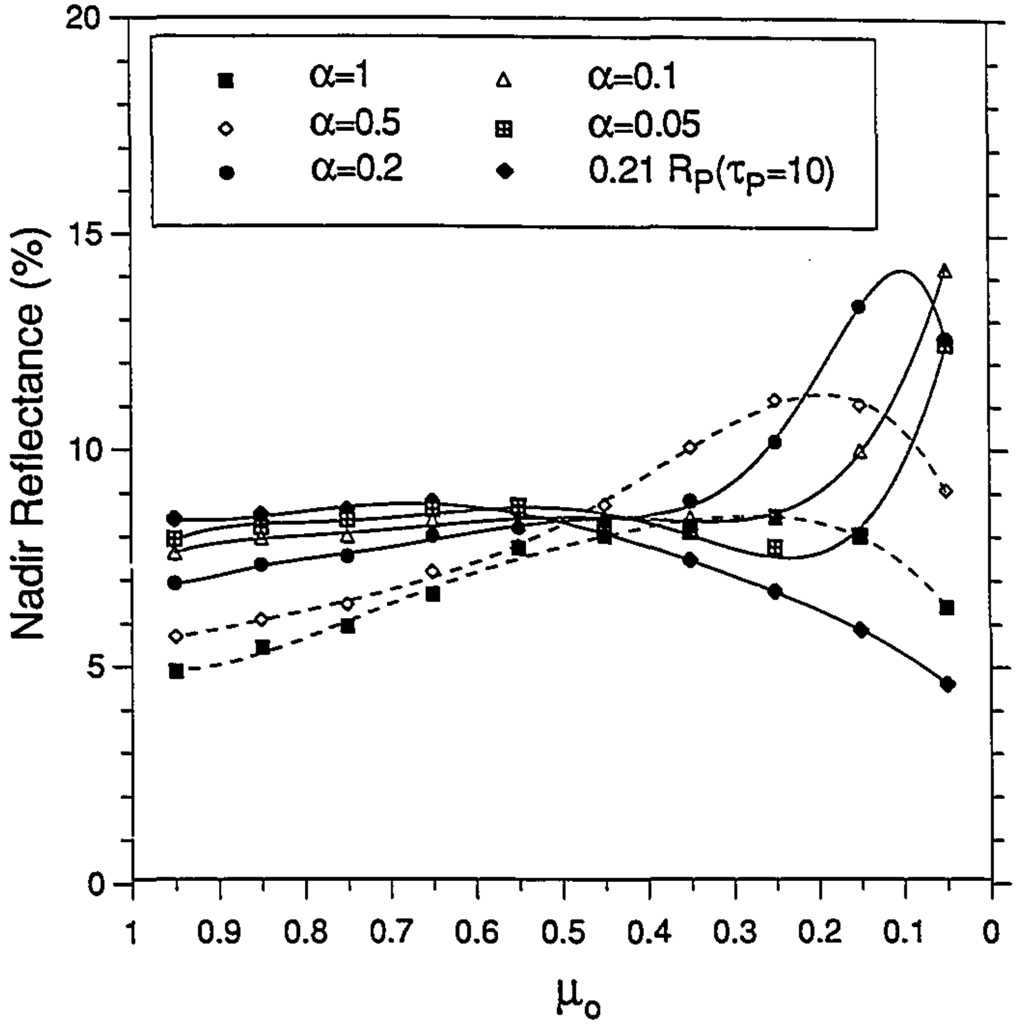

(b)

Figure 4.7 Nadir reflectances as a function of μ_0 for (a) an isolated cone and (b) an isolated cylinder at aspect ratios α=0.05, 0.1, 0.2, 0.5 and 1.0, together with plane parallel results at τ_p=10 and f=0.21.

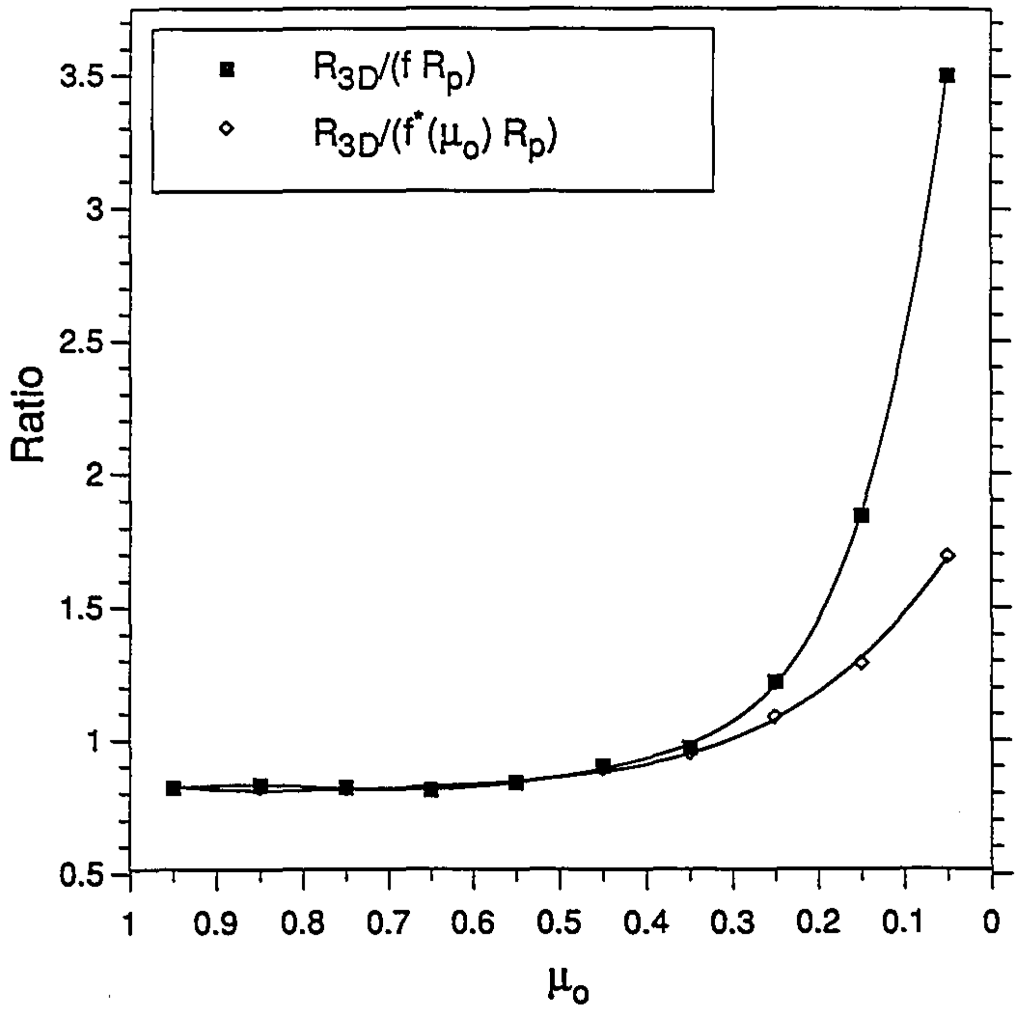

Figure 4.8 Ratios of reflectances from the cone field at α=0.2 to 1D reflectances which do not account for side illumination ("$R_{3D}/(f\ R_P)$"), together with ratios obtained when side illumination is included ("$R_{3D}/(f^*(\mu_o)\ R_P)$")

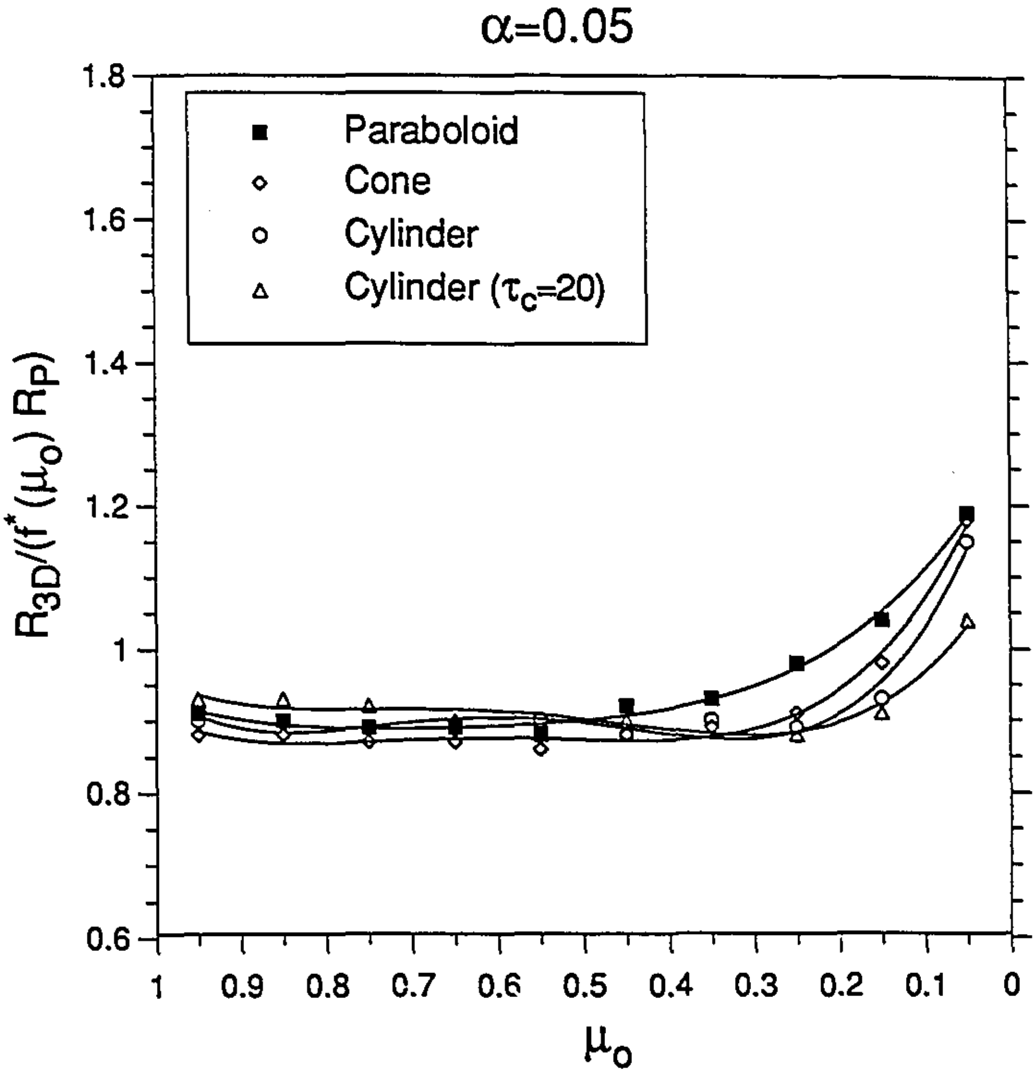
α=0.05
Paraboloid
Cone
Cylinder
Cylinder (τ_c=20)
$R_{3D}/(f^*(\mu_o)\,R_P)$
μ_o
1.8
1.6
1.4
1.2
1
0.8
0.6
1 0.9 0.8 0.7 0.6 0.5 0.4 0.3 0.2 0.1 0

(a)

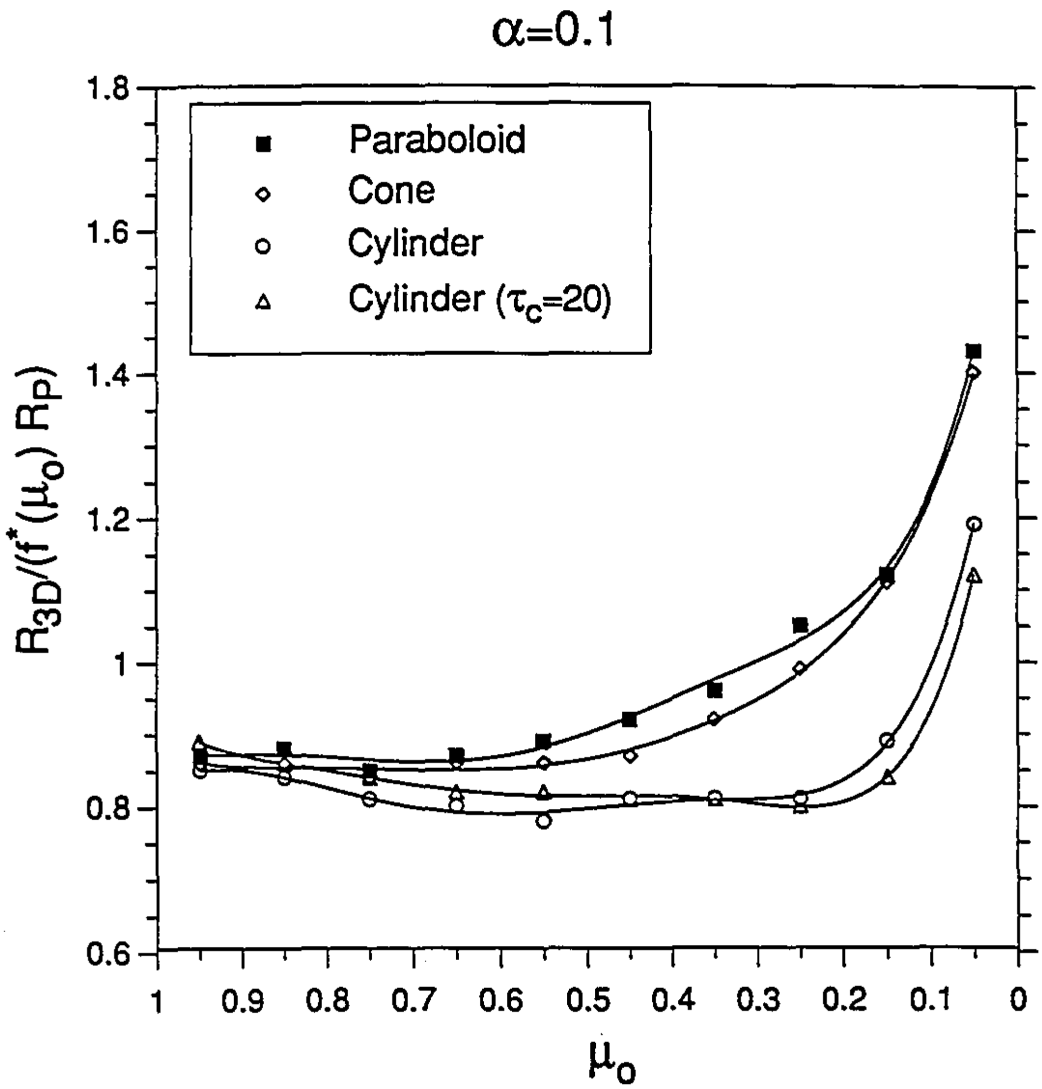

α=0.1
Paraboloid
Cone
Cylinder
Cylinder (τc=20)
R3D/(f*(μo) Rp)
μo
1.8
1.6
1.4
1.2
1
0.8
0.6
1
0.9
0.8
0.7
0.6
0.5
0.4
0.3
0.2
0.1
0

(b)

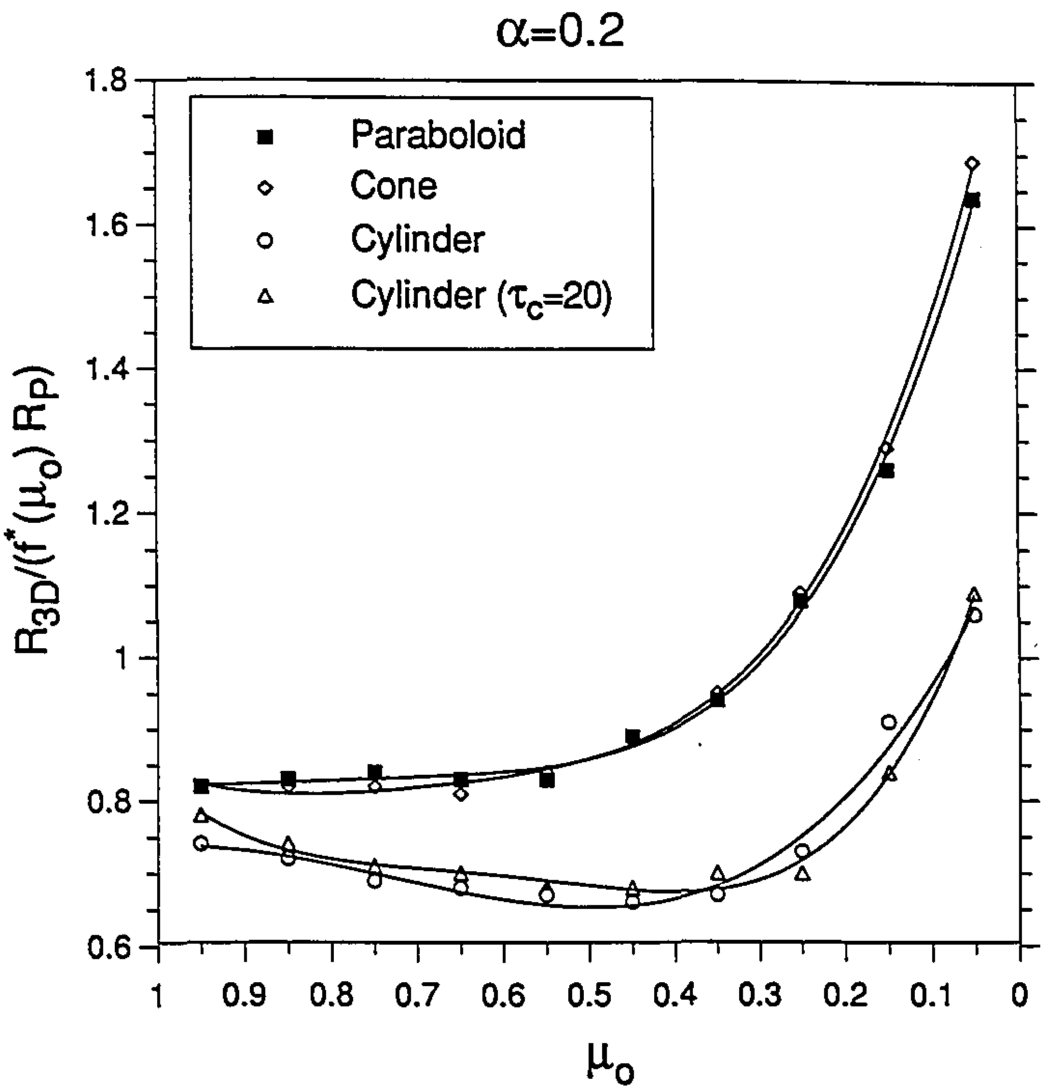

(c)

Figure 4.9 $R_{3D}/(f^*(\mu_o)\ R_P)$ vs μ_o for various cloud geometries at (a) α=0.05, (b) α=0.1, and (c) α=0.2.

are relatively flat (α=0.05), Fig. 4.9 (a) shows that only a modest increase in the ratio occurs with decreasing μ_0 for all surfaces. As α increases, however, ratios for surfaces which are sloped (paraboloid and cone) increase substantially, while those for the cylinders remain fairly constant. Since only cloud slope varies with α for the cone and paraboloid, while there is no such change for the cylinders, these results suggest that the slope of a surface may also be an important factor in explaining the differences between 3D and 1D reflectances.

While a rigorous correction for the slope effect in realistic cloud fields is beyond the scope of this study, an experiment was nonetheless carried out to explore one possible approach for the simple cloud geometries as a starting point. Consider a sloped surface inclined at an angle γ relative to the horizontal plane, with solar illumination at θ_0 ($= cos^{-1} \mu_o$) and an observer at nadir, as illustrated in Fig. 4.10. Relative to the sloped surface facing the sun, the angle of incidence becomes $\theta_o' = \theta_o - \gamma$, while the observer view angle is $\theta' = \gamma$, and the relative azimuth about the normal to the surface (z') is given by the angle ϕ'. If we now assume that a surface such as a cone can be approximated by a plane inclined at an angle equal to slope of the cone, the plane parallel model can then be used to generate reflectances at θ_o', θ' and ϕ' and, provided enhancement due to side illumination of the cone is taken into account, these can be compared with the cone reflectances. As a further simplification, since a cone is azimuthally symmetric and its slope does not vary over its surface, reflectances from the plane surface can be averaged over ϕ' in the forward scattering direction ($0° \leq \phi' \leq 90°$; $270° \leq \phi' \leq 360°$) for θ_o-γ>0°, and over the backscattering direction ($90° \leq \phi' \leq 180°$) for θ_o-γ<0°.

Fig. 4.11 (a) through (d) compares reflectances from an isolated cone ("R_{3D}") at α=0.05 (γ=5.7°), α=0.1 (γ=11.3°), α=0.2 (γ=21.8°), and α=0.5 (γ=45°), respectively, with plane parallel calculations (at τ_p=10) which do not account for the slope effect ("0.21 Rp"

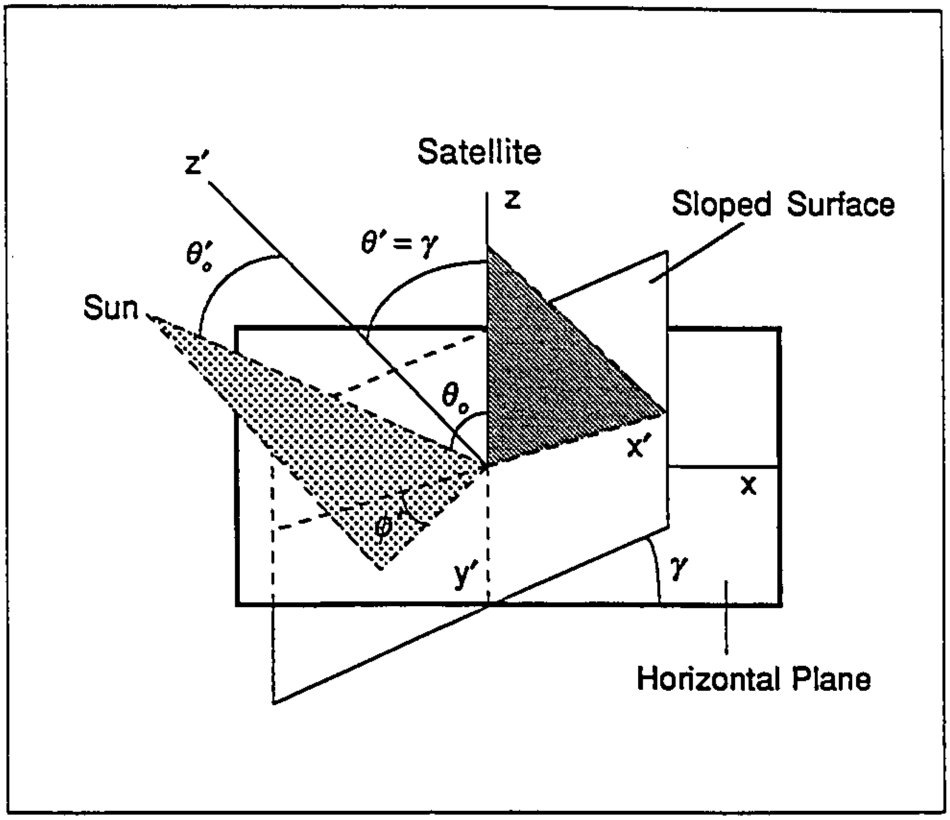

Figure 4.10 Schematic illustrating incident and observer angles relative to a sloped surface inclined at an angle γ relative to the horizontal plane.

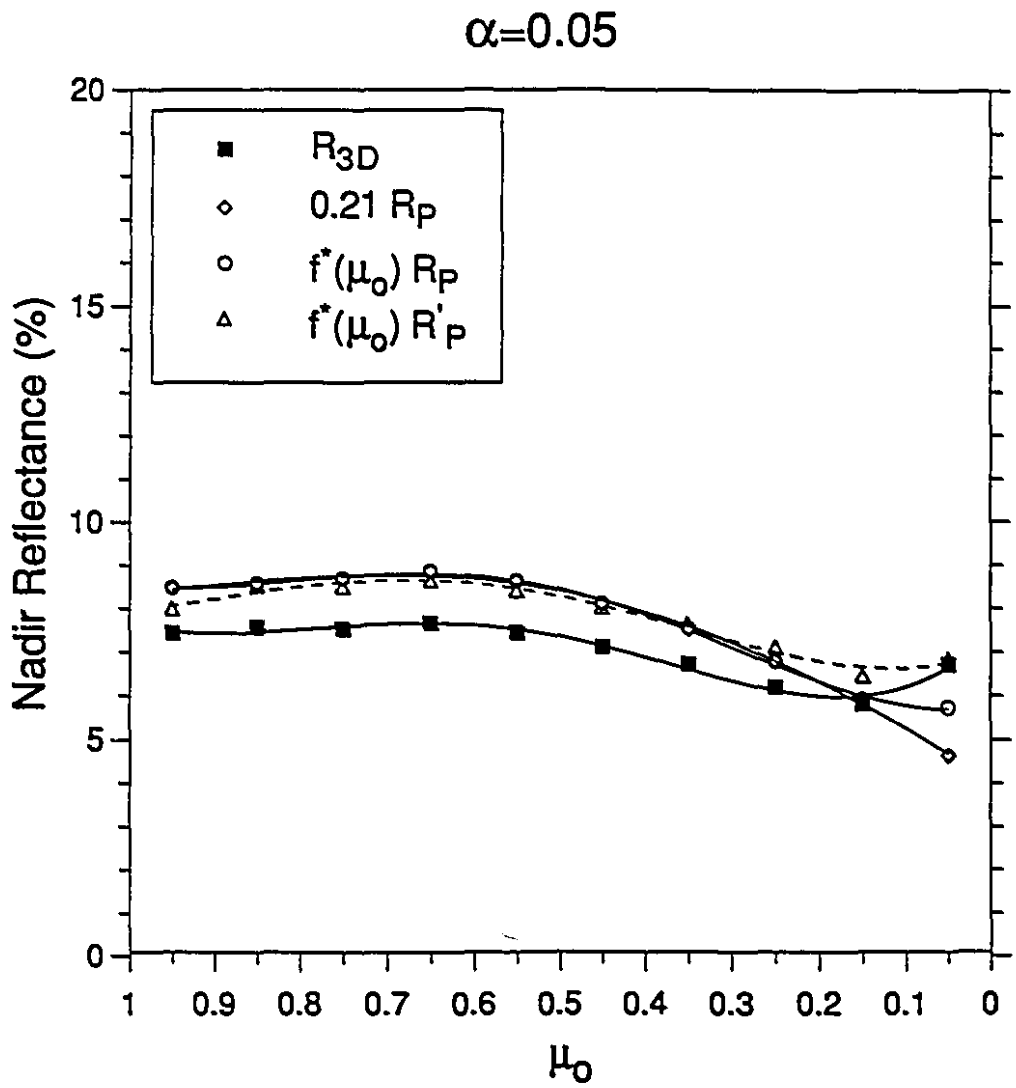
α=0.05
20
15
10
5
0
Nadir Reflectance (%)
R_{3D}
0.21 R_P
$f^*(\mu_o)$ R_P
$f^*(\mu_o)$ R'_P
1
0.9
0.8
0.7
0.6
0.5
0.4
0.3
0.2
0.1
0
μ_o

(a)

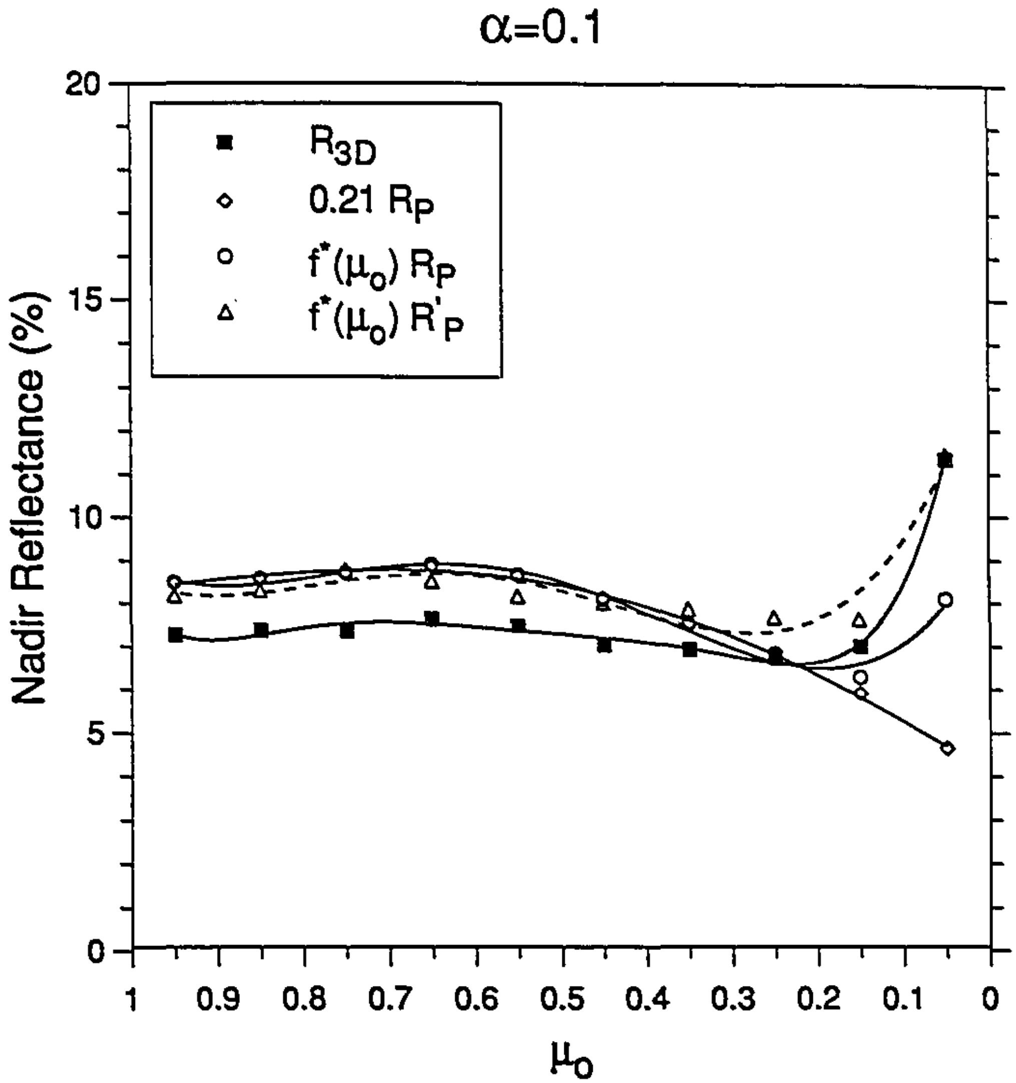
α=0.1
R_{3D}
$0.21\ R_P$
$f^*(\mu_o)\ R_P$
$f^*(\mu_o)\ R'_P$
Nadir Reflectance (%)
20
15
10
5
0
1
0.9
0.8
0.7
0.6
0.5
0.4
0.3
0.2
0.1
0
μ_o

(b)

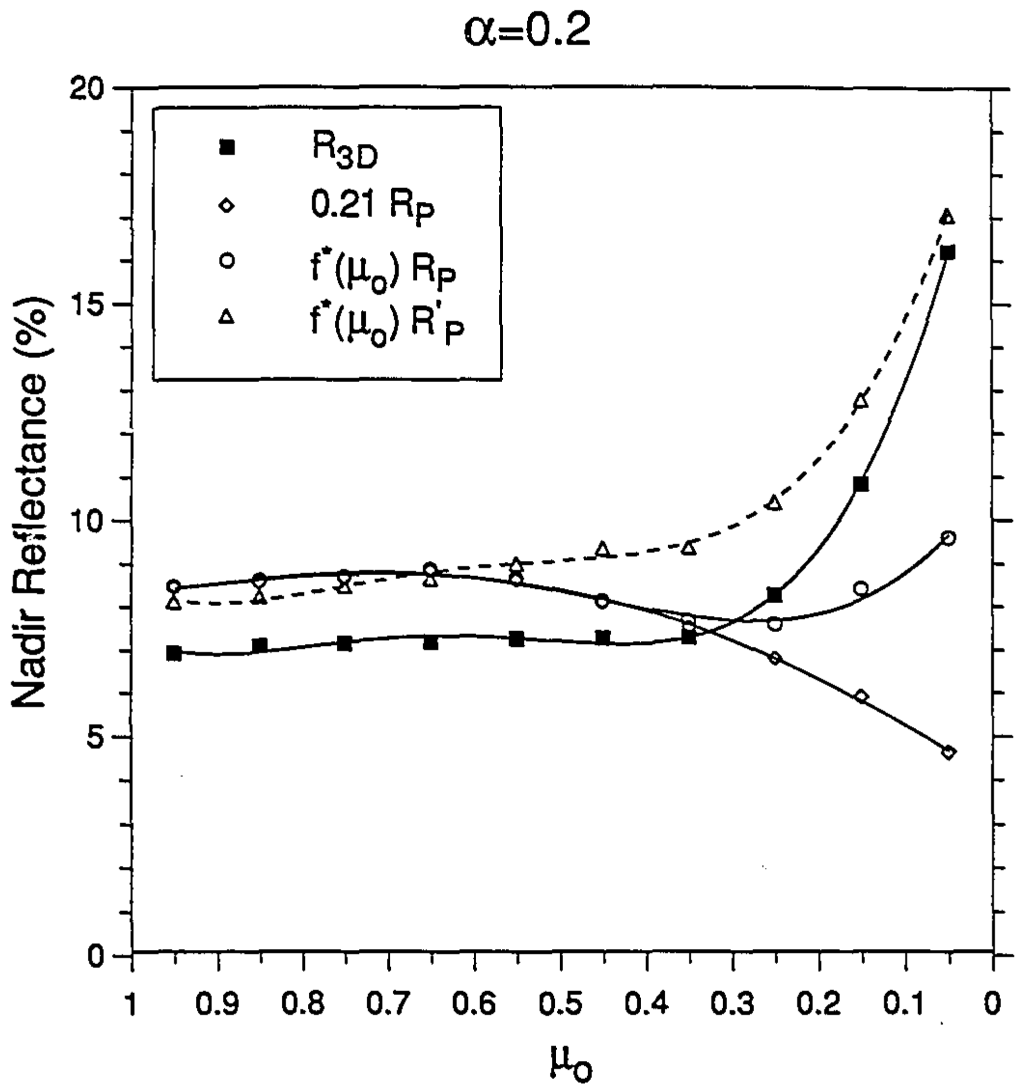
α=0.2
20
15
10
5
0
Nadir Reflectance (%)
R3D
0.21 RP
f*(μo) RP
f*(μo) R'P
1
0.9
0.8
0.7
0.6
0.5
0.4
0.3
0.2
0.1
0
μo

(c)

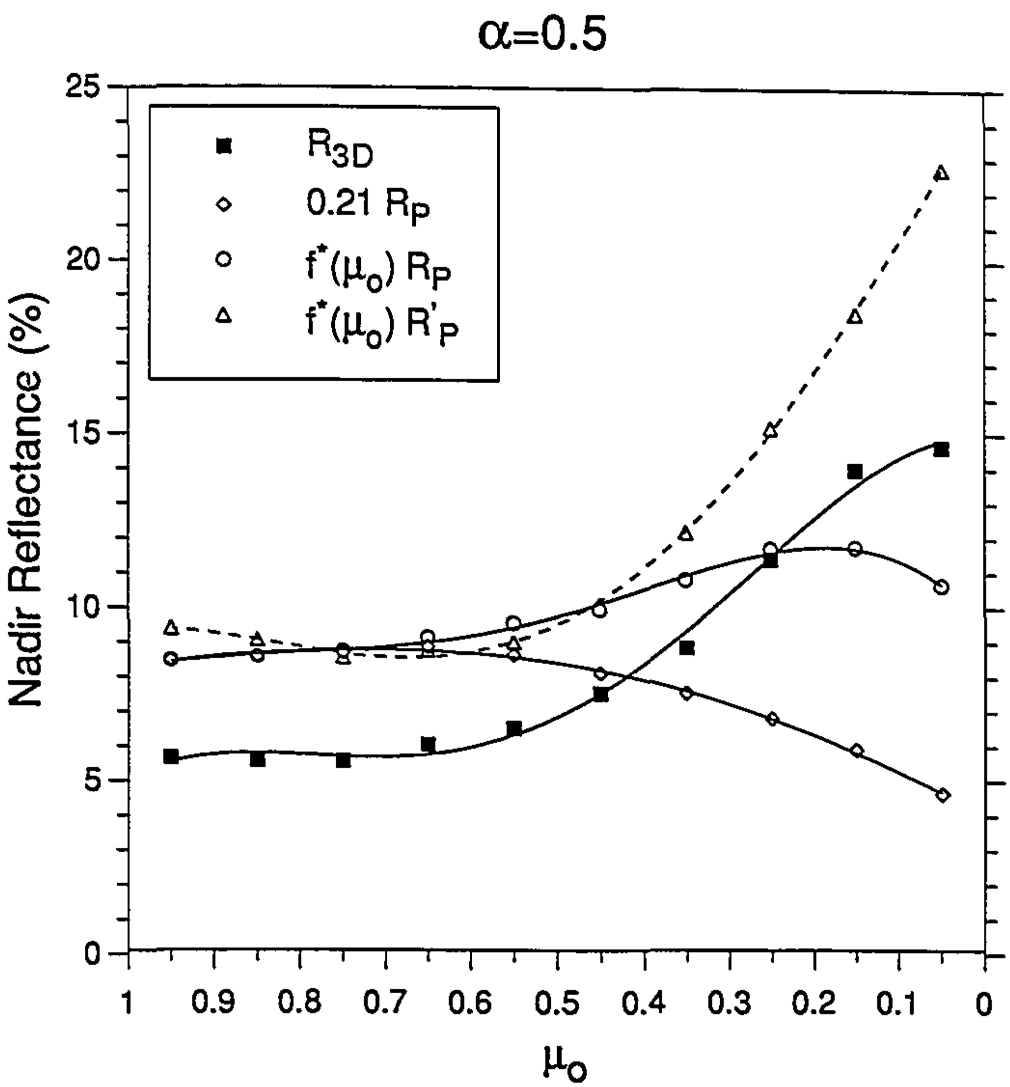

(d)

Figure 4.11 Isolated cone reflectances ("R_{3D}") together with various plane parallel calculations for (a) α=0.05 (γ=5.7°), (b) α=0.1 (γ=11.3°), (c) α=0.2 (γ=21.8°), and (d) α=0.5 (γ=45°). R'_P is obtained using incident and observer angles relative to the sloped surface.

and "$f^*(\mu_o)$ R_P"), and an approximation that takes both slope and enhancement due to cloud side illumination into account ("$f^*(\mu_o)$ R'_P"). While the sloped plane approximation isn't perfect, it does however appear to capture at least the gross features in the 3D reflectances. For example, as α gets larger, both "R_{3D}" and "$f^*(\mu_o)$ R'_P" show a progressively stronger increase with decreasing μ_o. For α<0.5 (Figs. 4.11 (a) through (c)), the largest discrepancies now appear to occur at larger values of μ_o, while the differences actually get smaller as the sun becomes more oblique. Clearly this is a substantial improvement over the assumptions which ignore the slope effect (e.g. "$f^*(\mu_o)$ R_P"). Large differences at sun angles closer to zenith are expected since no account of diffusive leakage through the clouds are assumed in the approximations. For α=0.5, the differences between 3D cloud reflectances and those for the "$f^*(\mu_o)$ R'_P" case at small μ_o are likely caused by diffusive leakage through the antisolar side of the 3D clouds due to a shorter horizontal path length through these clouds. If this did not occur, "R_{3D}" would likely increase with decreasing μ_o in a manner similar to that for the "$f^*(\mu_o)$ R'_P" case.

While these ideas appear to work reasonably well for simple cloud geometries, clearly a much more rigorous analysis is required to establish their validity for real cloud fields. In that case, some means of inferring the slope and orientation of the cloud top surfaces would be required. Also, the effect of side illumination would have to be included, as would the influence of side leakage through the cloud sides (especially at large μ_o). While this would be difficult to do using actual satellite observations, it may be feasible using Monte Carlo simulations of stochastic 3D cloud fields. In fact, it may even be possible to develop simple parameterizations to remove the cloud optical depth bias described in Chapter 2.

4.3.2 View Angle Dependence

Monte Carlo simulations can also be performed to examine whether 3D effects can explain some of the results obtained in Chapter 3 as well. In that chapter, mean observed reflectances exceeded plane parallel values in the backscattering direction by roughly a constant amount at all μ at oblique sun angles, despite marked differences in the frequency distributions. In the forward scattering direction, while observed reflectances generally fell within the range of plane parallel model values, the observations did show a very different μ dependence—observed reflectances appeared to level off between μ=0.5 and μ=0.3, whereas the calculations showed a steady increase.

To examine these differences, simulations using the cloud field in Fig. 4.1 were generated over the same ϕ intervals as in Chapter 3 (i.e. $30°<\phi<60°$; $120°<\phi<180°$). Fig. 4.12 (a) and (b) show 3D reflectances as a function of μ for μ_0=0.9-1.0 (Fig. 4.12 (a)) and μ_0=0.1-0.2 (Fig. 4.12 (b)) for gridpoint resolutions r=68 m, r=137 m and r=275 m. Changing r is equivalent to changing the aspect ratio of the cloud elements since only the horizontal dimension of the entire cloud field is affected. Plane parallel calculations ("0.5 $R_p(\tau_p$=7.6)") in these figures are normalized at nadir using the 3D reflectances at μ_0=0.9-1.0 (a τ_p=7.6 provided the best match for these cases).

In Fig. 4.12 (a), the 3D reflectances are shown to be relatively insensitive to r, and the plane parallel reflectances show a similar dependence on μ as the 3D results. In contrast, at μ_0=0.1-0.2, a rather large dependence on r is observed, and differences between 3D and 1D reflectances tend to be much larger than for zenith sun. In the backscattering direction, 3D reflectances are larger than the 1D values. This is consistent with the observational results in Chapter 3 as well as with Monte Carlo studies in the literature (e.g. Davies, 1984; Bréon, 1992; Kobayashi, 1993), and is attributable to scattering by the cloud sides. When r is small (high aspect ratio), differences between the 3D and 1D reflectances appear to increase with decreasing μ. As r is decreased (i.e. as aspect ratio decreases), this μ dependence decreases substantially. Thus, the lack of a μ dependence in the differences between the observations and plane parallel reflectances in Chapter 3 only appears in Monte Carlo simulations for clouds of relatively low aspect ratio.

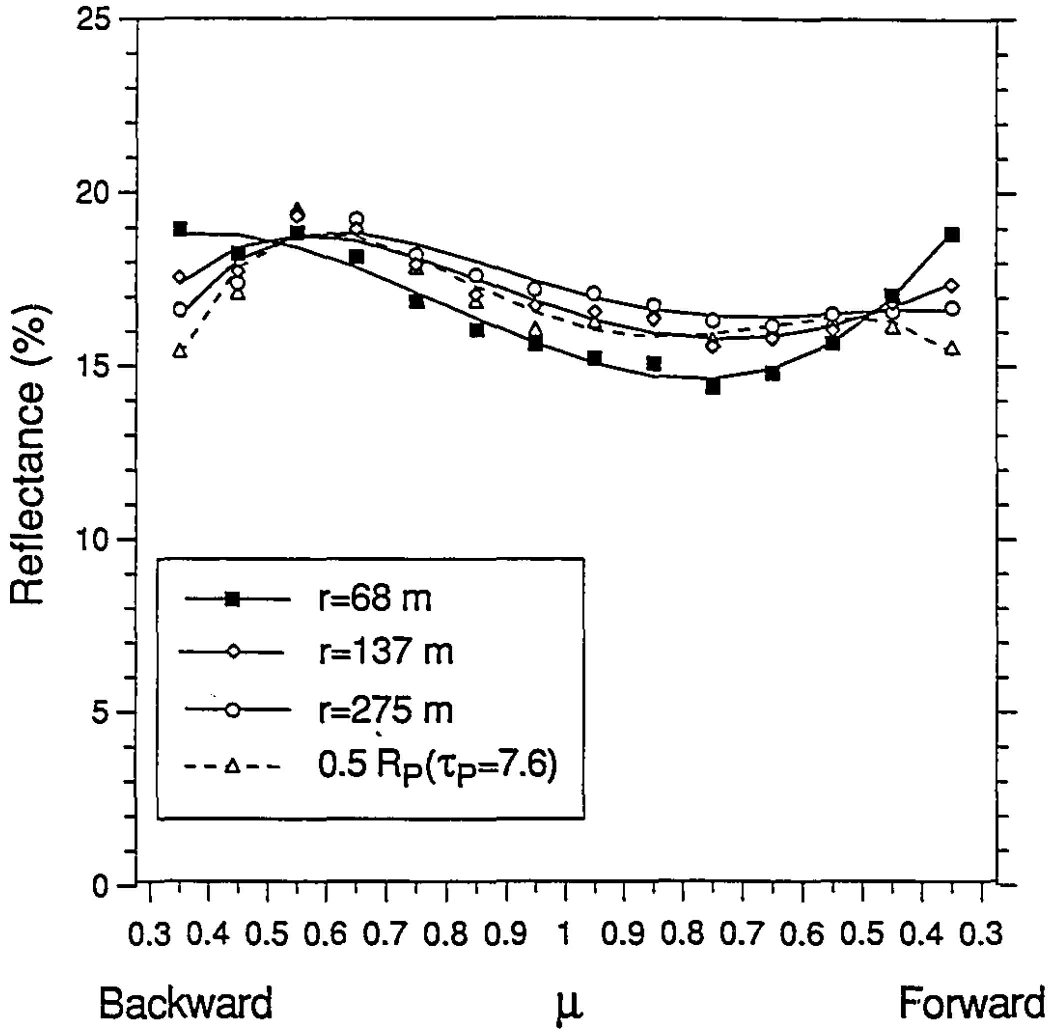
25
20
15
10
5
0
Reflectance (%)
r=68 m
r=137 m
r=275 m
0.5 R_P(τ_P=7.6)
0.3 0.4 0.5 0.6 0.7 0.8 0.9 1 0.9 0.8 0.7 0.6 0.5 0.4 0.3
Backward
μ
Forward

(a)

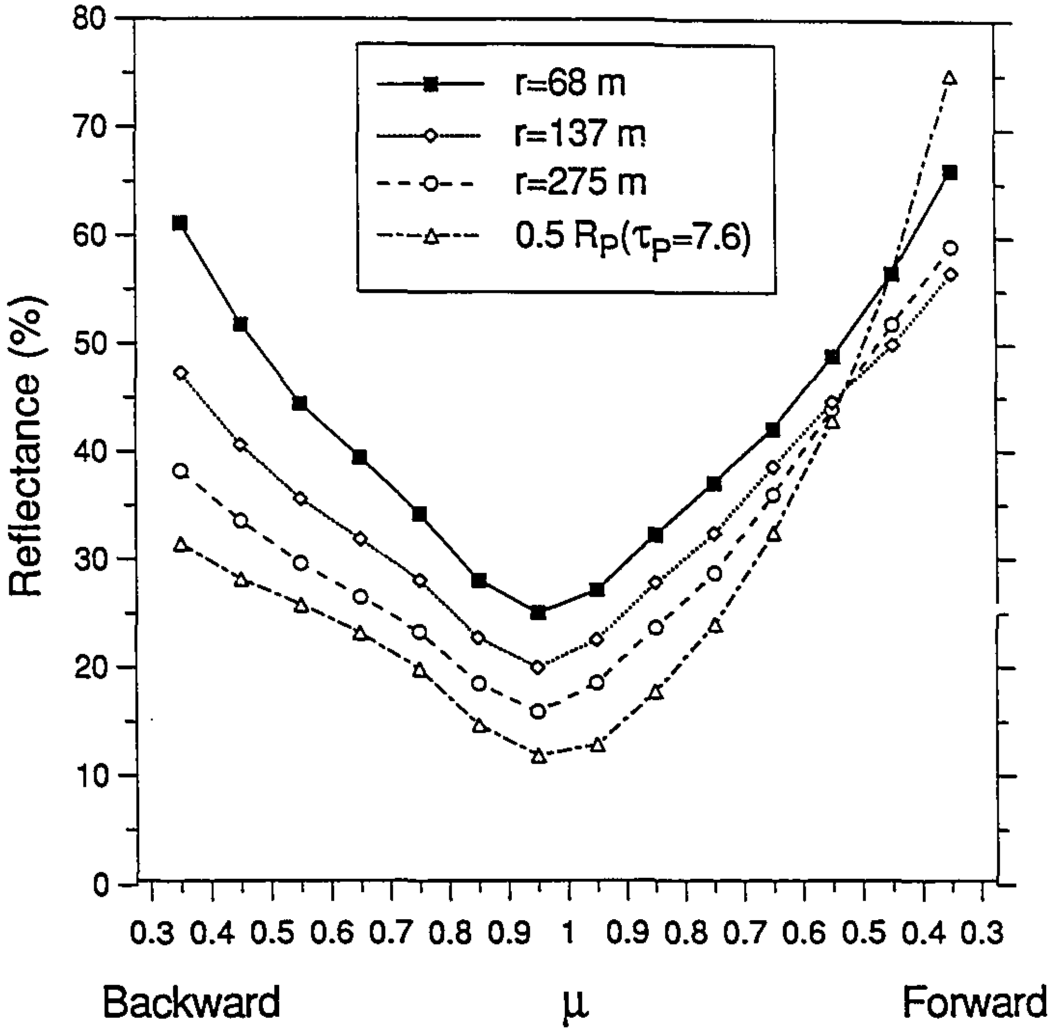

(b)

Figure 4.12 3D reflectances as a function of μ at (a) μ_0=0.9-1.0 and (b) μ_0=0.1-0.2 for various gridpoint resolutions (r) in the backward (120°<φ<180°) and forward (30°<φ<60°) scattering directions, together with normalized plane parallel calculations ("0.5 $R_P(\tau_P=7.6)$").

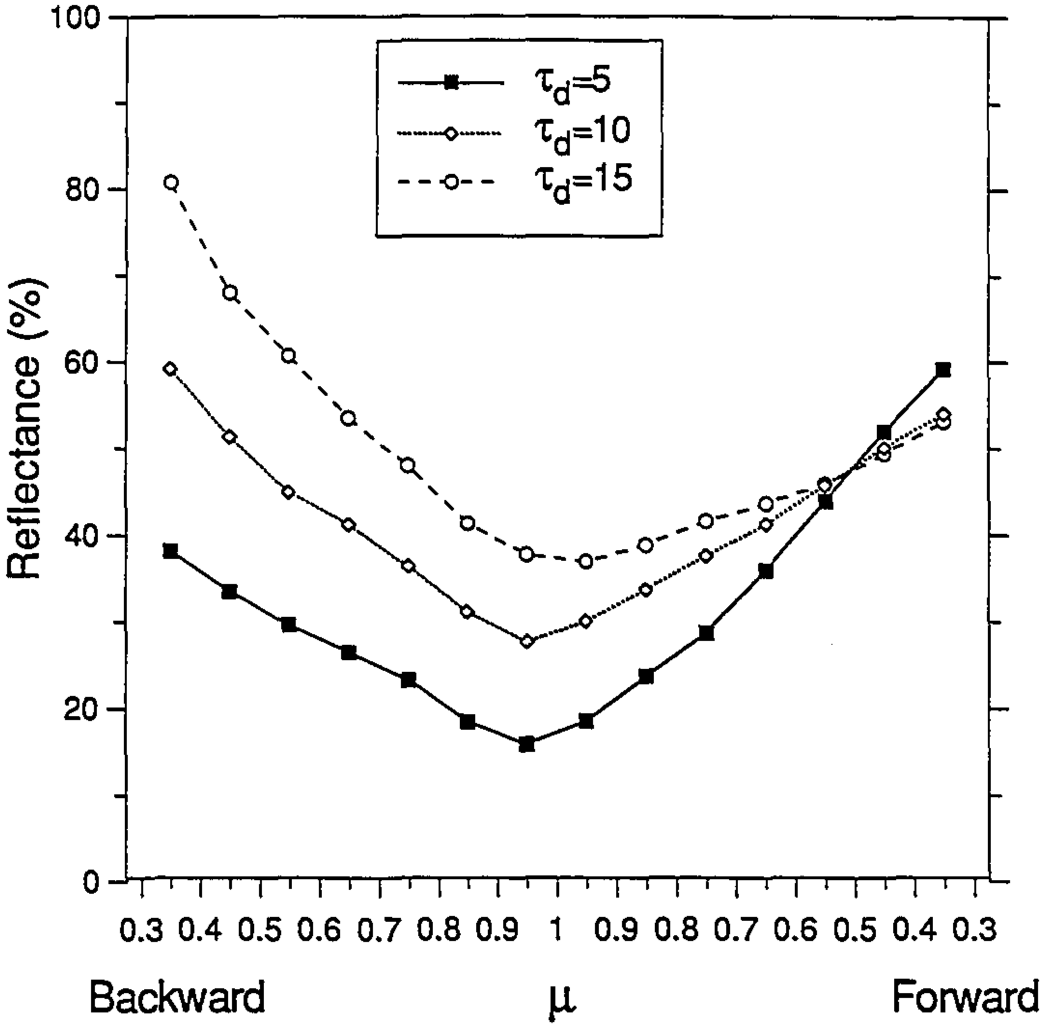

100
80
60
40
20
0
Reflectance (%)
τ_d=5
τ_d=10
τ_d=15
0.3 0.4 0.5 0.6 0.7 0.8 0.9 1 0.9 0.8 0.7 0.6 0.5 0.4 0.3
Backward
μ
Forward

(a)

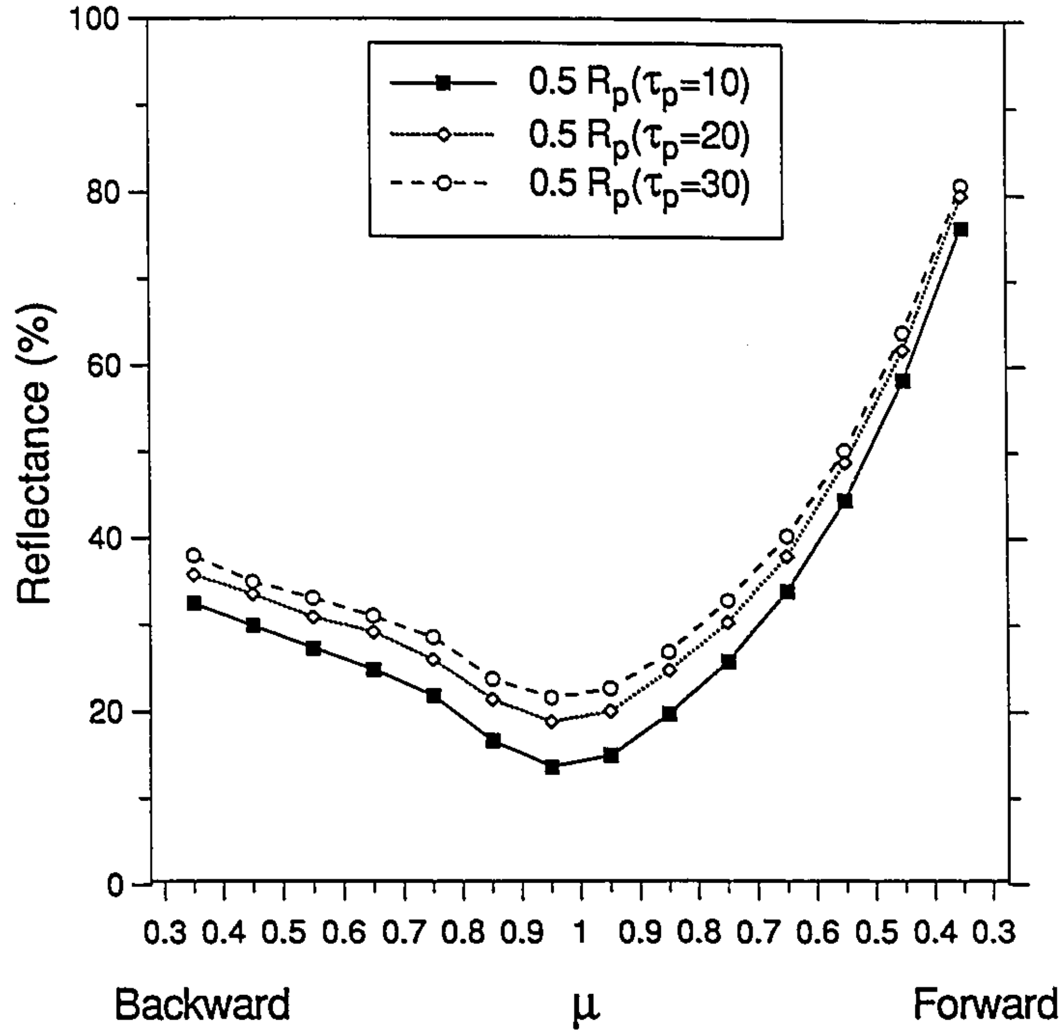

(b)

Figure 4.13 (a) 3D and (b) plane parallel reflectances as a function of μ for f=0.5, r =275 m, τ_d=5, 10 and 15, at μ_0=0.1-0.2.

In the forward scattering direction, the 3D reflectances show a similar difference from the 1D results as do the observations. In both Fig. 4.12 (b) and Fig. 3.3 (a), plane parallel reflectances show a much stronger dependence on μ than either the observations or the 3D calculations. The 3D reflectances do not appear to level off as strongly at small μ as the observations, however. This may be due to the fact that the observations are actually averages over many different cloud optical depths while the 3D reflectances were determined using a much smaller range (i.e. those which occur within the one cloud field considered). To examine the sensitivity to cloud optical depth in the 3D case, Fig. 4.13 (a) shows 3D reflectances for r =275 m, f=0.5 and τ_d=5, 10 and 15. In the forward direction, reflectances from thicker clouds tend to level off much more rapidly with decreasing μ than do those from thinner clouds. In contrast, plane parallel reflectances show a very different result. Fig. 4.13 (b) shows plane parallel calculations as a function of μ for three different cloud optical depths which correspond to each of the curves in Fig. 4.13 (a) (for f=0.5). In this case, the reflectances show a strong increase with decreasing μ in the forward direction, regardless of cloud optical depth. Physically, the reason for these differences is likely due to diffusive leakage through the 3D cloud sides—as the clouds become thicker, a larger proportion of the radiation exits through the antisolar side of the clouds at oblique view angles, resulting in a weaker μ dependence for those clouds. Thus, the tendency for the observed reflectances to level off at small μ in the forward scattering direction is consistent with 3D behavior.

4.4 Summary

This chapter has shown that many of the differences between the observations and plane parallel calculations obtained in Chapters 2 and 3 can be qualitatively explained by the influence of 3D cloud effects. At nadir, 3D clouds show the same dependence on μ_0 as the observations, a result which occurs not only for broken 3D cloud fields but can also occur in overcast conditions (provided the cloud tops are sufficiently "bumpy"). This dependence was shown to be highly sensitive to the influence of cloud side illumination and to the slope of the illuminated cloud top surfaces. Accounting for both of these effects in the plane parallel calculations was shown to significantly reduce reflectance differences at low sun elevations between 1D and 3D calculations when simple cloud geometries were considered. When the μ dependence between 3D and 1D reflectances were compared, differences were also qualitatively consistent with observational results. Differences tended to be small at high sun elevations (provided the plane parallel calculations were normalized at nadir), and increased with solar zenith angle. While the observational results in Chapter 3 showed the differences to be largely independent of μ in the backscattering direction, this was only observed in 3D calculations for clouds having relatively low aspect ratios. In the forward direction, the tendency for observed reflectances to level off at small μ was also found in the 3D cloud simulations.

Chapter 5

Summary and Conclusions

The purpose of this study has been to assess the performance of plane parallel radiative transfer theory in the analysis of satellite scanner measurements, and to examine what role 3D effects may have in explaining any differences. One year of ERBS scanner shortwave reflectance measurements were directly compared with plane parallel model calculations under different Sun-Earth-satellite viewing configurations. Then, based on Monte Carlo simulations involving 3D cloud fields, it was shown that many of the differences between the observations and plane parallel calculations can be qualitatively explained by 3D cloud effects.

5.1 Solar Zenith Angle Dependence

When matched to observations on a pixel-by-pixel basis (accounting for cloud fraction, curvature effects, and atmospheric effects above and below the cloud), plane parallel theory retrieves cloud optical depths that show a systematic increase with solar zenith angle. In the limit of large solar zenith angle, the retrieved optical depths become extremely large. On average, the largest increases occurred for $\mu_0 \lesssim 0.45$ when sub-pixel cloud fraction was taken into account. When cloud optical depths were analyzed for different classes of occurrence (deduced by calculating the mean over different percentile intervals), the μ_0 dependence in the cloud optical depth was also found to be sensitive to cloud optical depth. For thin clouds (optical depths $\lesssim 6$), this dependence tended to be strong only at oblique sun angles. For thicker clouds, the μ_0 dependence was much larger in general and was no longer restricted to small μ_0. In fact, for classes with clouds of optical depth greater than $\approx$12 at high sun, this dependence on μ_0 occurred for all solar zenith angles. This was observed for the thickest 10% of the clouds for the inhomogeneous approximation, and the thickest 1% for the homogeneous pixel approximation.

The absence of strong, systematic, diurnal and latitudinal effects in the observations, together with the high degree of statistical confidence from this very large data set, leads to the conclusion that direct use of the plane parallel approach for retrieving cloud optical depth from nadir reflectance is fundamentally flawed for thin clouds at low sun elevations and for thick clouds in general. That is, because plane parallel nadir reflectances decrease with decreasing μ_0 for a given cloud optical depth, while, on average, observed reflectances show the opposite behavior, plane parallel cloud optical depths inferred from low resolution satellite measurements suffer from a systematic solar zenith angle dependent bias. As a minimum requirement, application of 1D theory to the remote sensing of cloud optical thickness from measurements at nadir should therefore be restricted to thin clouds and small solar zenith angles.

The overall (relative) uncertainty in average reflectance due to the μ_0 bias in cloud optical depth was estimated to be less than 10% for $\mu_0>0.6$, and as large as 30% at very oblique sun angles. While the uncertainty in the nadir reflectance was generally small when the reflectance was low, it still exceeded 10% for $\mu_0<0.45$ for the thinnest 50% of the clouds, and tended to increase substantially for brighter clouds. For example, relative uncertainties in reflectance for the brightest 50% of the cases could be as high as 37%, while uncertainties as high as 50% were observed for the brightest 1% of the cases.

5.2 View and Relative Azimuth Angle Dependence

On average, differences between observed and plane parallel reflectances were found to be less sensitive to changes in μ and ϕ than to μ_0. At moderate to high sun elevations ($\mu_0>0.4$), the μ dependence from plane parallel theory was consistent with results from observations. For more oblique sun angles, observed reflectances tended to exceed those generated by the plane parallel model in the backscattering direction, with (absolute) differences ranging from less than 2% at intermediate μ_o to as much as 10% at the most oblique sun angles. Provided the atmosphere above the cloud was accounted for in the backscattering direction, no systematic μ dependence in the differences was observed on average. When stratified by pixel brightness (or cloud thickness), however, reflectances at oblique view angles showed a different result from that at nadir: reflectance differences were not sensitive to cloud thickness. Relative differences were generally $\leq 5\%$ at oblique view angles for $\mu_o>0.45$, and $\leq 20\%$ at smaller μ_o. In the forward scattering direction, plane parallel model reflectances were more sensitive to the model assumptions (such as cloud top height, sub-pixel cloud fraction), and consequently, observed reflectances generally fell within the range of plane parallel model values. Despite this, the observations and plane parallel calculations did behave differently at small μ—observed reflectances were shown to level off between μ=0.5 and μ=0.3, whereas the calculations increased steadily. When the observed and plane parallel reflectances were compared as a function of relative azimuth angle, the plane parallel model results showed a very similar dependence as the observations. Neglecting pixel area expansion with view angle in the calculations was shown to have only a minor influence in these comparisons.

When the observations were examined for consistency with the principle of directional reciprocity, a large discrepancy was observed due mainly to systematic differences in the μ_o dependence of the observed reflectance field compared to 1-D theory.

5.3 3D Effects

Overall, differences between the observations and plane parallel calculations were found to be qualitatively consistent with what comparisons between 3D and 1D simulations showed. When nadir reflectances from 3D cloud fields were examined as a function of μ_o, they tended to increase with decreasing μ_o, in a manner consistent with the observations. This behavior was not restricted only to broken cloud fields, but even occurred for overcast 3D cloud fields, provided the cloud tops were sufficiently inhomogeneous (or "bumpy").

While much of the discrepancy between 3D and 1D reflectances could be attributed to the influence of enhanced illumination of the 3D cloud sides for $f<1$, this did not appear to be the only cause. It was argued that an additional factor, associated with the slope of the illuminated cloud top surfaces, may also be important. To illustrate the importance of this effect, reflectances from simple cloud geometries (e.g. isolated cones, paraboloids and cylinders) were generated and compared with 1D results. It was shown that the departure from 1D behavior tended to increase as the slope of the illuminated cloud top surfaces was increased. When plane parallel calculations were modified to account for both slope and side illumination effects (in an approximate manner), a marked improvement in the results was observed at oblique sun angles. Closer to zenith, differences were attributed to diffusive leakage effects not accounted for in the modified 1D calculations. While these approximations were shown to provide reasonable results for simple cloud shapes, it is acknowledged that a much more rigorous approach would be required in the analysis of real cloud fields.

When the μ dependence between 3D and 1D reflectances were compared, the results were qualitatively consistent with the observational results in general. Reflectance differences tended to be small at high solar elevations (provided the plane parallel calculations were normalized at nadir), and much larger at oblique sun angles. At low sun, 3D reflectances were larger than the 1D values in the backscattering direction. However, while differences between observed and 1D reflectances were largely independent of μ in the backscattering direction, this was only observed for 3D clouds of low aspect ratio in the model comparisons. In the forward scattering direction, the tendency for observed reflectances to level off at small μ was also observed in the 3D cloud simulations.

Chapter 6

Bibliography

Aida, M. A., 1977: Scattering of solar radiation as a function of cloud dimension and orientation. *J. Quant. Spectrosc. Radiat. Transfer.*, **17**, 303-310.

Arking, A., 1964: Latitudinal distribution of cloud cover from TIROS III photographs, *Science*, **143**, 569-572.

Arking, A., and J.D. Childs, 1985: Retrieval of cloud cover parameters from multispectral satellite measurements. *J. Climate Appl. Meteor.*, **24**, 322-333.

Baldwin, D.G., and J.A. Coakley, Jr., 1991: Consistency of Earth radiation budget experiment bidirectional models and the observed anisotropy of reflected sunlight, *J. Geophys. Res.*, **96**, 5195-5207.

Barker, H.W., and J.A. Davies, 1992: Solar radiative fluxes for stochastic, scale-invariant broken cloud fields. *J. Atmos. Sci.*, **49**, 1115-1126.

Barkstrom, B., E. Harrison, G. Smith, R. Green, J. Kibler, R. Cess and the ERBE Science Team, 1989: Earth Radiation Budget Experiment (ERBE) archival and April 1985 results. *Bull. Amer. Meteor. Soc.*, **70**, 1254-1262.

Bohren, C.F., and D.R. Huffman, 1983: *Absorption and Scattering of Light by Small Particles*. John Wiley & Sons, Inc., New York, 530 pp.

Bréon, F.-M., 1992: Reflectance of broken cloud fields: simulation and parameterization. *J. Atmos. Sci.*, **49**, 1221-1232.

Busygin, V.P., N.A. Yevstratov, and Ye. M. Feigel'son, 1973: Optical properties of cumulus clouds, and radiant fluxes for cumulus cloud cover. *Izv. Atmos. Oceanic Phys.*, **9**, 1142-1151.

Cahalan, R.F., 1989: Overview of fractal clouds. *Advances in Remote Sensing*, Deepak, 317-389.

Cannon, J.C., 1970: Line transfer in two dimensions, *Astrophys. J.*, **161**, 255-264.

Cess, R.D. et al., 1990: Intercomparison and interpretation of climate feedback processes in 19 atmospheric general circulation models, *J. Geophys. Res.*, **95**, 16601-16615.

Chandrasekhar, S., 1950: *Radiative Transfer*, 393 pp., Oxford University Press, New York.

Coakley, J. A., 1991: Reflectivities of uniform and broken layered clouds. *Tellus*, **43B**, 420-433.

Coakley, J.A., Jr., and R. Davies, 1986: The effect of cloud sides on reflected solar radiation as deduced from satellite observations. *J. Atmos. Sci.*, **43**, 1025-1035.

Davies, R., 1978: The effect of finite geometry on the three-dimensional transfer of solar irradiance in clouds. *J. Atmos. Sci.*, **35**, 1712-1725.

Davies, R., 1984: Reflected solar radiances from broken cloud scenes and the interpretation of scanner measurements. *J. Geophys. Res.*, **89**, 1259-1266.

Davies, R., 1994: Spatial autocorrelation of radiation measured by the Earth Radiation Budget Experiment: Scene inhomogeneity and reciprocity violation. *J. Geophys. Res.*, **99**, 20879-20887.

Davies, R., W.L. Ridgway, and K.-E. Kim, 1984: Spectral absorption of solar radiation in cloudy atmospheres: A 20 cm^{-1} model, *J. Atmos. Sci.*, **41**, 2126-2137.

Davis, A., P.G. Gabriel, S. Lovejoy, D. Schertzer, and G.L. Austin, 1990: Discrete angle radiative transfer. Part III: Numerical results and applications. *J. Geophys. Res.*, **95**, 11729-11742.

Deirmendjian, D., 1969: *Electromagnetic Scattering on Spherical Polydispersions.* Elsevier, 290 pp.

Dozier, J., 1994: Planned EOS observations of the land, ocean and atmosphere. *Atmos. Res.*, **31**, 329-357.

Durkee, P.A., F. Pfeil, E. Frost, and R. Shema, 1991: Global analysis of aerosol particle characteristics. *Atmos. Environ.*, **25A**, 2457-2471.

Hale, G.M., and M.R. Querry, 1973: Optical constants of water in the 200-nm to 200 μm wavelength region. *Appl. Opt.*, **12**, 555-563.

Harshvardhan and R.W.L. Thomas, 1984: Solar reflection from interacting and shadowing cloud elements, *J. Geophys. Res.*, **89**, 7179-7185.

Hartmann, D. L., and E. E. Recker, 1986: Diurnal variation of outgoing longwave radiation in the tropics. *J. Climate and Appl. Meteor.*, **25**, 800-812.

Hartmann, D. L., V. Ramanathan, A. Berroir, and G.E. Hunt, 1986: Earth radiation budget data and climate research, *J. Geophys. Res.*, **24**, 439-468.

Hoppel, W.A., J.W. Fitzgerald, G.M. Frick, R.E. Larson, and E.J. Mack, 1990: Aerosol size distributions and optical properties found in the marine boundary layer over the Atlantic Ocean. *J. Geophys. Res.*, **95**, 3659-3686.

Kneizys, F. X., E. P. Shettle, L. W. Abreu, J. H. Chetwynd, Jr., G. P. Anderson, W. O. Gallery, J. E. A. Selby and S. A. Clough, 1988: Users Guide to LOWTRAN 7. Air Force Geophysics Lab., Hanscom AFB, MA, Rept. AFGL-TR-88-0177, 137 pp.

Kobayashi, T., 1988: Parameterization of reflectivity for broken cloud fields. *J. Atmos. Sci.*, 45, 3034-3045.

Kobayashi, T., 1993: Effects due to cloud geometry on biases in the albedo derived from radiance measurements. *J. Climate*, **6**, 120-128.

Kopia, L.P., 1986: The Earth Radiation Budget Experiment Scanner instrument. *Rev. Geophys.*, **24**, 400-406.

Koepke, P., and H. Quenzel, 1979: Turbidity of the atmosphere determined from satellite: Calculation of optimum viewing geometry. *J. Geophys. Res.*, **84**, 7847-7856.

Loeb, N.G., 1992: *A Multispectral Retrieval Technique for Inferring Cloud and Clear Sky Properties Over Ocean From Satellite Measurements*. M.Sc. Thesis, 186 pp., York University, Toronto, Canada.

Machado, L. A. T., M. Desbois, and J.-P. Duval, 1992: Structural characteristics of deep convective systems over tropical Africa and Atlantic Ocean. *Mon. Weather Rev.*, **120**, 392-406.

McKee, T. B., and S. K. Cox, 1974: Scattering of visible radiation by finite clouds. *J. Atmos. Sci.*, **31**, 1885-1892.

Minnis, P., 1989: Viewing zenith angle dependence of cloudiness determined from coincident GOES East and GOES West data. *J. Geophys. Res.*, **94**, 2303-2320.

Minnis, P., and E. F. Harrison, 1984: Diurnal variability of regional cloud and clear-sky radiative parameters derived from GOES data. Part II: November 1978 cloud distributions. *J. Clim. and Appl. Meteor.*, **23**, 1012-1031.

Prospero, J.M., R.J. Charlson, V. Mohnen, R. Jaenicke, A.C. Delany, J. Moyers, W. Zoller, and K. Rahn, 1983: The atmospheric aerosol system: an overview. *Rev. Geophys. Space Phys.*, **21**, 1607-1629.

Ramanathan, V., 1987: The role of Earth radiation budget studies in climate and general circulation research, *J. Geophys. Res.*, **92**, 4075-4095.

Rossow, W.B., 1989: Measuring cloud properties from space: A review, *J. Climate*, **2**, 201-213.

Rossow, W.B., and R.A. Schiffer, 1991: ISCCP cloud products. *Bull. Amer. Meteor. Soc.*, **72**, 2-20.

Schiffer, R.A., and W.B. Rossow, 1983: The International Satellite Cloud Climatology Project (ISCCP): The first project of the World Climate Research Program. *Bull. Amer. Meteor. Soc.*, **64**, 779-784.

Stamnes, K., S.-C. Tsay, W. Wiscombe, and K. Jayaweera, 1988: Numerically stable algorithm for discrete-ordinate-method radiative transfer in multiple scattering and emitting layered media, *Appl. Opt.*, **24**, 2502-2509.

Stephens, G.L., 1986: Radiative transfer in spatially heterogeneous, two dimensional, anisotropically scattering media, *J. Quant. Spectrosc. Radiat. Transfer,* **36**, 51-67.

Stephens, G.L., 1988: Radiative transfer through arbitrarily shaped optical media. Part I: General method of solution, *J. Atmos. Sci.*, **45**, 1818-1848.

Stephens, G.L., and S.-C. Tsay, 1990: On the cloud absorption anomaly, *Quart. J. Roy. Meteor. Soc.*, **116**, 671-704.

Stowe L.L., H.Y.M. Yeh, T.F. Eck, C.G. Wellemeyer, H.L. Kyle, and Nimbus-7 Cloud Data Processing Team, 1989: Nimbus-7 Global Cloud Climatology. Part II: First Year Results, *J. Climate*, 2, 671-709.

Stuhlmann, R., P. Minnis, and G. L. Smith, 1985: Cloud bidirectional reflectance functions: a comparison of experimental and theoretical results. *Appl. Opt.*, **24**, 396-401.

Toon, O.B., and J.B. Pollack, 1976: A global average model of atmospheric aerosols for radiative transfer calculations. *J. Appl. Meteor.*, **15**, 225-246.

Warren, S.G., C.J. Hahn, J. London, R.M. Chervin, and R.L. Jenne, 1988: Global distribution of total cloud cover and cloud type amounts over the ocean. NCAR Technical Note TN-317+STR, Boulder, CO, 42 pp. + 170 maps.

WCRP, 1990: The radiative effects of clouds and their impact on climate. A. Arking, ed., WMO/TD-NO. 399, World Meteorological Organization, Geneva, 39 pp.

Weinman, J.A., and Harshvardhan, 1982: Solar reflection from a regular array of horizontally finite clouds, *Appl. Opt.*, **21**, 2940-2944.

Welch, R.M., S.K. Cox and J.M. Davis, 1980: *Solar radiation and clouds*, Meteorological Monographs, **17**, 39, American Meteorological Society.

Welch, R.M., and B.A. Wielicki, 1984: Stratocumulus cloud field reflected fluxes: The effect of cloud shape, *J. Atmos. Sci.*, **41**, 3085-3103.

Wendling, P., 1977: Albedo and reflected radiance of horizontally inhomogeneous clouds, *J. Atmos. Sci.*, **34**, 642-650.

Wielicki, B.A., and R.N. Green, 1989: Cloud identification for ERBE radiative flux retrieval. *J. Appl. Meteor.*, **28**, 1133-1146.

Wielicki, B.A., and L. Parker, 1992: On the determination of cloud cover from satellite sensors: The effect of sensor spatial resolution. *J. Geophys. Res.*, **97**, 12799-12823.

Ye, Q., and J.A. Coakley, Jr., 1994a: Biases in earth radiation budget observations, Part I: Effects of scanner spatial resolution on the observed anisotropy, submitted to *J. Geophys. Res.*

Ye, Q., and J.A. Coakley, Jr., 1994b: Biases in earth radiation budget observations, Part II: Consistent scene identification and anisotropic factors, submitted to *J. Geophys. Res.*

Young, M.J., 1967: Variability in estimating total cloud cover from satellite pictures, *J. Appl. Meteor.*, **6**, 573-579.